The Dissertation Committee for Yingnan Liu Certifies that this is the approved version of the following Dissertation:

Second-order Nonlinear Intersubband Polaritonic Metasurfaces

Committee:

Mikhail A. Belkin, Supervisor

Seth R. Bank

Ray Chen

Alexey Belyanin

Igal Brener

Second-order Nonlinear Intersubband Polaritonic Metasurfaces

by

Yingnan Liu

Dissertation

Presented to the Faculty of the Graduate School of

The University of Texas at Austin

in Partial Fulfillment

of the Requirements

for the Degree of

Doctor of Philosophy

The University of Texas at Austin

December 2019

Dedication

To My Family

Acknowledgements

First of all, I would like to thank my mother Juan Wang for her love, endless support, and sacrifices in my whole life. I also want to thank my father, Junjie Liu and little brother Yunyu Liu, for their understanding, support, and encouragement. Thank you for always being there for me.

Secondly, I appreciate the guidance of my supervisor, Prof. Mikhail Belkin. In the past four years, he has provided some critical and brilliant advice to help me develop different theoretical models. I also want to thank Dr. Ray Chen, Dr. Seth R. Bank, Dr. Alexey Belyanin, Dr. Igal Brener, for kindly serving on my dissertation committee.

Thirdly, I would like to express my gratitude to our group members and my collaborators for their help: Dr. Jongwon Lee, Dr. Aiting Jiang, Dr. Feng Lu, Dr. Seungyong Jung, Dr. Yifan Jiang, Dr. Daniele Palaferri, Jeahyun Kim, Nishant Nookala, Jiaming Xu, Jialin Mei, Stephen March, John F. Klem, Mykhailo Tymchenko.

Finally, I would like to thank my friends Shinuo Weng, Zhe Wang and Dian who have been incredibly supportive through the difficult time. Their support has made me a stronger person, and I will always be grateful.

Abstract

Second-order Nonlinear Intersubband Polaritonic Metasurfaces

Yingnan Liu, Ph.D.

The University of Texas at Austin, 2019

Supervisor: Mikhail Belkin

Frequency mixing is an essential nonlinear process with extensive applications in photonics, chemistry, biology, and energy sciences. Traditional nonlinear crystals have weak nonlinear responses and light beams need long propagation distances in the crystals to accumulate a significant wave mixing in practice. However, wave mixing in such bulky crystals results in stringent phase-matching requirements and bulk nonlinear crystals are not compatible with modern "flat" optics concept that enables complete control of the phase-front of the output beam but requires optical medium with sub-wavelength thickness. Fortunately, the emerging of metasurfaces has provided an efficient method to generate the large nonlinear response on nanoscale. The metasurfaces have enabled the development of "flat" optical elements with the intrinsic benefit of small thickness, intricate control of the optical wavefront, and, in case of nonlinear optical elements, relaxed phase-matching constraints.

In my Ph.D. dissertation, I focus on the second-order intersubband polaritonic nonlinear metasurfaces. These structures combine enormous intersubband nonlinear response in III-V semiconductor heterostructures and field enhancement of plasmonic nano-resonators. Our earlier research has demonstrated giant nonlinear responses for the

second harmonic generation in metasurfaces. In this dissertation, I propose several approaches to improve the performance of second harmonic generation metasurfaces and extend their functionality to difference-frequency and sum-frequency generation in the mid-infrared range. For the first part of this study, I have demonstrated new multi-quantum-well designs for second harmonic generation with materials have much narrower linewidth compared with previous materials. This leads to a conversion efficiency of 1.2%. Second, I have demonstrated the mid-infrared difference-frequency generation in polaritonic nonlinear metasurface for the first time. The optimization of the metasurface, the theoretical investigation of the saturation effect, the fabrication of the metasurface, and the experimental characterization of the metasurface have been discussed. The effective nonlinear susceptibility is 340 nm/V and the difference-frequency generation conversion efficiency of this metasurface is 0.13%. I have also demonstrated the mid-infrared sum-frequency generation in a polaritonic nonlinear metasurface. Both the theoretical analysis of the saturation effect and the experimental characterization of the metasurface have been illustrated. The upconversion efficiency of this metasurface is 0.03% and the nonlinear susceptibility is 158 nm/V. In addition, as the prospect of the SFG metasurfaces, the performance of metasurfaces under extremely high pump intensity has been discussed and the metasurface designs for high-conversion-efficiency have been proposed. For the last part of this study, metasurfaces in the THz range have been explored. These metasurfaces are designed to generate 4~6 THz with a difference-frequency generation process from polaritonic metasurfaces at room temperature. The theoretical analysis, sample design, and preliminary experimental results have been discussed.

Table of Contents

List of Tables

List of Figures

Chapter 1: Introduction

1.1 Overview

Flat optical components [*1*] have recently received growing attention in the photonics and nano-electronics communities due to their promise to dramatically simplify the production of traditional linear optical components, such as lenses, and their ability to control the wavefront of light beyond that possible with traditional optical components. This technology relies on metasurfaces made of arrays of sub-wavelength nano-inclusions, which allow people to manipulate local amplitude and phase of reflected or transmitted optical beams and control nonlinear optical effects [*2-4*]. These miniaturized structures support very tight confinement of fields [*5*] and have been employed to demonstrate phase control [*6-8*] and frequency mixing [*9, 10*] of light waves. Ultra-thin nonlinear metasurfaces, in particular, present an additional benefit relaxed phase-matching constraints for wave mixing processes. Indeed, by shining a light beam onto the 2D array of nano-resonators, the phase matching condition is easily achieved by matching k-vector components parallel to the metasurface, thanks to the subwavelength thickness of its constituents. However, for frequency mixing, the limited nonlinear response in the infrared/visible range in traditional nonlinear materials [*11, 12*] and nonlinear metasurfaces based on plasmonic nano-resonators [*13, 14*] requires further improvement for practical applications.

In our earlier research [*9, 10*], we have combined the giant nonlinear response associated with intersubband transitions in multi-quantum-well (MQW) semiconductor heterostructures and the high field enhancement of plasmonic nano-resonators to create ultra-thin metasurfaces with giant out-of-plane second harmonic response, which is 3-5 orders of magnitude higher than previous reports in the literature. These initial studies

used pulsed lasers and focused only on the nonlinear process of second harmonic generation. In addition to second harmonic generation (SHG), other second-order nonlinear response such as difference-frequency and sum-frequency generation (DFG and SFG) can also bring exciting applications. For example, two infrared high power lasers can be used to build a high-power THz source through a DFG process [*15*]. Analogously, metasurfaces with a suitable continuous-wave (CW) pump laser can be used to upconvert low-intensity long wavelength infrared (LWIR, λ=8-12μm) and THz signals to the mid-wavelength infrared (MWIR, λ=3-5μm) or the short-wavelength infrared (SWIR, λ=1-3μm) bands, where photodetector focal plane arrays are less expensive and more robust.

1.2 OUTLINE

This dissertation introduces the design and development of second-order nonlinear plasmonic metasurfaces, including SHG, DFG, and SFG metasurfaces. Fundamental theoretical background about intersubband transition in MQWs and the coupling between intersubband transition and metallic nanoresonators are illustrated in Chapter 2. Chapter 3 focuses on the development of SHG metasurfaces. The general MQW design rules and new designs for SHG have been discussed in this chapter. In Chapter 4, both the theoretical investigation and experimental characterization of DFG metasurfaces have been demonstrated. In this chapter, the optimization of nanoresonators, the fabrication of metasurfaces, the experimental measurement, and corresponding theoretical analysis are shown in detail. As mentioned earlier, the nonlinear processes could be used to generate new laser sources. To achieve high frequency conversion efficiency in nonlinear wave mixing, one usually requires at least one strong pump laser. In my DFG metasurface research, a CW CO_2 laser was used to

explore the performance of metasurfaces under strong pump power illumination. SFG, the reverse process of DFG, has been studied in Chapter 5 with theoretical analysis and experimental characterization. In Chapter 6, as the prospect of the SFG metasurfaces, the performance of metasurfaces under extremely high pump intensity is discussed. In Chapter 7, THz DFG metasurfaces have been explored. These metasurfaces are designed to generate 4~6 THz with DFG process from highly nonlinear ultra-thin metasurfaces at room temperature. The theoretical analysis, sample design, and preliminary experimental results are discussed here. A summary of present work is given in Chapter 8.

Chapter 2: Theoretical Background

2.1 Intersubband Transitions in N-doped III-V Semiconductor Heterostructure

2.1.1 Dielectric Function

Intersubband (ISB) transitions are the optical excitations between the quantized electronic energy levels within the conduction band (or within the valence band) of semiconductor heterostructures [*16*]. In ultra-thin layers of n-doped semiconductors, such as n-doped III-V multi-quantum-well, the electrons are confined in the growth direction due to band offset of different materials. The confinement of electrons forms quantized energy levels in conduction bands. Optical transitions can happen between these subbands and, thus, various nonlinear processes can be observed in such systems. Due to the selection rules, only the electric field normal to the quantum well growth plane will effectively excite the intersubband transitions. Intersubband transitions have some physical properties that are important in practice, including tunable absorption (or emission) wavelengths, sharp absorption or emission linewidth, and ultrafast carrier dynamics.

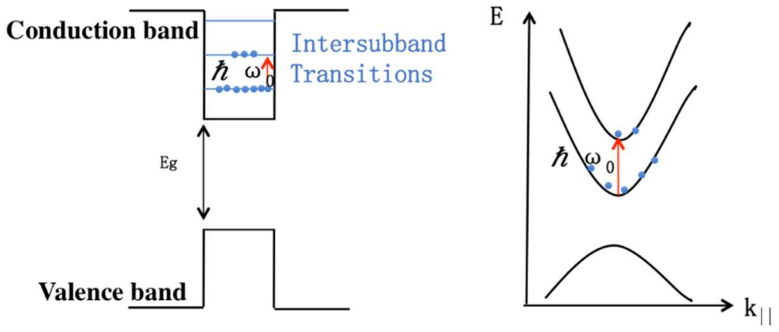

Figure 2.1: Mechanism of intersubband transitions.

The electrons in MQWs can move without restrictions within the quantum-well layers, while get confined in the growth direction. Thus the dielectric functions are anisotropic. The dielectric constant perpendicular to the semiconductor layers can be estimated as [*10, 16*]:

$$\varepsilon_{\perp}(\omega) \approx \varepsilon_{core}(\omega) + \frac{Ne^2 z_{ij}^2}{\epsilon_0 \hbar(\omega_{ij} - \omega - i\gamma_{ij})} \tag{2.1}$$

where ez_{ij} is the transition dipole moment between state i and j, ω_{ij} and γ_{ij} is the transition frequency and linewidth between state i and j respectively, *N* is the average electron volume concentration, and ε_{core} is the dielectric constant with no doping. Here we assume electrons are in the ground state. Since the electrons are free to move in the directions parallel to the layers, the in-plane dielectric constant of the MQW can be described with the Drude-Lorentz model [*10*]:

$$\varepsilon_{\parallel}(\omega) \approx \varepsilon_{core}(\omega) + \frac{iNe^2\tau_D}{\omega m^*(1 - i\omega\tau_D)} \tag{2.2}$$

where $\tau_D \approx 10^{-13}$ s is the Drude relaxation time, m^* is the effective mass, ω is the frequency of the incident beam.

2.1.2 Nonlinear Susceptibility

The polarization *P* of a material system depends on the strength of applied optical field *E*.

$$\tilde{P} = \varepsilon_0\left[\chi^{(1)}\tilde{E} + \chi^{(2)}\tilde{E}^2 + \chi^{(3)}\tilde{E}^3 + \cdots\right] = \tilde{P}^{(1)} + \tilde{P}^{(2)} + \tilde{P}^{(3)} + \cdots \tag{2.3}$$

where $\chi^{(1)}$ is the linear susceptibility, $\chi^{(2)}$ is the second-order susceptibility, $\chi^{(3)}$ is the third-order susceptibility. $\chi^{(2)}$ is a third-rank tensor, and each element of second-order polarization is $P_i^{(2)} = \varepsilon_0 \chi_{ijk}^{(2)} E_j E_k$. From quantum mechanics, the second-order susceptibility can be described as [*11*]:

$$\chi_{ijk}^{(2)}(\omega_p+\omega_q,\omega_q,\omega_p) \tag{2.4}$$
$$=\frac{e^3}{2\epsilon_0\hbar^2}\sum_{lmn}N_l\left\{\frac{z_{ln}^i z_{nm}^j z_{ml}^k}{(\omega_{nl}-\omega_p-\omega_q-i\gamma_{nl})(\omega_{ml}-\omega_p-i\gamma_{ml})}\right.$$
$$+\frac{z_{ln}^i z_{nm}^k z_{ml}^j}{(\omega_{nl}-\omega_p-\omega_q-i\gamma_{nl})(\omega_{ml}-\omega_q-i\gamma_{ml})}$$
$$+\frac{z_{ln}^k z_{nm}^i z_{ml}^j}{(\omega_{mn}-\omega_p-\omega_q-i\gamma_{mn})(\omega_{nl}+\omega_p+i\gamma_{nl})}$$
$$+\frac{z_{ln}^j z_{nm}^i z_{ml}^k}{(\omega_{mn}-\omega_p-\omega_q-i\gamma_{mn})(\omega_{nl}+\omega_q+i\gamma_{nl})}$$
$$+\frac{z_{ln}^j z_{nm}^i z_{ml}^k}{(\omega_{nm}+\omega_p+\omega_q+i\gamma_{nm})(\omega_{ml}-\omega_p-i\gamma_{ml})}$$
$$+\frac{z_{ln}^k z_{nm}^i z_{ml}^j}{(\omega_{nm}+\omega_p+\omega_q+i\gamma_{nm})(\omega_{ml}-\omega_q-i\gamma_{ml})}$$
$$+\frac{z_{ln}^k z_{nm}^j z_{ml}^i}{(\omega_{ml}+\omega_p+\omega_q+i\gamma_{ml})(\omega_{nl}+\omega_p+i\gamma_{nl})}$$
$$\left.+\frac{z_{ln}^j z_{nm}^k z_{ml}^i}{(\omega_{ml}+\omega_p+\omega_q+i\gamma_{ml})(\omega_{nl}+\omega_q+i\gamma_{nl})}\right\}$$

where ez_{ij} is the electric dipole moment between state i and j, γ_{ij} and ω_{ij} is the transition linewidth and frequency between state i and j respectively, ω_q and ω_p are two input frequencies, N_i is the population of the state i. The MQW energy levels and dipole moments can be tuned by changing the materials compositions, doping levels, and width of quantum wells and barriers. With proper tailoring, giant intersubband optical nonlinearities can be produced in this engineered semiconductor MQW structures. It is known that *n*-doped coupled MQWs may be designed to have second-order nonlinear susceptibilities up to 3-5 orders of magnitude larger than traditional bulk nonlinear materials [*17*].

2.1.3 Saturation of Intersubband Transitions

From the expression of second-order susceptibility, we know that the second-order susceptibility has a relationship with electron populations of different energy levels. With strong pump intensities, electrons are pump to higher energy level and may cause saturation effects [*18, 19*].

For example, for SHG in a three-level system, one can write:

$$\chi^{(2)}_{MQW,zzz}(2\omega,\omega,\omega) = \frac{e^3}{\varepsilon_0\hbar^2}\left\{\frac{(N_1 - 2N_2 + N_3)z_{12}z_{23}z_{31}}{(\omega_{31} - 2\omega - i\gamma_{31})(\omega_{21} - \omega - i\gamma_{21})}\right\} \tag{2.5}$$

The populations of different subbands can be calculated as shown below. The first 3 energy levels in the conduction band are considered. I_z^{ω} is the pump intensity of fundamental frequency. N_i is the population of state i, N is the total electron concentration. $\alpha_{ij}(\omega)$ is the absorption coefficient between state i and j at frequency ω, $\alpha_{ij}(\omega) = \frac{(N_i - N_j)\alpha_{ij}^{(0)}}{N}$, where $\alpha_{ij}^{(0)}$ [*18*] is the absorption coefficient with all carriers on state i. τ_{ij} is the relaxation time between state i and j. Here the pump intensity at frequency 2ω is neglected. The rate equations are given as:

$$\begin{cases} \dfrac{dN_1}{dt} = \dfrac{-\alpha_{12}(\omega)I_z^{\omega}}{\hbar\omega} + \dfrac{N_2}{\tau_{12}} + \dfrac{N_3}{\tau_{13}} \\ \dfrac{dN_2}{dt} = \dfrac{\alpha_{12}(\omega)I_z^{\omega}}{\hbar\omega} - \dfrac{\alpha_{23}(\omega)I_z^{\omega}}{\hbar\omega} - \dfrac{N_2}{\tau_{12}} + \dfrac{N_3}{\tau_{23}} \\ \dfrac{dN_3}{dt} = \dfrac{\alpha_{23}(\omega)I_z^{\omega}}{\hbar\omega} - \dfrac{N_3}{\tau_{13}} - \dfrac{N_3}{\tau_{23}} \end{cases} \tag{2.6}$$

For steady state，

$$\begin{cases} \dfrac{-\alpha_{12}(\omega)I_z^{\omega}}{\hbar\omega}+\dfrac{N_2}{\tau_{12}}+\dfrac{N_3}{\tau_{13}}=0 \\ \dfrac{\alpha_{12}(\omega)I_z^{\omega_1}}{\hbar\omega}-\dfrac{\alpha_{23}(\omega)I_z^{\omega}}{\hbar\omega}-\dfrac{N_2}{\tau_{12}}+\dfrac{N_3}{\tau_{23}}=0 \\ \dfrac{\alpha_{23}(\omega)I_z^{\omega}}{\hbar\omega}-\dfrac{N_3}{\tau_{13}}-\dfrac{N_3}{\tau_{23}}=0 \end{cases} \tag{2.7}$$

$$\begin{cases} -\dfrac{(N_1-N_2)\alpha_{12}^{(0)}I_z^{\omega}}{N\hbar\omega}+\dfrac{N_2}{\tau_{12}}+\dfrac{N_3}{\tau_{13}}=0 \\ \dfrac{(N_1-N_2)\alpha_{12}^{(0)}I_z^{\omega}}{N\hbar\omega}-\dfrac{(N_2-N_3)\alpha_{23}^{(0)}I_z^{\omega}}{N\hbar\omega}-\dfrac{N_2}{\tau_{12}}+\dfrac{N_3}{\tau_{23}}=0 \\ \dfrac{(N_2-N_3)\alpha_{23}^{(0)}I_z^{\omega}}{N\hbar\omega}-\dfrac{N_3}{\tau_{13}}-\dfrac{N_3}{\tau_{23}}=0 \end{cases} \tag{2.8}$$

Set

$$\begin{cases} I_{12}^{sat}=\dfrac{N\hbar\omega}{2\tau_{12}\alpha_{12}^{(0)}} \\ I_{23}^{sat}=\dfrac{N\hbar\omega}{2\tau_{23}\alpha_{23}^{(0)}} \end{cases} \tag{2.9}$$

Then the relationships between populations of different levels are

$$\begin{cases} N_1=N_3\left\{\left(1+\dfrac{2I_{12}^{sat}}{I_z^{\omega}}\right)\left(1+\dfrac{2I_{23}^{sat}\tau_{13}}{I_z^{\omega}\tau_{13}}+\dfrac{2I_{23}^{sat}}{I_z^{\omega}}\right)+\dfrac{2I_{12}^{sat}\tau_{12}}{I_z^{\omega}\tau_{13}}\right\} \\ N_2=N_3\left(1+\dfrac{2I_{23}^{sat}\tau_{23}}{I_z^{\omega}\tau_{13}}+\dfrac{2I_{23}^{sat}}{I_z^{\omega}}\right) \\ N_1+N_2+N_3=N \end{cases} \tag{2.10}$$

The saturation factor

$$\frac{(N_1 - 2N_2 + N_3)}{N} = \frac{4I_{12}^{sat}I_{23}^{sat}\left(1+\frac{\tau_{23}}{\tau_{13}}\right) + 2I_{12}^{sat}I_z^{\omega}\left(1+\frac{\tau_{12}}{\tau_{13}}\right) - 2I_{23}^{sat}I_z^{\omega}\left(1+\frac{\tau_{23}}{\tau_{13}}\right)}{3I_z^{\omega}I_z^{\omega} + 4I_z^{\omega}I_{23}^{sat}\left(1+\frac{\tau_{23}}{\tau_{13}}\right) + 2I_{12}^{sat}I_z^{\omega}\left(1+\frac{\tau_{12}}{\tau_{13}}\right) + 4I_{12}^{sat}I_{23}^{sat}\left(1+\frac{\tau_{23}}{\tau_{13}}\right)} \tag{2.11}$$

With this equation, local electron populations under different pump intensities can be achieved, so as the second-order susceptibility. This will cause saturation in the output SHG power [*9*]. Similarly, the saturation effects will also affect DFG and SFG output power and will be explained in detail in Chapter 4 and 5.

2.2 The Coupling of ISB Transitions and Metallic Nanoresonators

The light-matter coupling in MQW systems occurs only by employing TM-polarized electromagnetic waves, due to the ISB polarization selection rule. Therefore normal incidence light does not couple with electron states in QWs. An approach to achieve normal incident light coupling with MQWs is taking advantage of metallic nanoresonators.

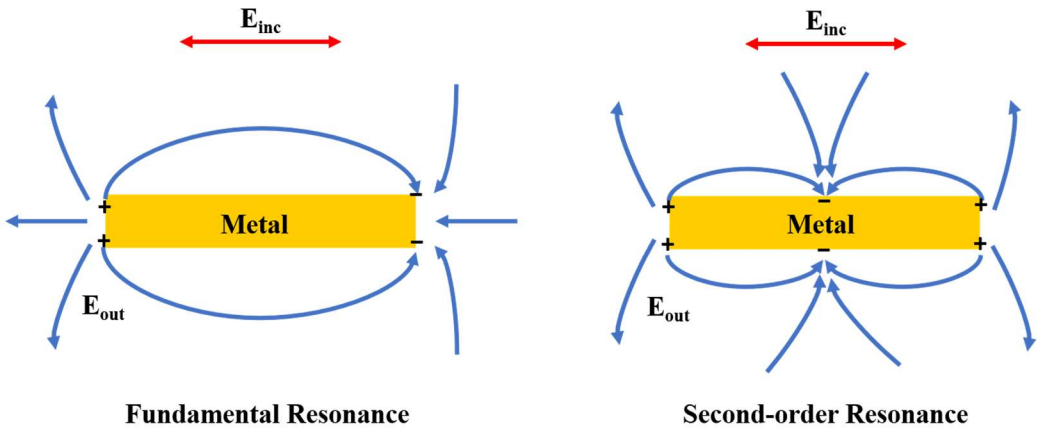

Figure 2.2: Schematic of the E-field polarization directions of the output beams (blue) at the fundamental and second-order resonance with normal incident beams (red).

For example, in Fig. 2.2, incident light with an E-field polarized in a horizontal direction can cause fundamental plasmon resonance and higher-order plasmon resonance in a metal rod structure at certain frequencies. Plasmons (electric charge oscillations) in nanorods can generate E field with a component in the vertical direction (TM-polarized electric field), which can couple with ISB electrons. When the frequencies of confined modes of the plasmonic nanoresonators are in resonance with specific ISB transitions, large nonlinearities can be generated in MQWs.

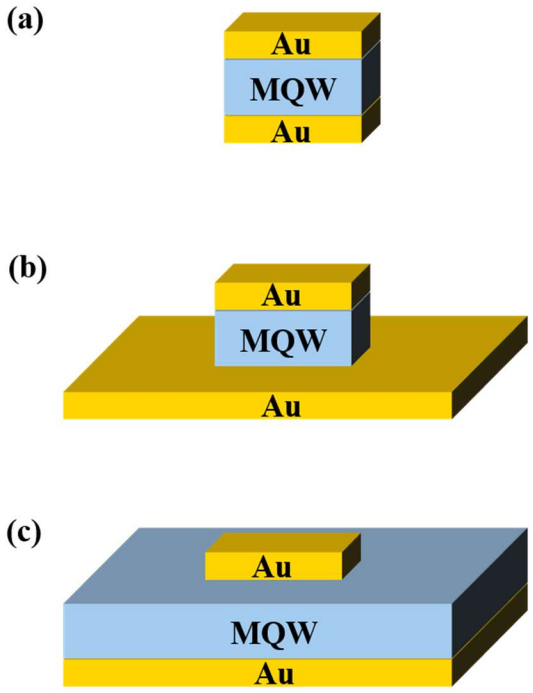

Figure 2.3: Three types of metal-insulator-metal (MIM) configurations.

Except using metallic nanoresonators only on top of the insulators, structures with metallic nanoresonators on both top and bottom are also broadly used. By placing two metal-dielectric interfaces close to each other, there is near-field coupling between the plasmon modes of the two metals [*20*]. There are typically three types of MIM

configurations [*20*], as shown in Fig. 2.3. The fabrication of Type (a) structure involves plasma etching of the bottom Au layer after wafer bonding, which is much harder than the plasma etching of the top Au layer. Considering the complicated fabrication process of Type (a) structure, it is not commonly used in MQW based polaritonic metasurfaces. The other two types are both widely used, and generally, Type (b) provides a better field enhancement compared with Type (c) based on our experience [*9, 10*].

In the past few years, many reports have shown the combination of plasmonic antennas with ISB transitions in different applications, such as performances enhancement for mid-infrared and terahertz detectors [*21, 22*] and Purcell enhancement of THz emission from quantum cascade electroluminescent devices [*23*].

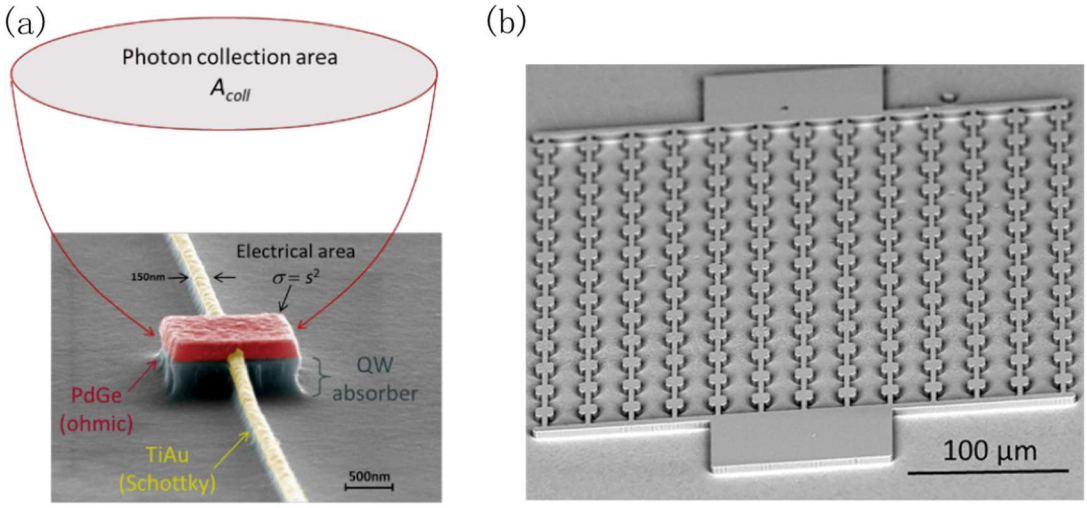

Figure 2.4: (a) Device structure of the room temperature antenna-coupled quantum well infrared photodetector at 8.9 µm [*21*]. (b) SEM image of patch antenna microcavity terahertz sources [*23*].

In our earlier research on polaritonic ISB nonlinear metasurfaces, we have demonstrated giant SHG based on the coupling of ISB transition and plasmonic

resonators [*9, 10*]. The design purpose of such patterned metasurfaces is to maximize the enhancement of the normal component of the polarization in the quantum material at the input frequency and at the same time enhancing the out-coupling of radiation to free-space at the generated frequency. The optimization of metasurfaces is illustrated in Chapter 4.

2.3 LORENTZ RECIPROCITY THEOREM AND THE OVERLAP INTEGRAL

A current density $\widetilde{J_1}$ produces an electric field $\widetilde{E_1}$ and a magnetic field $\widetilde{H_1}$. A second current density $\widetilde{J_2}$ produces an electric field $\widetilde{E_2}$ and a magnetic field $\widetilde{H_2}$. They all have same frequency ω and same time dependence $e^{-i\omega t}$. For arbitrary volume V containing these two sets of sources $\widetilde{J_1}$ and $\widetilde{J_2}$,

$$\int_V (\widetilde{J_1}\cdot\widetilde{E_2} - \widetilde{E_1}\cdot\widetilde{J_2})dV = \oint_S (\widetilde{E_1}\times\widetilde{H_2} - \widetilde{E_2}\times\widetilde{H_1})\cdot d\tilde{S} \tag{2.12}$$

Where S is the surface enclosing the volume V. If $\widetilde{J_1}$ and $\widetilde{J_2}$ are localized sources, and there are no incoming waves from infinitely far away, we have

$$\int_V \widetilde{J_1}\cdot\widetilde{E_2}dV = \int_V \widetilde{E_1}\cdot\widetilde{J_2}\,dV \tag{2.13}$$

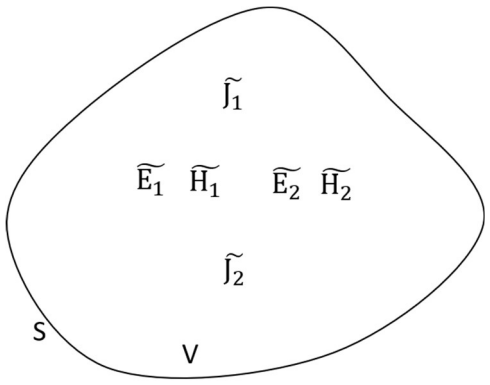

Figure 2.5: Geometry for the Lorentz reciprocity theorem.

For example, in the DFG metasurface, two input beams generate a current source $J_{MQW}^{\omega_{DFG}}$ in the MQW through a nonlinear process. This current source generates an electric field $E_{out}^{\omega_{DFG}}$ in the air and $E_{out}^{\omega_{DFG}}$ is the desired DFG output signal. Here since it is not convenient to simulate the $E_{out}^{\omega_{DFG}}$ directly, the Lorentz reciprocity theorem is used in the calculation of $E_{out}^{\omega_{DFG}}$ as below.

A 2D surface source in the air $J_{2D}^{\omega_{DFG}}$ generates an electric field in the MQW with z-component of $E_z^{\omega_{DFG}}$. A current source $J_{MQW}^{\omega_{DFG}}$ in the MQW generates an electric field $E_{out}^{\omega_{DFG}}$ in the air. With Lorentz reciprocity theorem, we can get:

$$\int_S J_{2D}^{\omega_{DFG}} \cdot E_{out}^{\omega_{DFG}} dS = \int_V E_z^{\omega_{DFG}} \cdot J_{MQW}^{\omega_{DFG}} \, dV \tag{2.14}$$

where V is the unit cell of designed nanoresonator. The $J_{2D}^{\omega_{DFG}}$ and $E_z^{\omega_{DFG}}$ can be easily got from the simulation. Since only z-components can contribute to the nonlinear process in the MQW, the $J_{MQW}^{\omega_{DFG}}$ can be calculated with:

$$J_{MQW}^{\omega_{DFG}} = j2\omega\varepsilon_0\chi_{MQW,zzz}^{(2)} E_z^{\omega_1} E_z^{\omega_2} \tag{2.15}$$

where $E_z^{\omega_1}$ and $E_z^{\omega_2}$ are the z-components of the electric fields in the MQW generated by the two input beams $E_{inc}^{\omega_1}$ and $E_{inc}^{\omega_2}$. The optimized nanoresonators can contribute to the field enhancements, and these field enhancements are described by $\frac{E_z^{\omega_1}}{E_{inc}^{\omega_1}}$, $\frac{E_z^{\omega_2}}{E_{inc}^{\omega_2}}$, and $\frac{E_z^{\omega_{DFG}}}{E_{inc}^{\omega_{DFG}}}$, thus

$$J_{MQW}^{\omega_{DFG}} = j2\omega\varepsilon_0\chi_{MQW,zzz}^{(2)} \frac{E_z^{\omega_1}}{E_{inc}^{\omega_1}} \frac{E_z^{\omega_2}}{E_{inc}^{\omega_2}} E_{inc}^{\omega_1} E_{inc}^{\omega_2} \tag{2.16}$$

From equation (4.6), (4.8), and $J_{2D}^{\omega_{DFG}} = 2\varepsilon_0 c E_{inc}^{\omega_{DFG}}$, we can get

$$E_{out}^{\omega_{DFG}} = \frac{j2\omega \int_V \chi_{MQW,zzz}^{(2)} \frac{E_z^{\omega_1}}{E_{inc}^{\omega_1}} \frac{E_z^{\omega_2}}{E_{inc}^{\omega_2}} E_{inc}^{\omega_1} E_{inc}^{\omega_2} \frac{E_z^{\omega_{DFG}}}{E_{inc}^{\omega_{DFG}}} dV}{cS} \tag{2.17}$$

If we set

$$P_{eff}^{\omega_{DFG}} = \varepsilon_0 \chi_{eff}^{(2)} E_{inc}^{\omega_1} E_{inc}^{\omega_2} \tag{2.18}$$

then the effective susceptibility is

$$\chi_{eff}^{(2)}(\omega_1-\omega_2,\omega_1,\omega_2)=\frac{\int_V \chi_{MQW,zzz}^{(2)}(r)\frac{E_z^{\omega_1}(r)}{E_{inc}^{\omega_1}}\frac{E_z^{\omega_2}(r)}{E_{inc}^{\omega_2}}\frac{E_z^{\omega_{DFG}}(r)}{E_{inc}^{\omega_{DFG}}}dV}{V} \tag{2.19}$$

The $\chi_{MQW,zzz}^{(2)}$ is determined by the MQW material properties. Thus in the design of the nanoresonators, we only need to optimize the value of

$$\varsigma=\frac{\int_V \frac{E_z^{\omega_1}}{E_{inc}^{\omega_1}}\frac{E_z^{\omega_2}}{E_{inc}^{\omega_2}}\frac{E_z^{\omega_{DFG}}}{E_{inc}^{\omega_{DFG}}}dV}{V} \tag{2.20}$$

ς is called the overlap integral. The design of the nanoresonators has been optimized to achieve the best coupling of the normally incident pump waves with vertically polarized intersubband transitions and the out-coupling of the difference-frequency radiation to free space. The intensity conversion efficiency is definded as the output intensity devided by one of the input intensity.

Chapter 3: Prospect of Mid-IR Second Harmonic Generation in Polaritonic Intersubband Nonlinear Metasurfaces

3.1 INTRODUCTION

Our previous research has demonstrated that nonlinear metasurfaces based on the polaritonic coupling of electromagnetic modes in plasmonic nanocavities with quantum engineered intersubband nonlinearities in n-doped multi-quantum well (MQW) semiconductor heterostructures can produce a giant nonlinear response for the second harmonic generation [*9*]. The nonlinear conversion efficiency is 0.075%. To improve the conversion efficiency of SHG metasurface, new designs of MQW with other materials are explored. Here the $GaAs_{0.51}Sb_{0.49}/In_{0.53}Ga_{0.47}As/Al_{0.48}In_{0.52}As$ based MQWs and $GaAs_{0.51}Sb_{0.49}/In_{0.53}Ga_{0.47}As$ based MQWs are designed with expectations of high conversion efficiencies above 1 %.

3.2 MQW DESIGN

3.2.1 MQW Design Principles

Epitaxial Lattice Matching

Binary alloy is one with two components. Some typical binary alloy with Zincblende (diamond) crystal structures are GaAs, AlAs, InAs, GaSb, GaP, and InP. Ternary alloy is one with three components, such as $Al_{1-x}Ga_xAs$, $Al_{1-y}In_yAs$, and $In_{1-z}Ga_zAs$. Epitaxy refers to the deposition of a crystalline overlayer on a crystalline substrate [*24*]. Two typical substrates in III-V MQW growth are GaAs and InP. Epitaxy growth usually requires the materials have the same crystal structures and the lattice constants of the layer materials are nearly the same to reduce the strain in the grown

material. The lattice constant of some III-V materials and their alloy are shown in Fig. 3.1.

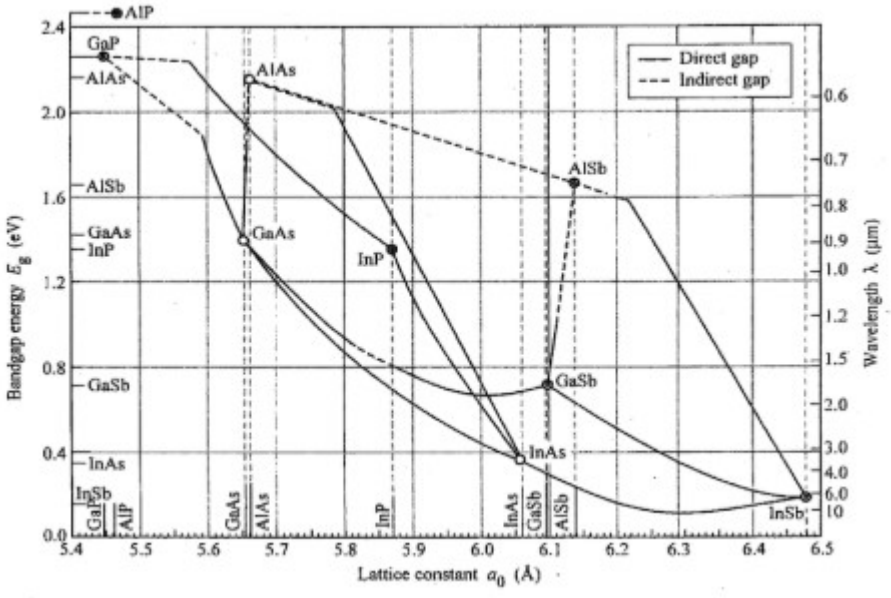

Figure 3.1: Bandgap versus lattice constant of III-V semiconductors [*25*].

By properly selecting the composition in the alloy to satisfy the lattice matching requirement, various III-V compound can be grown without strains.

Strained Structures

If the lattice matching is not satisfied in the epitaxial growth, there are strains induced between layers and the strain effect can modify the properties of materials [*26-28*]. The two types of strains have been shown in Fig. 3.2. If the thin layer lattice constant is greater than that of the substrate, the thin layer takes up the lattice spacing in the plane (compressive strain) and expands in the growth direction. If the thin layer lattice constant is smaller than that of the substrate, the thin layer takes up the lattice spacing in the plane (tensile strain) and compressed in the growth direction [*26*].

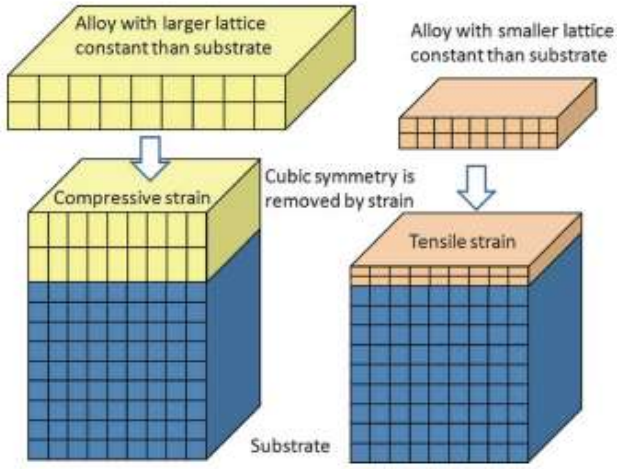

Figure 3.2: Schematic indicating the two types of strain when a thin layer is grown epitaxially on a substrate. If the thin layer lattice constant is greater than that of the substrate, the thin layer takes up the lattice spacing in the plane (compressive strain) and expands in the growth direction. If the thin layer lattice constant is smaller than that of the substrate, the thin layer also takes up the lattice spacing in the plane (tensile strain) and compressed in the growth direction [*26*].

3.2.2 MQW Design for the SHG metasurfaces

The quantum well structure for the nonlinear response was designed using a self-consistent *Poisson-Schrödinger* solver. In the program with predefined material ($In_{0.53}Ga_{0.47}As/Al_{0.48}In_{0.52}As$), the MQW energy level and dipole matrix element could be adjusted by tuning the thickness of layers and doing level. For a user-defined material, the band offset and effective electron mass are required. In order to improve the conversion efficiency of SHG metasurface, I have explored some new designs of MQW with other materials.

Here the MQW designs with $GaAs_{0.51}Sb_{0.49}/In_{0.53}Ga_{0.47}As/Al_{0.48}In_{0.52}As$ are demonstrated. The most important reason we choose this MQW system is that the

material linewidth ($2\hbar\gamma$~0.010 meV measured by the growth group) is supposed to be much narrower than our previous $In_{0.53}Ga_{0.47}As/Al_{0.48}In_{0.52}As$ system (~0.030 meV). This decrease in linewidth could lead to a dramatic increase in nonlinearity. The nonparabolicity parameters in Table 3.2 are estimated by matching the same E_p for all the materials used in the design.

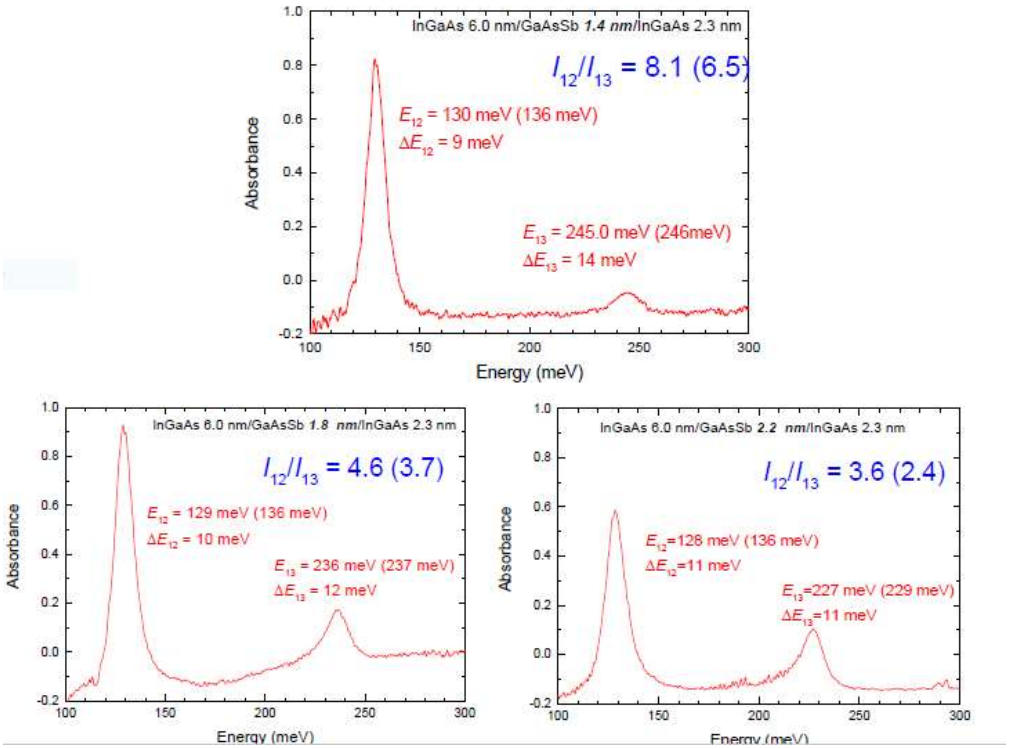

Figure 3.3: Absorption spectra of several $GaAs_{0.51}Sb_{0.49}/In_{0.53}Ga_{0.47}As/Al_{0.48}In_{0.52}As$ MQW heterostructures measured by the growth group. The material linewidth is ~0.010 meV.

	Effective electron mass (m_0^*)	Conduction Band offset (eV)	Nonparabolicity parameter (10^{-18})	Ep
GaAsSb(barrier)	0.045	0.36	1.0779	17.46
InGaAs(well)	0.043	0	1.18	17.46
AlInAs	0.076	0.52	0.3779	17.46

Table 3.1: The effective mass, band offset and nonparabolicity parameter of $GaAs_{0.51}Sb_{0.49}/In_{0.53}Ga_{0.47}As/Al_{0.48}In_{0.52}As$

With the above parameters, the thickness and doping level are tuned to optimize the second harmonic generation in the MQW. Two optimized designs are shown below. ez_{ij} is the transition dipole moment between state i and j. E_{ij} is the energy difference between state i and j.

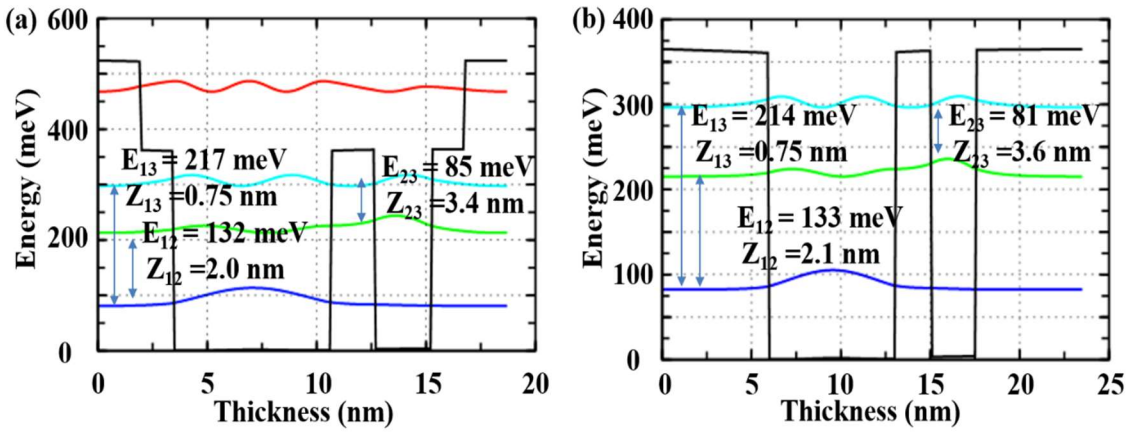

Figure 3.4: Conduction band diagrams of one period of designed MQW structures (a) $GaAs_{0.51}Sb_{0.49}/In_{0.53}Ga_{0.47}As/Al_{0.48}In_{0.52}As$ MQW structure band diagram (b) $GaAs_{0.51}Sb_{0.49}/In_{0.53}Ga_{0.47}As$ MQW structure band diagram

The MQWs are designed to display giant second harmonic generations with fundamental energy of 107.8 meV (26.1 THz, 11.5 μm). The conduction band diagrams of the two structures have been shown in Fig. 3.4. The E_{12} of both structures has been

detuned away from the fundamental energy to reduce saturation effect. Please note that the E_{12} need to be larger than the Fermi energy of the designed MQW to minimize the influence of thermal noise, usually around 50 meV (*2kT)* away. The growth sheets of the two structures are shown in Table 3.3 and Table 3.4. Please note the barrier thicknesses are optimized with anticrossing < 3 meV for the upper SHG states.

The estimated transition linewidth are $2\hbar\gamma_{12} = 0.010$ meV and $2\hbar\gamma_{13} = 0.014$ meV. For Fig. 3.4 (a), the saturation intensity is 4.0 MW/cm^2, the Fermi energy is 86.6 meV, the calculated nonlinearity $\chi^{(2)}_{MQW,zzz}(2\omega,\omega,\omega)$ is 455 nm/V, the overlap with CST simulation is 4.42, and the conversion efficiency is 1.2%. For Fig. 3.4 (b), the saturation intensity is 4.4 MW/cm2, the calculated nonlinearity $\chi^{(2)}_{MQW,zzz}(2\omega,\omega,\omega)$ is 362 nm/V, the overlap with CST simulation is 5.47, and the conversion efficiency is 1.2%. The calculated conversion efficiency is much larger than our previous SHG metasurfaces conversion efficiency (0.075%).

Matrix Layers

Layer	Material	[nm]	Ratio	Doping (cm-3)
1	InGaAs	300	In53Ga47As	
2	InP	100		
3	InGaAs	5	In53Ga47As	1.00E+18
4	GaAsSb	6	GaAs51Sb49	
	Start of 17 repeat periods			
5S1	GaAsSb	6	GaAs51Sb49	
6S1	InGaAs	7.1	In53Ga47As	2.20E+18
7S1	GaAsSb	2	GaAs51Sb49	
8S1	InGaAs	2.5	In53Ga47As	
9S1	GaAsSb	6	GaAs51Sb49	
	End of repeat periods			
10	GaAsSb	6	GaAs51Sb49	
11	InGaAs	5	In53Ga47As	1.00E+18

Table 3.2: $GaAs_{0.51}Sb_{0.49}/In_{0.53}Ga_{0.47}As$ MQW growth parameters. The semiconductor layers were grown on semi-insulating InP substrate.

Matrix Layers

Layer	Material	[nm]	Ratio	Doping (cm-3)
1	InGaAs	300	In53Ga47As	
2	InP	100		
3	InGaAs	5	In53Ga47As	1.00E+18
4	AlInAs	4	Al48In52As	
	Start of 21 repeat periods			
5S1	AlInAs	2	Al48In52As	
6S1	GaAsSb	1.5	GaAs51Sb49	
7S1	InGaAs	7.2	In53Ga47As	2.20E+18
8S1	GaAsSb	2	GaAs51Sb49	
9S1	InGaAs	2.6	In53Ga47As	
10S	GaAsSb	1.5	GaAs51Sb49	
11S1	AlInAs	2	Al48In52As	
	End of repeat periods			
12	AlInAs	4	Al48In52As	
13	InGaAs	5	In53Ga47As	1.00E+18

Table 3.3: $GaAs_{0.51}Sb_{0.49}/In_{0.53}Ga_{0.47}As/Al_{0.48}In_{0.52}As$ MQW growth parameters. The semiconductor layers were grown on semi-insulating InP substrate.

3.3 SUMMARY

In this work, I have designed two promising MQW structures for mid-IR second harmonic generations based on $GaAs_{0.51}Sb_{0.49}/In_{0.53}Ga_{0.47}As/Al_{0.48}In_{0.52}As$ systems. With the benefit of the narrow linewidth (~0.010 meV), the designed MQW structures are supposed to have large nonlinearities $\chi^{(2)}_{MQW,zzz}(2\omega,\omega,\omega)$ and dramatic increases in conversion efficiency. The theoretical calculations have predicted a conversion efficiency of 1.2%, which is 16 times larger than our previous SHG metasurfaces [*9*].

Chapter 4: Mid-IR Different Frequency Generation from Highly-Nonlinear Ultra-Thin Metasurfaces Coupled to Intersubband Transitions[1]

4.1 INTRODUCTION

Nonlinear intersubband polaritonic metasurfaces based on the coupling of quantum-engineered intersubband nonlinearities in semiconductor heterostructures with optical modes of plasmonic nanoantennas [*10, 29*] have achieved record-high (~0.075%) power conversion efficiencies for the second harmonic generation (SHG) using low-intensity (~10 kW/cm^2) illumination [*9*]. These metasurfaces provide orders of magnitude higher second-order nonlinear optical response compared to nonlinear metasurfaces based on other design principles, such as those employing the nonlinearities of metal nanoresonators, bulk nonlinear materials, or 2D materials [*13, 14, 30-34*]. They hold high promise to impact nonlinear optics applications due to their potential for achieving high levels of conversion efficiency under continuous-wave illumination [*9*], relaxed phase-matching constraints compared to bulk nonlinear crystals [*10*] and the ability to provide subwavelength control of the wavefront of the output beam [*8, 14, 35*].

Many practical applications of nonlinear materials involve sum- and difference-frequency mixing processes for new frequency generation, optical gating, and light upconversion for detection. Unlike intersubband SHG metasurfaces in which the plasmonic antennas can be easily designed to support strong resonances at frequencies ω

[1]Parts of this chapter have been published in Adv. Optical Mater. **2018**,1800681, where Yingnan Liu contribute to the design of MQW and nonlinear metasurface, sample fabrication, nonlinear optical characterization, and theoretical analysis. Stephen March contribute to the linear optical characterization. Nishant Nookala contribute to the design of MQW. John F. Klem contribute to the growth of MQW.

and 2ω for two orthogonal input polarizations [*9, 10*], the metasurfaces designed for sum- and difference-frequency generation (SFG and DFG, respectively) require antennas that support resonances at three different frequencies with significant field enhancement and good nonlinear modal overlap [*10*], which makes their design more challenging. On the other hand, since SFG and DFG processes employ two distinct input beams at different optical frequencies, SFG and DFG nonlinear metasurfaces have an additional design flexibility that helps to achieve high resonant optical nonlinearity while avoiding strong intensity saturation for at least one of the two pumps.

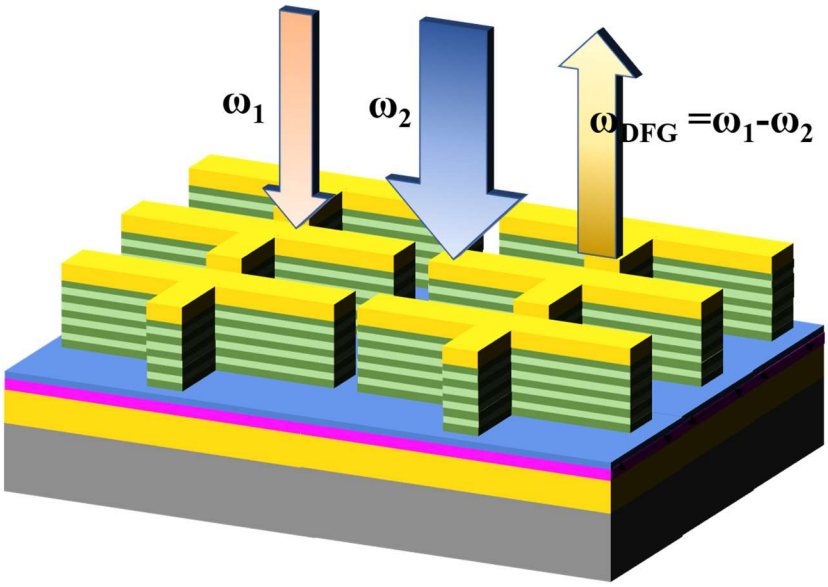

Figure 4.1: Schematic of the DFG process in the proposed metasurface.

Here I report the first nonlinear intersubband polaritonic metasurface designed for DFG. A 390-nm-thick metasurface was designed to achieve maximum nonlinear response for the pump wavelengths $\lambda_1 \approx 5.4$ μm and $\lambda_2 \approx 9.3$ μm to produce DFG output

at $\lambda_{DFG} \approx 12.9$ μm. An effective nonlinear susceptibility of up to 3.4×10^5 pm/V and nonlinear conversion efficiency of up to 0.43 mW/W^2 was achieved experimentally. Approximately 0.3% of $\lambda_1 \approx 5.4$ μm photons were down-converted to $\lambda \approx 12.9$ μm photons at the focal spot in our experiment. These results show that the design of the nonlinear intersubband polaritonic metasurfaces can be generalized to produce efficient DFG and SFG and that these metasurfaces are well-suited for the generation of long-wavelength infrared radiation (λ>12 μm) from shorter-wavelength (λ=3-12 μm) mid-infrared pumps as well as for an upconversion of long-wavelength infrared radiation to shorter wavelength via a related SFG process.

4.2 Metasurface Design and Simulations

4.2.1 MQW Design and Material Optical Absorption

The $In_{0.53}Ga_{0.47}As/Al_{0.48}In_{0.52}As$ quantum well structure for the nonlinear response was designed using a self-consistent Poisson–Schrödinger solver. The structure was designed to be resonant for the DFG process with pump photon energies of 250 meV and 136 meV, respectively. The layer sequence (in nanometer) is **2.5**/6.2/**1.4**/2.4/**2.5** where AlInAs barriers are shown in bold, and the first 1.5 nm of the first 2.5-nm-barrier and the last 1.5 nm of the last 2.5-nm-barrier are n-doped to 7.3×10^{18} cm^{-3}. The conduction band diagram of one MQW period is shown in Figure 4.2. ez_{ij} is the transition dipole moment between state i and j. E_{ij} is the transition energy between state i and j.

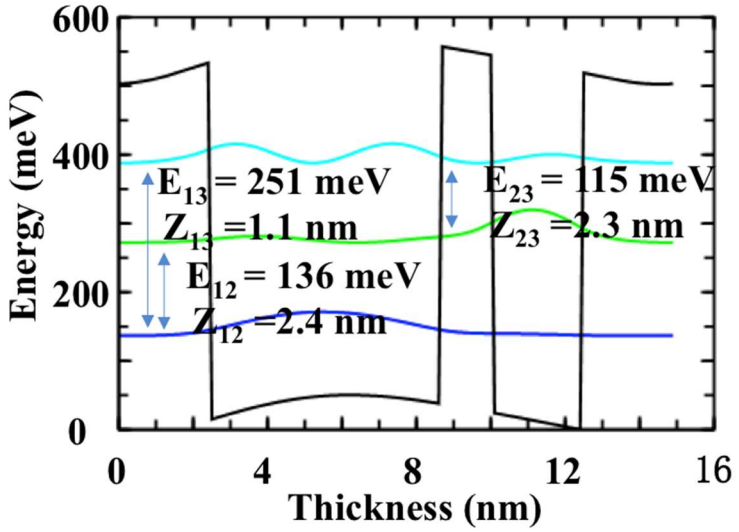

Figure 4.2：Conduction band diagram of one period of an $In_{0.53}Ga_{0.47}As/Al_{0.48}In_{0.52}As$ MQW structure. The layer sequence (in nanometer) is **2.5**/6.2/**1.4**/2.4/**2.5** where AlInAs barriers are shown in bold, and the first 1.5 nm of the first 2.5-nm-barrier and the last 1.5 nm of the last 2.5-nm-barrier are n-doped to 7.3×10^{18} cm−3

A 390-nm-thick MQW layer composed of 26 repetitions of the structure in Fig. 4.2 was grown by the molecular beam epitaxy on a semi-insulating InP substrate by our collaborators in Sandia Laboratories. The experimental absorption spectrum has been collected by the growth group and shown in Fig. 4.3. λ_{ij} is the photon wavelength. $2\hbar\gamma_{ij}$ is the measured transition linewidth. α_{ij} is the absorption coefficient. (A similar material absorption spectrum can also be measured in our lab with multi-pass geometry and will be introduced in Chapter 6.) The absorption spectrum of the grown structure indicates that the intersubband transition energies between the ground state and states 3 and 2 are 235 meV and 140 meV, slightly different from the design targets.

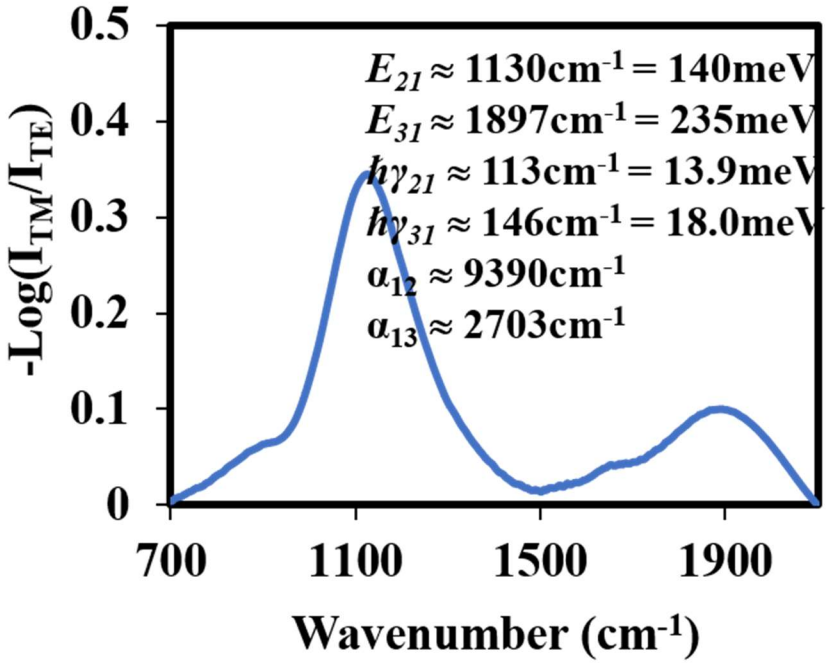

Figure 4.3: Absorption spectrum of the MQW heterostructure acquired by attenuated total reflectance (ATR) signal pass measurement. The frequencies of the absorption peaks that correspond to 1-2 and 1-3 transitions and their linewidth factors (half width at half maxima) are listed.

The value of α_{ij} allows us to estimate the active doping level. The absorption coefficient can be calculated with [*17*]:

$$\alpha(\omega) = 2\frac{\omega}{c}\mathrm{Im}(\sqrt{\varepsilon_{\perp}(\omega)}\sin^2(\theta) \tag{4.1}$$

The $\varepsilon_{\perp}(\omega)$ can be calculated with [*36, 37*]:

$$\varepsilon_{\perp}(\omega) \approx \varepsilon_{core}(\omega) + \frac{Ne^2z_{21}^2}{\epsilon_0\hbar(\omega_{21} - \omega - i\gamma_{21})} + \frac{Ne^2z_{31}^2}{\epsilon_0\hbar(\omega_{31} - \omega - i\gamma_{31})} \tag{4.2}$$

Here experimentally measured transition energy and transition linewidth (as shown in Fig. 4.3) are used, θ=60°. The value of calculated absorption coefficient $\alpha(\omega)$ can be tuned to approach the value of experimentally measured α_{ij} by changing the average doing level *N*. For the best match, we can get $N = 1.3 \times 10^{18}$ cm^{-3}.

The calculated magnitude of the heterostructure intersubband nonlinear susceptibility for the DFG process is shown in Figure 4.4 as a function of pump 1 frequency with the wavelength of pump 2 fixed at $\lambda_2 \approx 9.3$ μm. The wavelength λ_2 corresponds to the wavelength of a fixed-frequency high-power continuous-wave CO_2 laser in our laboratory.

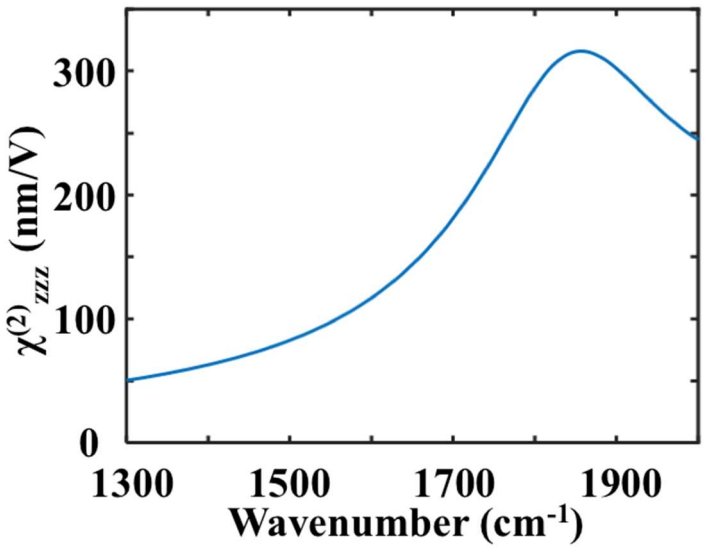

Figure 4.4: Calculated intersubband nonlinear susceptibility of the heterostructure in Fig. 4.2 as a function of the pump 1 wavenumber.

The value of $\chi^{(2)}_{MQW,zzz}$ shown in Figure 4.4 was calculated using the following equation [*11*]:

$$\chi^{(2)}_{MQW,zzz}(\omega_1-\omega_2,\omega_1,\omega_2)=\frac{e^3}{2\varepsilon_0\hbar^2}\left\{\frac{(N_1-N_2)z_{12}z_{23}z_{31}}{(\omega_{32}-\omega_1+\omega_2-i\gamma_{32})(\omega_{21}-\omega_2+i\gamma_{21})}\right. \quad (4.3)$$
$$-\frac{(N_1-N_3)z_{12}z_{23}z_{31}}{(\omega_{32}-\omega_1+\omega_2-i\gamma_{23})(\omega_{31}-\omega_1-i\gamma_{31})}$$
$$+\frac{(N_1-N_3)z_{12}z_{23}z_{31}}{(\omega_{21}-\omega_1+\omega_2-i\gamma_{21})(\omega_{31}-\omega_1-i\gamma_{31})}$$
$$\left.+\frac{(N_2-N_3)z_{23}z_{31}z_{12}}{(\omega_{12}+\omega_1-\omega_2+i\gamma_{12})(\omega_{32}-\omega_2+i\gamma_{32})}\right\}$$

where ω_1 and ω_2 are the pump frequency of the pump 1 (QCL) and pump 2 (CO_2 laser), respectively, e is the electron charge, N_1, N_2, N_3 are the populations of the first three energy subbands in the MQW structure, ez_{ij}, $\hbar\omega_{ij}$, $\hbar\gamma_{ij}$ are the transition dipole moment, transition energy, and the transition linewidth between states i and j (the values of z_{ij} and $E_{ij}= \hbar\omega_{ij}$ are shown in Fig. 4.3). For the calculations shown in Fig. 4.4, I assumed that all the electrons are in the ground state and used the experimentally-measured values of N_1 = 1.3×10^{18} cm^{-3}, $\hbar\omega_{31}$=235 meV, $\hbar\omega_{21}$=140 meV, $\hbar\gamma_{21}$=13.9 meV, and $\hbar\gamma_{31}$=18.0 meV. I further assumed $\hbar\gamma_{32}$ =15.0 meV for calculation. The calculations further assume low-intensity illumination and neglect saturation effects. The simulated maximum response is around 315 nm/V at 1850 cm^{-1}.

4.2.2 Nanoresonator Design and Simulations

Nanoresonator Optimization Results

The MQW layer is sandwiched between a metal ground plane and an array of etched T-shaped nanoresonators with their top surfaces coated with Ti/Au. The MQW-filled nanoresonators are designed to resonate at all three input/output frequencies. Various dimensions can be tuned to optimize the value of the overlap integral, such as width/length of the resonator, the gap between two resonators. The simulation results are obtained with the electromagnetic simulation software (CST Studio).

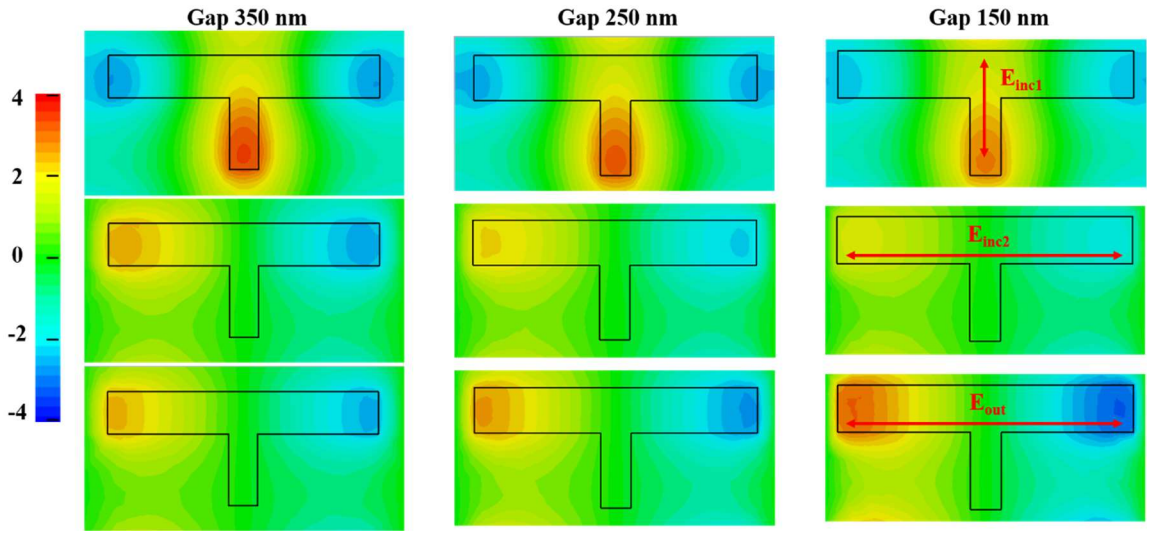

Figure 4.5: The simulated Ez field enhancement with varies gap sizes at the two pump frequencies and the difference-frequency monitored in the MQW layer 200 nm below the top metal surface of the nanoresonator. The color code shows the field enhancements in the MQW heterostructure relative to the electric-field amplitudes in the incoming waves.

Since we etched the MQW into T shape, only T shape area has a strong nonlinear response and contributes to the effective susceptibility. Thus the overlap is integrated over T shape area where $\chi^{(2)}_{MQW,zzz}$ is nonzero. However, V in the denominator is still the whole unit cell, including the gap volume. In Fig. 4.6, the dimensions of the resonators are fixed and the gap is the variable. The overlaps of the three designs in Fig. 4.5 are 1.26, 1.32, 1.44 respectively. As we increase the gap size, the area contributes to the integration remains the same while unit cell size V increases. This causes a decrease in the overlap, which indicates a small gap size is preferred in our metasurface design.

Besides, the width and length of the resonators are also tuned to be on the resonance of input two beams frequencies and output DFG frequency. However, the degrees of freedom with T shape resonators don't allow a perfect match for all three

resonance. The best nanoresonator design is evaluated by maximizing the overlap integral. The optimized unit cell of the metasurface is represented in Figure 4.6.

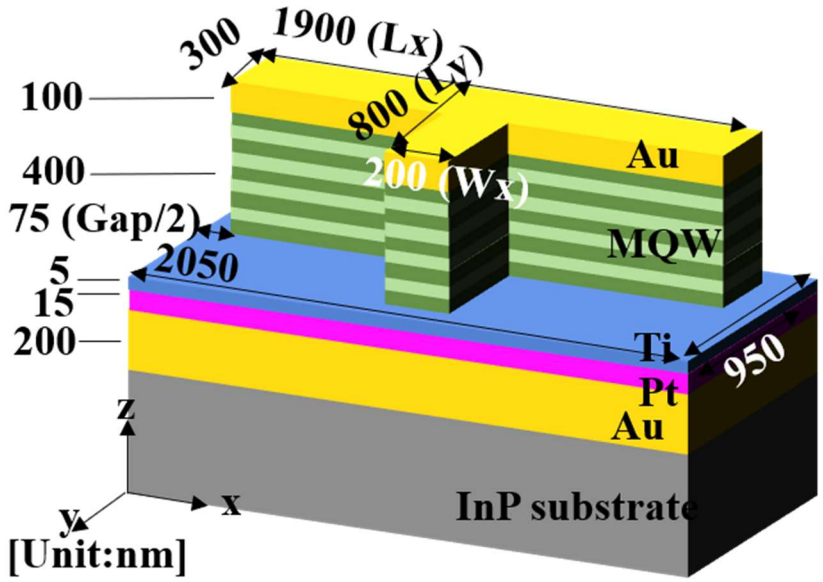

Figure 4.6： Nonlinear metasurface structure. A 0.95 μm by 2.05 μm metasurface unit-cell.

Figure 4.7 (a) shows the simulated absorption spectra of the metasurface under x- and y-polarized plane wave illumination at normal incidence. The absorption spectra can be extracted from the reflection coefficient S_{11} in the simulation. Since $S_{11}^2 = \frac{I_{ref}}{I_{bg}}$, the spectra can be attained with $1 - S_{11}^2$. Strong resonances for a y-polarized wave at $\lambda_1 \approx 5.4$ μm and an x-polarized wave at $\lambda_{DFG} \approx 12.9$ μm, as well as a weaker resonance for the x-polarized wave at $\lambda_2 \approx 9.3$ μm are visible in the spectra. Figure 4.7 (b) shows the enhancement of the z-polarized electric field in the MQW layer 200 nm below the top gold surface of the antenna compared to the amplitudes of the incident wave for the case of three frequencies involved in the DFG process.

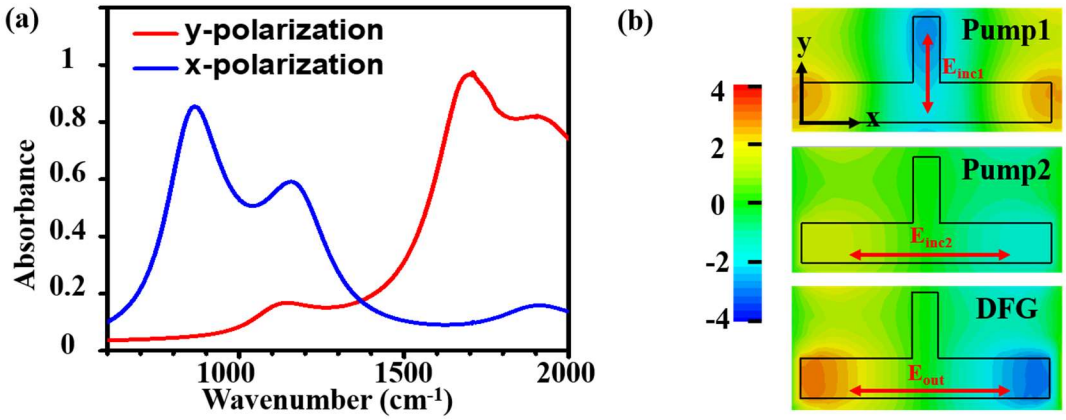

Figure 4.7: Numerical simulations of the intersubband nonlinear metasurfaces for DFG. (a) The simulated normal-incidence absorption spectrum of the metasurfaces made of the unit cells shown in Fig. 1(d) for different light polarizations. (b) The simulated Ez field enhancement at the two pump frequencies and the difference-frequency monitored in the MQW layer 200 nm below the top metal surface of the nanoresonator. The color code shows the field enhancements in the MQW heterostructure relative to the electric-field amplitudes in the incoming waves.

For this nano-resonator design, the highest overlap is 1.44 for the input/output polarizations used in the simulations in Figure 4.7 (b). Under low-intensity illumination (neglecting intensity saturation of the intersubband nonlinearity), we have $\chi_{xyx}^{(2)\mathrm{eff}} \approx 450$ nm/V for the DFG process with $\lambda_1 \approx 5.4$ μm and $\lambda_2 \approx 9.3$ μm pumps. This value is approximately 1.5 times larger than the intersubband nonlinearity $\chi_{MQW,zzz}^{(2)}$ plotted in Fig. 4.4. Other metasurface $\chi^{(2)}$-tensor components are computed to be at least 20 times smaller.

Saturation Effect in the DFG Metasurfaces

For all previous analysis for DFG metasurfaces, we have ignored the saturation effects. However, the saturation effect plays an important role when pump intensity increase intensely. In equation (4.3), when pump intensity is weak, N_2 and N_3 are much smaller than N_1. In this case, $N_1 \approx N_e$, where N_e is the total doped electron density. When pump intensity increases, more and more electrons are transferred from the fundamental energy level to higher energy levels, which will cause a decrease in the value of $\chi^{(2)}_{MQW,zzz}$ and cause saturation in the output DFG power. The populations of different subbands under high pump intensity are derived below. Only the first three energy levels of the conduction band are considered. $I_z^{\omega_1}$, $I_z^{\omega_2}$ are two pump intensities from state 1 to state 2, and state 2 to state 3 respectively. $\alpha_{ij}(\omega_p)$ is the absorption coefficient between state i and j at the frequency ω_p. N_1, N_2, N_3 are the populations of the first three energy subbands in the MQW structure, ez_{ij}, $\hbar\omega_{ij}$, $\hbar\gamma_{ij}$ are the transition dipole moment, transition energy, and the transition linewidth between states i and j. τ_{ij} is the relaxation time between state i and j, calculated with self-consistent Poisson-Schrödinger solver based on Frohlich model. τ_{12}= 2.07 ps, τ_{13}=1.94 ps, τ_{23}= 1.53 ps. Here the pump intensity from state 2 to state 3 is neglected.

The rate equations are given as

$$\begin{cases} \dfrac{dN_1}{dt} = \dfrac{-\alpha_{12}(\omega_1)I_z^{\omega_1}}{\hbar\omega_1} + \dfrac{-\alpha_{13}(\omega_2)I_z^{\omega_2}}{\hbar\omega_2} + \dfrac{N_2}{\tau_{12}} + \dfrac{N_3}{\tau_{13}} \\ \dfrac{dN_2}{dt} = \dfrac{\alpha_{12}(\omega_1)I_z^{\omega_1}}{\hbar\omega_1} - \dfrac{N_2}{\tau_{12}} + \dfrac{N_3}{\tau_{23}} \\ \dfrac{dN_3}{dt} = \dfrac{\alpha_{13}(\omega_2)I_z^{\omega_2}}{\hbar\omega_2} - \dfrac{N_3}{\tau_{13}} - \dfrac{N_3}{\tau_{23}} \end{cases} \tag{4.4}$$

For steady state，

$$\begin{cases} -\dfrac{\alpha_{12}(\omega_1)I_z^{\omega_1}}{\hbar\omega_1} - \dfrac{\alpha_{13}(\omega_2)I_z^{\omega_2}}{\hbar\omega_2} + \dfrac{N_2}{\tau_{12}} + \dfrac{N_3}{\tau_{13}} = 0 \\ \dfrac{\alpha_{12}(\omega_1)I_z^{\omega_1}}{\hbar\omega_1} - \dfrac{N_2}{\tau_{12}} + \dfrac{N_3}{\tau_{23}} = 0 \\ \dfrac{\alpha_{13}(\omega_2)I_z^{\omega_2}}{\hbar\omega_2} - \dfrac{N_3}{\tau_{13}} - \dfrac{N_3}{\tau_{23}} = 0 \end{cases} \tag{4.5}$$

Since $\alpha_{ij}(\omega) = \frac{(N_i - N_j)\alpha_{ij}^{(0)}}{N}$, where $\alpha_{ij}^{(0)}$ is the absorption coefficient with all carriers on state i, we can get:

$$\begin{cases} -\dfrac{(N_1 - N_2)\alpha_{12}^{(0)}I_z^{\omega_1}}{N\hbar\omega_1} - \dfrac{(N_1 - N_3)\alpha_{13}^{(0)}I_z^{\omega_2}}{N\hbar\omega_2} + \dfrac{N_2}{\tau_{12}} + \dfrac{N_3}{\tau_{13}} = 0 \\ \dfrac{(N_1 - N_2)\alpha_{12}^{(0)}I_z^{\omega_1}}{N\hbar\omega_1} - \dfrac{N_2}{\tau_{12}} + \dfrac{N_3}{\tau_{23}} = 0 \\ \dfrac{(N_1 - N_3)\alpha_{13}^{(0)}I_z^{\omega_2}}{N\hbar\omega_2} - \dfrac{N_3}{\tau_{13}} - \dfrac{N_3}{\tau_{23}} = 0 \end{cases} \tag{4.6}$$

Set

$$\begin{cases} I_{12}^{sat} = \dfrac{N\hbar\omega_1}{2\tau_{12}\alpha_{12}^{(0)}} \\ I_{13}^{sat} = \dfrac{N\hbar\omega_2}{2\tau_{13}\alpha_{13}^{(0)}} \end{cases} \tag{4.7}$$

Then the relationships between populations of different levels are

$$\begin{cases} N_1 = N_3\left(1 + \dfrac{2I_{13}^{sat}}{I_z^{\omega_2}} + \dfrac{2I_{13}^{sat}\tau_{13}}{I_z^{\omega_2}\tau_{23}}\right) \\ N_2 = \dfrac{N_3\left(1 + \dfrac{2I_{13}^{sat}}{I_z^{\omega_2}} + \dfrac{2I_{13}^{sat}\tau_{13}}{I_z^{\omega_2}\tau_{23}} + \dfrac{2I_{12}^{sat}\tau_{12}}{I_z^{\omega_1}\tau_{23}}\right)}{1 + \dfrac{2I_{12}^{sat}}{I_z^{\omega_1}}} \\ N_1 + N_2 + N_3 = N \end{cases} \tag{4.8}$$

For each pump intensity, the population N_1, N_2, and N_3 can be calculated with the above formula, so as the DFG susceptibility. However, due to the non-uniform field enhancement of plasmonic nanocavities, the pump intensity inside the MQW is

dependent on the position. The pump intensity of every position is calculated with simulation software CST STUDIO SUITE, and the effective DFG susceptibility is calculated by integrated DFG susceptibility of all positions with equation (2.19). The output DFG power is

$$I_{DFG} = \frac{(\omega_{DFG}\chi_{eff}^{(2)}d)^2 I_{inc}^{\omega_1} I_{inc}^{\omega_2}}{2\varepsilon_0 c^3} \tag{4.9}$$

where d is the thickness of MQW.

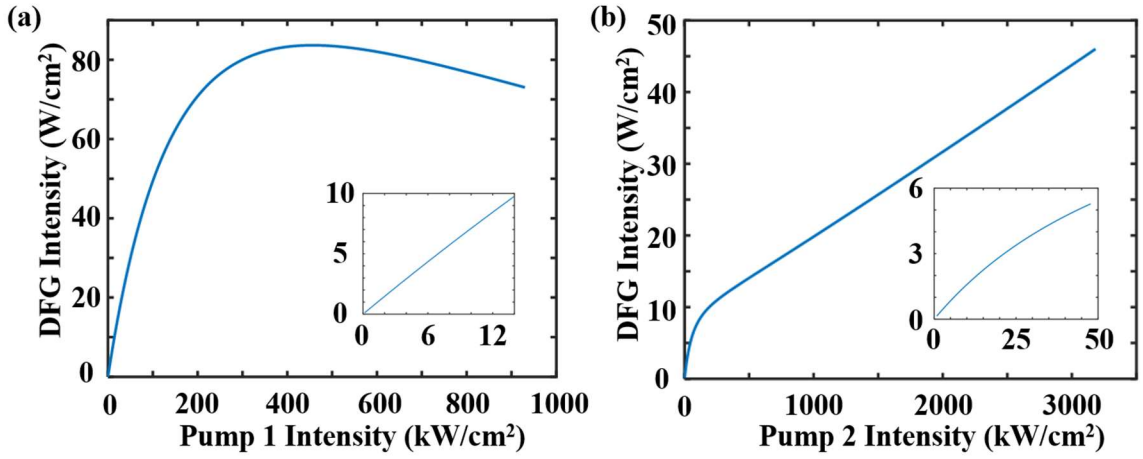

Figure 4.8: (a) Simulations of the DFG intensity output versus pump 1 intensity with pump 1 polarized in y-direction at 1850 cm-1($\lambda_1 \approx 5.4$ μm). Pump 2 is polarized in the x-direction and its intensity is fixed at 159 kW/cm2. Pump 2 wavelength is $\lambda_2 \approx 9.3$ μm ($1/\lambda_2 \approx 1075$ cm^{-1}). (b) DFG intensity versus pump 2 intensity with pump 2 polarized in the x-direction at 1075 cm^{-1}. Pump 1 is polarized in the y-direction and its intensity is fixed at 13.4 kW/cm2. Pump 1 wavelength is $\lambda_1 \approx 5.4$ μm ($1/\lambda_1 \approx 1850$ cm^{-1}). The simulations in panels (a) and (b) include intensity saturation of optical nonlinearity as discussed in the text.

We assume the impinging waves are plane waves to simplified the simulations. Fig. 4.8 (a, b) show the computed DFG intensity versus pump 1 intensity and pump 2

intensity respectively, including the saturation effect. As illustrated in Fig. 4.8 (a), the DFG intensity gradually saturates when pump 1 increases above ~300 kW/cm^2. Fig. 4.8 (b) shows a clear saturation of the DFG power when pump 2 intensity is around 100 kW/cm^2. The insets show the DFG intensity dependence as the function of pump 1 intensity and pump 2 intensity, respectively, for a range of intensities used in our experiment. In the insets, the DFG intensity has a linear relationship with pump 1 intensity and a nearly linear dependence on pump 2 intensity.

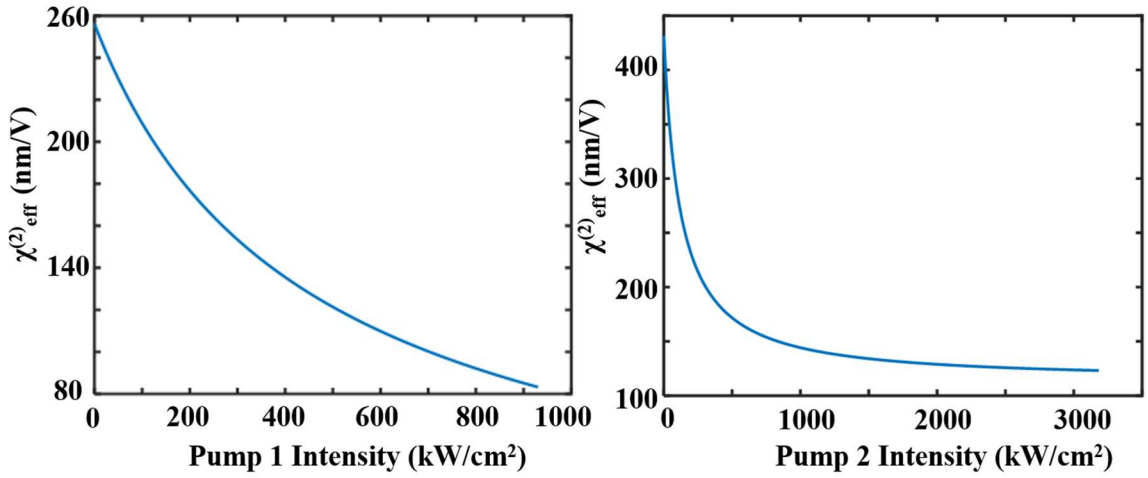

Figure 4.9: (a) Simulations of the DFG susceptibility versus pump 1 intensity with pump 1 polarized in y-direction at 1850 cm^{-1}(λ_1≈5.4 μm). Pump 2 is polarized in the x-direction and its intensity is fixed at 159 kW/cm2. Pump 2 wavelength is λ_2≈9.3 μm (1/ λ_2≈1075 cm^{-1}). (b) Simulations of the DFG susceptibility versus pump 2 intensity with pump 2 polarized in the x-direction at 1075 cm^{-1}. Pump 1 is polarized in the y-direction and its intensity is fixed at 13.4 kW/cm2. Pump 1 wavelength is λ_1≈5.4 μm (1/ λ_1≈1850 cm^{-1}).

The effective susceptibility $\chi^{(2)}_{eff}$ is shown in Fig. (4.9). As the pump intensity increases, the $\chi^{(2)}_{eff}$ decreases dramatically. We note that, due to high computational complexity, our simulations do not include the effect of the MQW bandstructure change

due to different charge distribution in the upper states. This analysis warrants further studies that are beyond the scope of this project.

4.3 Device Fabrication

A 400 nm–thick MQW structure as designed in Fig. 4.2 was grown by molecular beam epitaxy (MBE) on a semi-insulating InP substrate. The wafer was deposited with gold on top and transferred to another gold-coated InP substrate by wafer bonding. The original substrate was then removed by wet etch. There were 25 (5×5) different patterns on this sample, and each pattern was formed by 200 μm × 200 μm array of the same plasmonic nanoresonators. Based on our previous experience with the second harmonic generation metasurfaces, the absorption peak positions of the fabricated structures are typically red-shifted by 10-15% compared to the simulation results. The difference between the theory and experiment is likely due to the real materials parameters being slightly different from that assumed in simulations. To account for this uncertainty, we fabricated metasurfaces with variations in antenna dimensions. The patterns were fabricated by e-beam evaporation of gold, PECVD growth of SiN, e-beam lithography, and plasma etching. The plasma etching went through the top layer gold and the MQW layer. The whole fabrication process is illustrated in Fig. 4.10.

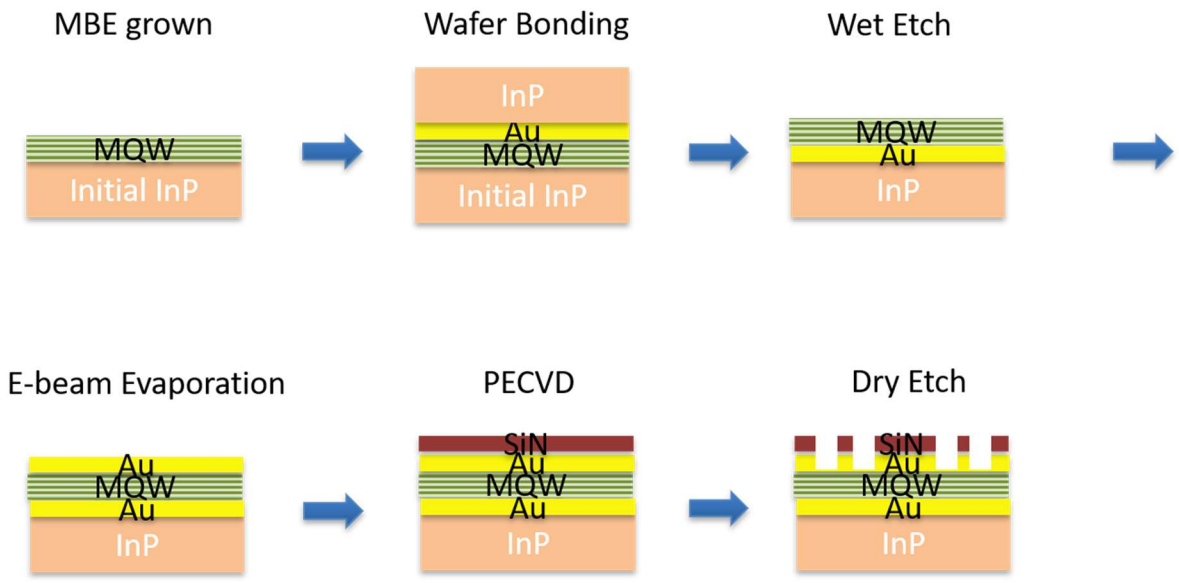

Figure 4.10: Schematic of the metasurface fabrication process

MQW Growth

The two alloys of the MQW, $In_{53}Ga_{47}As$ and $Al_{48}In_{52}As$, are lattice-matched. The MQW was grown with MBE and the growth sheet is shown below. The repeated periods are the active nonlinear region. On top of the active region, there are 300 nm InGaAs and 100 nm InP, which is the etch stop layer. The etch stop layer is essential for the substrate removel process and is explained in the substrate removal part.

Matrix Layers				
Layer	**Material**	**[nm]**	**Ratio**	**Doping (cm-3)**
1	InGaAs	300	In53Ga47As	
2	InP	100		
3	InGaAs	5	In53Ga47As	
4	AlInAs	1	Al48In52As	
5	AlInAs	1.5	Al48In52As	7.30E+18
	Start of 26 repeat periods			
6S1	AlInAs	1.5	Al48In52As	7.30E+18
7S1	AlInAs	1	Al48In52As	
8S1	InGaAs	6.2	In53Ga47As	
9S1	AlInAs	1.4	Al48In52As	
10S1	InGaAs	2.4	In53Ga47As	
11S1	AlInAs	1	Al48In52As	
12S1	AlInAs	1.5	Al48In52As	7.30E+18
	End of repeat periods			
13	AlInAs	1.5	Al48In52As	7.30E+18
14	AlInAs	1	Al48In52As	
15	InGaAs	5	In53Ga47As	

Table 4.1: $In_{0.53}Ga_{0.47}As/Al_{0.48}In_{0.52}As$ MQW growth parameters. The semiconductor layers were grown on semi-insulating InP substrate.

Thermocompression Bonding

The thermocompression bonding is achieved by the diffusion occurs between two metals with atomic contact. It typically involves three steps: pre-conditioning, deposition, and bonding. The grown MQW on initial InP substrate was cleaned by oxygen plasma in Oxford RIE (Reactive Ion Etching). The recipe is O_2 50sccm, chamber pressure 50 mtorr, RF power 75W, time 2 mins. This step is to remove polymer residues on the surface. Then the sample was dipped into buffered oxide etchant (BOE) for ~10 s. The BOE we used is a diluted hydrofluoric acid (HF) etchant. This step can remove surface oxides and also improve surface adhesion. Another bare InP substrate was also cleaned with these two steps. The cleaned bare InP substrate and the cleaned MQW sample wafer were deposited with 5 nm titanium, 15 nm platinum and 200 nm gold on top by e-beam

evaporation. The titanium layer is used to improve the adhesion between other metal and the sample surface. The platinum layer is a protective layer that forbids potential diffusion into MQW during high-temperature wafer bonding. The two wafers were cut into the same size (usually a quarter of the 2-inch wafer), blown with N_2 gas, aligned along the crystallographic direction face to face and placed in tungsten plate of AML wafer bonder. After closing the chamber, the plate was lifted gradually to increase the force on the sample to ~100 N. This is to maintain the position of the sample under the vibration during chamber evacuation. When the chamber was evacuated to 5×10^{-4} torr and the temperature of both the upper and lower plate reached 315 °C, I increased the clamping force to 4500 N and let it maintain for 15 min. Then the samples were cooled down to 200 °C and removed from the chamber.

Substrate Removal

The initial InP substrate was mechanically polished to thin down the thickness. The sample, with initial InP substrate face up, was bonded to a glass slide by crystal glue. Then the glass was bonded to a metal block by crystal glue. The crystal glue becomes liquid with a temperature around 190 °C and becomes solid after cooled down to the room temperature. The main role of the glass slide is to provide a smooth surface. The initial thickness of the whole sample was measured and recorded. The initial thickness of InP was 350 μm and should be thinned down to 100~150 μm. A thick and smooth glass plate was cleaned with DI water. SiC gel was mixed with water on the glass plate, and then the sample was gently pressed and polished in the SiC gel. The uniformity of the polished surface is critical to the success of the next wet etch step. After polishing, the thickness differences among the different area of the sample surface need to be less than

0.02 mm. The polished sample was removed from the metal block and the glass slide, and cleaned with acetone and IPA.

The remaining InP on the sample and the growth stop layer of MQW need to be removed by wet etch. The sample was bonded to a glass slide with crystal glue, and the sample edge was also covered with glue. The glue can protect the backside and the edge from the etchant. This sample was dipped into HCl : DI water = 3(300 ml) : 1(100 ml) for 10~15 mins. InP etch rate is ~10 μm/min in this solution, and the etch stop at $In_{0.53}Ga_{0.47}As$ layer. Perfect removal of the InP can be clearly noticed when the sample surface is shiny. The existence of the etch stop layer help us to control the etch time with visible phenomena. The etched sample was cleaned with DI water. The next step was to remove the etch stop layer. The top 300 nm InGaAs layer was etched by dipping in H_3PO_4 : H_2O_2 : DI water = 1(50ml) : 1(50ml) : 38(1900ml) solution for about 2.5 mins. The $In_{0.53}Ga_{0.47}As$ etch rate in this solution is ~2 nm/s and the etch stop at the 100 nm InP layer. The surface color becomes uniform (purple for 400 nm MQW) after complete removal of the InGaAs layer. The etched sample was then cleaned with DI water. The remained 100 nm InP layer was removed by dipping into HCl : DI water = 3(300 ml) : 1(100 ml) for a few seconds and the surface became shiny again. The sample was then cleaned with DI water. We have fully removed the initial InP substrate and the etch stop layer.

PECVD and E-beam Lithography

After wet etch, 5 nm titanium and 100 nm gold were deposited on top of the sample. Since the sample after wet etches had a clean surface, and there was no need to repeat the clean steps. (If the wet etch and deposition are performed in different days, then the two clean steps described before is necessary.) Now we got a sandwiched structure with a 400 nm

MQW layer between two metal layers. To make nanoresonators, we need to etch through the top gold layer and the MQW layer.

A layer of SiN was deposited on the top by plasma-enhanced chemical vapor deposition (PECVD). The deposition rate is 17 nm/min. This SiN serves as the etch mask. The SiN should be thick enough to survive through the whole etching process of MQW and metals. Plasma treatment (Oxford RIE, O_2 20 sccm, chamber pressure 50 mtorr, RF power 150 W, time 15 mins) has been applied to the sample surface to enhance the adhesion. Positive e-beam resist ZEP was spin-coated (4000 rpm, 1 min) on the surface and baked at 180 °C for 2 min. The sample was written with designed patterns by JEOL 6000 FSE EBL (EOS7, 100pA, area dose: 180μC/cm2, line dose: 0.12nC/cm, shot module: -40). The exposed sample was developed in Amyl-acetate for 1 min 15 s and rinsed with IPA. The ZEP residue is cleaned in Oxford RIE (O_2 20 sccm, chamber pressure 50 mtorr, RF power 70 W, time 20 s).

Plasma Etching

SiN is etched in Oxford RIE (CHF_3 20 sccm, O_2 4 sccm, RF power 300 W, chamber pressure 50 mtorr) with ZEP as the etch mask. The etch rate of SiN is 46 nm/min. After the patterns were transferred to SiN, the ZEP is cleaned with Oxford RIE (O_2 50 sccm, chamber pressure 50 mtorr, RF power 70 W, time 30 min) and acetone (1 h). (Sonication in acetone for 1~3 s if the sample is still not clean.) The top gold layer and MQW are etched in Oxford ICP (Cl 10 sccm, CH_4 8 sccm, H_2 4 sccm, RF power 100 W, ICP Generator 1200W, Set pressure 4mtorr, temperature 60 °C). For this recipe, the etch rate of SiN is 46 nm/min, the etch rate of gold is 50 nm/min, and the etch rate of MQW is 200 nm/min. After the etching, the sample was dipped in the BOE for a few seconds to remove the SiN residue.

The scanning electron microscope (SEM) images of the fabricated nano-resonator array are shown in Fig. 4.11.

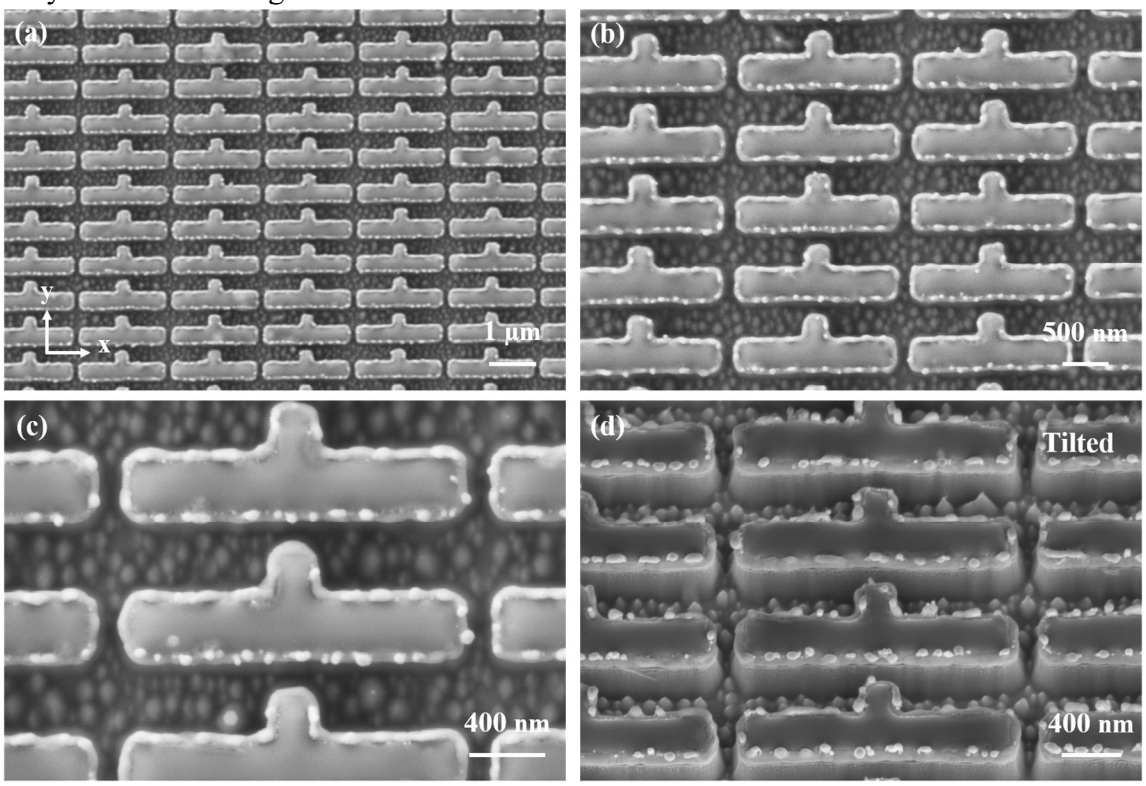

Figure 4.11: The SEM image of the fabricated metasurface. (a) (b) and (c) are the top-view SEM images of the metasurface with different field scales. (d) is the tilted view of the metasurface.

4.4 Experimental Characterization

Linear Absorption Spectrum

The absorption spectra of this metasurface for x- and y-polarized input light were measured with Bruker FTIR spectrometer. Please note that there are typically two forms of displaying the absorption spectra, which are $-log(\frac{I_{ref}}{I_{bg}})$ and $1-\frac{I_{ref}}{I_{bg}}$, where I_{ref} is the reflected beam intensity on pattern area, I_{bg} is the reflected beam intensity on gold

with no patterns. Here the second form $1 - \frac{I_{ref}}{I_{bg}}$ is used, and it can be directly compared with the previous theoretical analysis.

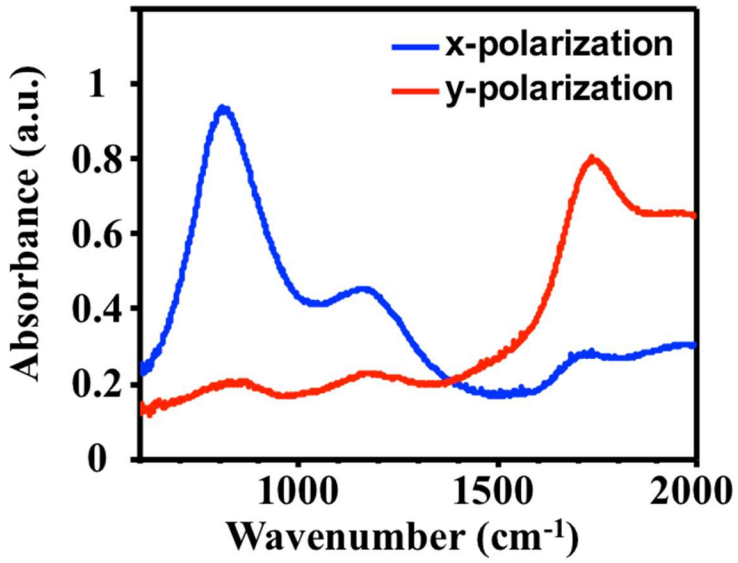

Figure 4.12: Reflection-absorption spectrum of the fabricated metasurface at normal incidence for light polarized along x-axis and y-axis.

The metasurface antenna with the long arm length of 1800 nm, the short arm length of 600 nm, and the short arm width of 250 nm produces three resonances that are best-matched the theoretical simulations in Fig. 4.7 (a). As shown in Fig. 4.12, the strong absorption peaks around $\lambda_1 \approx 5.4$ μm and $\lambda_{DFG} \approx 12.9$ μm, and a weaker peak at $\lambda_2 \approx 9.3$ μm are observed.

Experimental Setup

The DFG measurements of the metasurface were performed using the setup shown in Fig. 4.13. A non-tunable continuous-wave CO_2 laser and a linear-polarized pulsed QCL were used as pump sources. The QCL and the CO_2 laser were placed with

orthogonal polarization. A short pass filter was used as a beam splitter to combine the two beams. The beams were reflected by a LP filter and passed through a collimating lens (numerical aperture 0.5) to the sample. The DFG output was collected by the same lens, and then passed through a LP filter and a ZnSe lens to the detector.

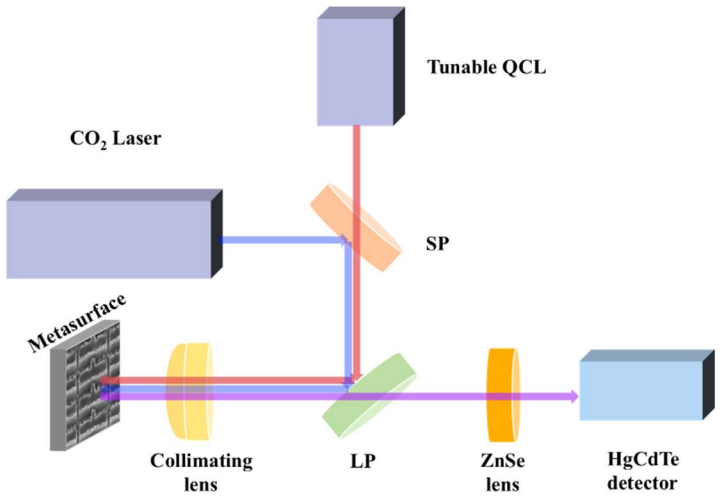

Figure 4.13: Optical set-up for metasurface characterization. A linear polarized tunable QCL and a non-tunable CO_2 laser were placed with orthogonal polarization. A short pass filter was used as a beam splitter to combine the two beams. The beams were reflected by a LP filter and passed through a numerical aperture 0.5 collimating lens to the sample. The DFG output was collected by the same lens, and then passed through a LP filter and a ZnSe lens to the detector.

Here we assume both input beams are Gaussian beams with the intensity distribution $I_i(r) = I_{0i} e^{-\frac{2r^2}{w_{0i}^2}}$ on the sample, where w_{0i} is the focal spot radius of beam i (i=1, 2 for pumps 1 and 2, respectively, or i=DFG for the DFG beam). The radii of the focal spots of the two pumps on the sample were measured to be w_{01}≈37 μm and w_{02}≈20 μm and for the QCL and the CO_2 laser, respectively, using the knife-edge technique.

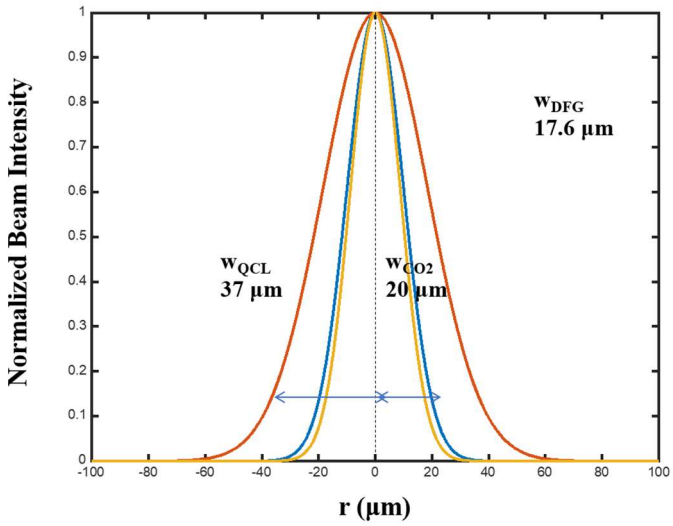

Figure 4.14: The normalized beam intensity distribution of the three Gaussian beams. The red curve represents the QCL beam. The blue curve represents the CO_2 laser beam. The yellow curve represents the DFG beam.

From equation (4.9), we can easily get

$$I_{DFG}(r) = \frac{(\omega_{DFG}\chi_{eff}^{(2)}d)^2 I_{01}^{\omega_1} I_{02}^{\omega_2}}{2\varepsilon_0 c^3} e^{-\frac{2r^2}{w_{01}^2}} e^{-\frac{2r^2}{w_{02}^2}} \tag{4.10}$$

$$I_{DFG}(r) = \frac{(\omega_{DFG}\chi_{eff}^{(2)}d)^2 I_{01}^{\omega_1} I_{02}^{\omega_2}}{2\varepsilon_0 c^3} e^{-2r^2(\frac{1}{w_{01}^2}+\frac{1}{w_{02}^2})} \tag{4.11}$$

From equation (4.11), we know the distribution of the DFG intensity on the metasurface is also a Gaussian distribution. If we set

$$I_{DFG}(r) = I_0^{DFG} e^{-\frac{2r^2}{w_{DFG}^2}} \tag{4.12}$$

then we get

$$\begin{cases} I_0^{DFG} = \dfrac{(\omega_{DFG}\chi_{eff}^{(2)}d)^2 I_{01}^{\omega_1} I_{02}^{\omega_2}}{2\varepsilon_0 c^3} \\ \dfrac{1}{w_{DFG}^2} = \dfrac{1}{w_{01}^2} + \dfrac{1}{w_{02}^2} \end{cases} \tag{4.13}$$

The calculated DFG radius is 17.6 μm. For Gaussian beam,

$$I_0 = \frac{2P_0}{\pi w^2} \tag{4.14}$$

where the P_0 is the total power.

Dual-beam alignment

The beam radii of QCL and CO_2 laser at the focal point are 37 μm and 20 μm, respectively. Since each pattern on the metasurface is 200 μm × 200 μm, the input beam sizes are much smaller than the metasurface pattern size, we couldn't align the two beams directly with the reflected signal from the metasurface patterns. A sample designed for alignment with different size of gold circular patterns on a Si substrate was shown in Fig. 4.15. The radius of the small circular pattern is 20 μm, and the radius of the large circular pattern is 45 μm.

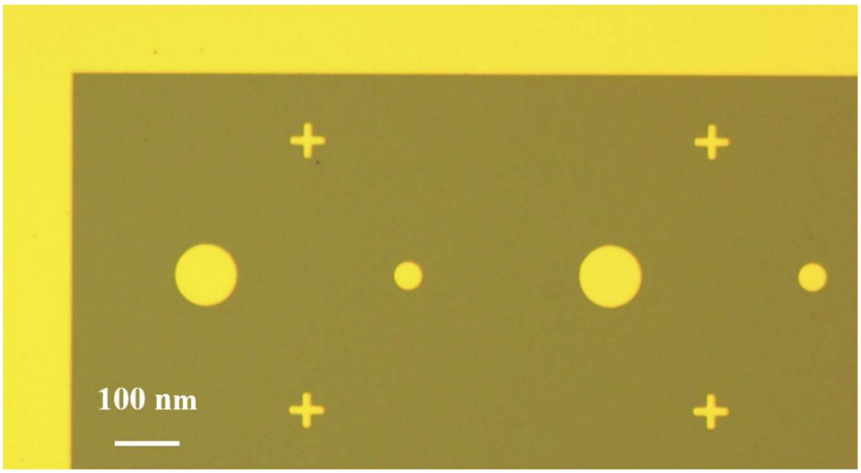

Figure 4.15: The optical microscopic image of the alignment sample. The radius of the small circular pattern is 20 μm, and the radius of the large circular pattern is 45 μm.

As mention earlier, the input beams are Gaussian beams and the intensity follow the distribution of $I_i(r) = I_{0i}e^{-\frac{2r^2}{w_{0i}^2}}$, i=1, 2 for QCL and CO_2 laser, respectively. The reflected power from the small circular pattern is maximized for each input laser by adjusting the

laser position. This step is repeated six times on a series of small patterns to reduce measurement error. Then the centers of the two beams are nearly located at the same position.

Nonlinear Optical Characterization Results

The DFG measurements of the metasurface were performed using the setup shown in Figure 4.16. In some experiments, a half-wave plate and/or a polarizer were used either for power control of the CO_2 laser or for the characterization of the polarization of the DFG output. For nonlinear measurement, the DFG power versus pump intensity, wavenumber, and output polarization were characterized. As mentioned earlier, the metasurface with the antenna long arm length of 1800 nm, the short arm length of 600 nm, and the short arm width of 250 nm produces three resonances that are best-matched the theoretical simulations and its performance is described below.

The QCL was operated at 250 kHz repetition rate with the duty cycle in the range 1-10%. The tuning range of the QCL was 5.1-5.7 μm (1750-1950 cm^{-1}). The wavelength of the CO_2 was 9.3 μm (1075 cm^{-1}). The wavenumber of a CO_2 laser was fixed at 1075 cm-1 ($\lambda 2 \approx 9.3$ μm). Figure 4.16 (a) shows the DFG emitted power as a function of the wavenumber of the QCL beam. The QCL laser was operated at 250 kHz repetition rate with a 10 % duty cycle. The QCL peak power was maintained at 15 mW at the sample position while the CO_2 laser provided a 1 W CW output power at the sample position. This dependence confirms that the metasurface provides the maximum DFG conversion efficiency at approximately λ_{DFG}=13 μm. Black dots in Figure 4.16 (a) show the dependence of the DFG power calculated from the theoretical dependence of the nonlinear susceptibility in Fig. 4.4 using equation (4.9). The measured frequency dependence of the DFG efficiency is in good agreement with theory.

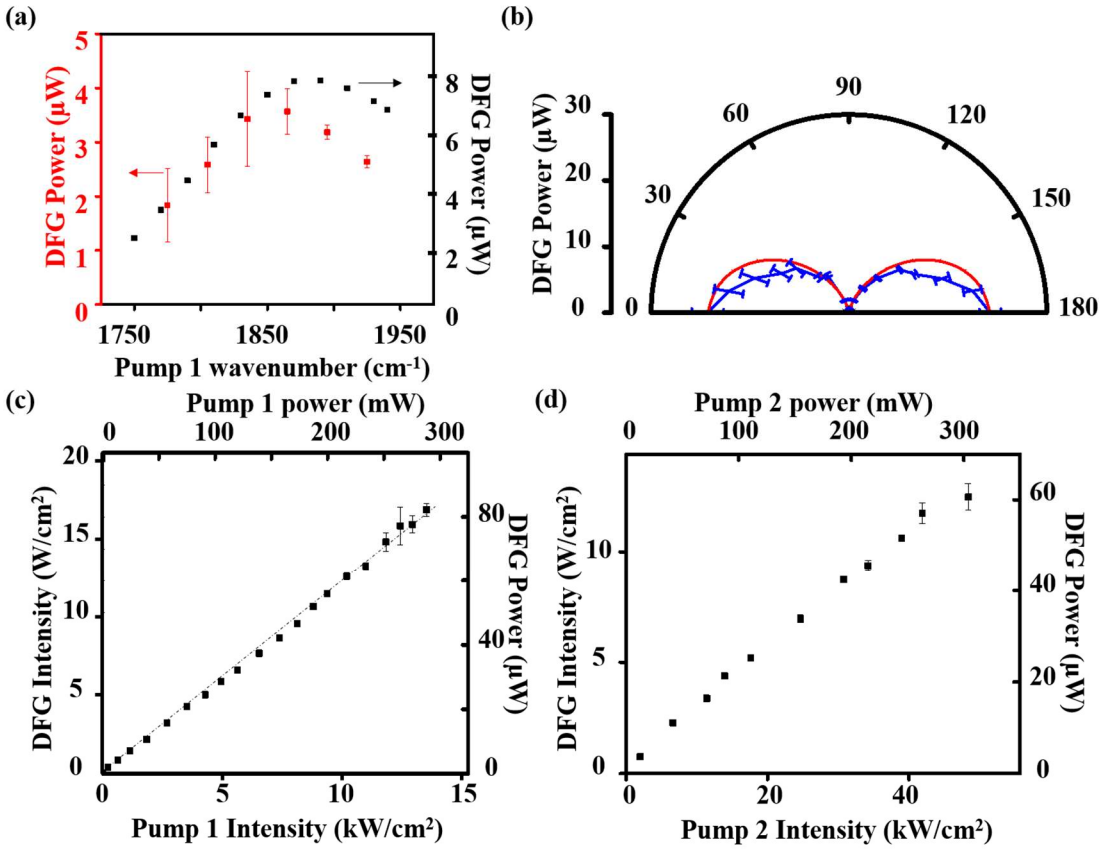

Figure 4.16: (a) Experimentally-measured DFG peak power as a function of the pump 1 wavenumber (red squares with error bars and left axis). Simulation results are plotted as black dots and refer to the right axis. The pump 1 power is fixed at 15 mW at the sample position. The wavelength of pump 2 is fixed at λ_2=9.3 μm and the pump 2 power is fixed at 1 W at the sample position. (b) DFG peak power as a function of the angle of polarization analyzer in front of the photodetector with 0° and 180° corresponding to x-direction in Fig. 3(a) or Fig. 2(b). The red line is a fit with $\cos^2(\theta)$, where θ is the analyzer angle. (c) DFG peak intensity as a function of the pump 1 peak intensity at the sample position. (d) DFG peak intensity as a function of the pump 2 peak intensity at the sample position. The data are corrected for the collection efficiency of the setup.

For the other three measurements reported in Fig. 4.16 (b)-(d), the QCL was fixed at 1850 cm^{-1} (5.4 μm). Fig. 4.16 (b), shows the polarization dependence of the DFG output. The data is well-fitted with a $\cos^2(\theta)$ function, indicating that the DFG output is predominantly x-polarized as expected by our theoretical analysis.

The DFG peak intensity as a function of the pump 1 (QCL) intensity is reported in Fig. 4.16 (c). The CO_2 laser power was fixed at 1W and the QCL power was varied from 0 to nearly 300 mW. In the measurement range, the DFG power has a linear dependence on pump 1 power and the maximum DFG power of 83 μW was obtained with the QCL beam power of 288 mW and the CO_2 power of 1W (see Fig. 4.16 (c)). The DFG peak power as a function of the pump 2 power is shown in Fig. 4.16 (d). In this case, the QCL was operated at 250 kHz repetition rate with 1% duty cycle with a fixed peak output power of 300 mW and the CO_2 laser power was varied between zero and 0.3 W using a half-wave plate and a polarizer. The DFG power displays a nearly linear dependence on the pump 2 power in this range. While the top axes in Fig. 4.16 (c,d) are plotted in power units, the bottom axis show peak intensities, that are obtained assuming Gaussian beams as discussed before. The experimental results for intensities match very well with the simulation results in Fig. 4.9. From Fig. 4.16(c), the DFG conversion efficiency with respect to pump 1 intensity ($\frac{I_{0DF}}{I_{01}}$) is approximately 0.13%, which corresponds to 0.3% conversion of pump 1 photons to DFG photons in the focal spot. The intensity data in Fig. 4.16 (c) also allows us to compute the effective nonlinear susceptibility of the metasurface using equation (2.19). We obtain $\chi_{eff}^{(2)} \approx 3.4\times10^5$ pm/V, close to theoretical predictions.

Experimentally-measured DFG peak power with other designs are also explored. Table 4.2 list the dimensions of the metasurface antennas that we tested, and the observed

maximum DFG power generated by the metasurfaces. The metasurface gap size was kept the same as that listed in Fig. 4.6.

	L_y=550 nm **W_x=200 nm**	**L_y=650 nm** **W_x=200 nm**	**L_y=600 nm** **W_x=200 nm**	**L_y=600 nm** **W_x=250 nm**	**L_y=600 nm** **W_x=150 nm**
L_x=2100 nm	<8 μW	<8 μW	<8 μW	<8 μW	<8 μW
L_x=2000 nm	18 μW	28 μW	13 μW	17 μW	15 μW
L_x=1900 nm	12 μW	50 μW	35 μW	40 μW	38 μW
L_x=1800 nm	40 μW	76 μW	78 μW	83 μW	X
L_x=1700 nm	23 μW	66 μW	71 μW	X	X

Table 4.2: The experimentally-measured DFG peak power with different dimensions. We indicate the structures which were damaged during fabrication and not tested with an "X". (cf. Fig. 4.7 for definitions of L_x, L_y, and w_x).

The maximum DFG power was observed from the metasurface with the antenna dimensions L_x=1800, L_y=600 nm, and W_x=250nm. As one can see, metasurfaces with small variations in the antenna dimensions from the optimal results presented here produced similar DFG power.

4.5 SUMMARY

Despite the need to optimize the nanoresonator design for three different resonant frequencies, the DFG metasurface has a comparable conversion efficiency to SHG metasurfaces reported earlier [*10*]. We believe that further improvements to the

conversion efficiency will be achieved with additional optimizations of both the MQW heterostructure and the nanoresonator designs.

In summary, we have demonstrated that our polaritonic nonlinear metasurfaces can produce giant DFG response. A nonlinear susceptibility of 3.4×10^5 pm/V and 0.3% conversion efficiency of 5.4 μm photons into 12.9 μm photons were measured experimentally. The results show that these ultrathin metasurfaces may prove to be versatile nonlinear elements for frequency down- and upconversion in a relatively broad spectral range, and without phase-matching constraints of traditional nonlinear crystals.

Chapter 5: Mid-IR Upconversion from Highly-Nonlinear Ultra-Thin Metasurfaces Coupled to Intersubband Transitions

5.1 INTRODUCTION

Upconversion has widespread applications such as surface analysis [*38-42*], quantum information processing [*43-46*], and generation of new light sources [*47-50*]. One of the most promising applications of upconversion is making infrared light visible to the human eye with 2D imaging technique based on nonlinear crystals [*51, 52*]. Although these techniques exhibit high conversion efficiency because of large crystal size, they have intrinsic limitations that arise from the quasi-phase-matching requirement. First, the conversion efficiency decreases dramatically as the phase mismatch term increases [*51*], which restricts the field-of-view. Second, even though the wide spectral band could benefit field-of-view broadening, images suffer from distortion and have various levels of brightness [*53*]. The limited field-of-view is the primary constraint for 2D upconversion imaging systems applications.

One possible solution is nonlinear intersubband polaritonic metasurfaces based on the coupling of quantum-engineered intersubband nonlinearities in semiconductor heterostructures. Unlike most other methods which require precise and complicated phase matching [*51-54*] to achieve efficient upconversion, the nonlinear intersubband plasmonic metasurface could work over a relatively broad wavelength [*10, 55*] without a restrictive phase-matching condition. Metasurface could potentially provide efficient continuous-wave upconversion in subwavelength films with large fields-of-view. While we are not presenting a setup for upconversion from infrared to visible, this work is an investigation toward efficient upconversion with nonlinear metasurface.

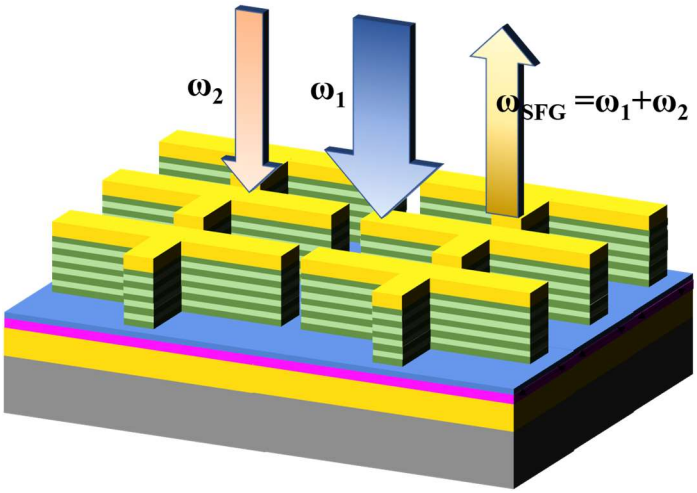

Figure 5.1: Schematic of the SFG process in the proposed metasurface.

We demonstrate the upconversion with nonlinear intersubband polaritonic metasurface for the first time. The structure was designed for pump wavelengths at $\lambda_1 \approx$ 9.3 μm and $\lambda_2 \approx$ 13.4 μm and output wavelength at $\lambda_{SFG} \approx$ 5.5 μm. In this experiment, an upconversion efficiency of 0.03% is demonstrated at a pump intensity of 30.4 kW/cm^2. The theoretical analysis predicts a 1% conversion efficiency with a pump intensity of ~450 kW/cm^2. These results indicate that nonlinear intersubband polaritonic metasurfaces offer a promising method for achieving high conversion efficiency through upconversion at sufficient pump intensity.

5.2 Metasurface Simulations

The metasurface discussed in Chapter 4 for DFG has great potential for efficient upconversion. The metasurface was made of a 390 nm thick multi-quantum well (MQW) with the conduction band diagram as shown in Figure 4.2, and the SEM images of the fabricated metasurface are displayed in Fig. 4.13. More details about the design and fabrication of the sample can be found in Chapter 4. Considering the characteristic

performance of this metasurface and working range of the laser sources we have, the ideal upconversion process is input wavelength at $\lambda_1 \approx 9.3$ μm, $\lambda_2 \approx 13.4$ μm (746.3 cm^{-1}) and output wavelength at $\lambda_{SFG} \approx 5.5$ μm (1818 cm^{-1}). Fig. 5.2 shows the enhancement of the z-polarized electric field in the MQW layer 200 nm below the top gold surface of the antenna compared to the amplitudes of the incident wave for the case of three frequencies involved in the SFG process.

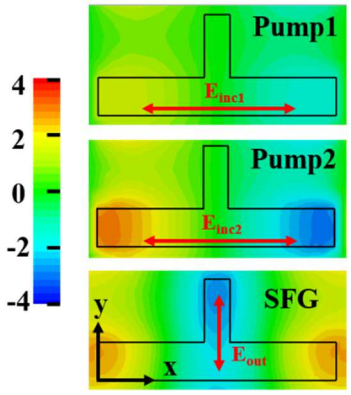

Figure 5.2: The simulated E_z field enhancement at the two pump frequencies and the sum-frequency monitored in the MQW layer 200 nm below the top metal surface of the nanoresonator. The color code shows the field enhancements in the MQW heterostructure relative to the electric-field amplitudes in the incoming waves.

The SFG nonlinear response can be calculated with:

$$\chi^{(2)}_{MQW,zzz}(\omega_1+\omega_2,\omega_1,\omega_2) = \frac{e^3(z_{12}z_{23}z_{31})}{2\varepsilon_0\hbar^2}\left\{\frac{N_1-N_2}{(\omega_{31}-\omega_1-\omega_2-i\gamma_{31})(\omega_{21}-\omega_1-i\gamma_{21})}\right. \quad (5.1)$$
$$+\frac{N_1-N_2}{(\omega_{31}-\omega_1-\omega_2-i\gamma_{31})(\omega_{21}-\omega_2-i\gamma_{21})}$$
$$+\frac{N_2-N_3}{(\omega_{13}+\omega_1+\omega_2+i\gamma_{13})(\omega_{32}-\omega_1-i\gamma_{32})}$$
$$\left.+\frac{N_2-N_3}{(\omega_{13}+\omega_1+\omega_2+i\gamma_{13})(\omega_{32}-\omega_2-i\gamma_{32})}\right\}$$

When the pump intensity increases, more and more electrons are pumped from the fundamental energy level to higher energy levels, which could cause saturation in the

output SFG power. The populations of different subbands can be calculated with the coupled-rate equations, as shown in equation (5.2). $I_z^{\omega_1}$, $I_z^{\omega_2}$ are two pump intensities from state 1 to state 2, and state 2 to state 3 respectively. $\alpha_{ij}(\omega_p)$ is the absorption coefficient between state *i* and *j* at frequency ω_p. N_1, N_2, N_3 are the populations of the first three energy subbands in the MQW structure, ez_{ij}, $\hbar\omega_{ij}$, $\hbar\gamma_{ij}$ are the transition dipole moment, transition energy, and the transition linewidth between states *i* and *j*. τ_{ij} is the relaxation time between state *i* and *j*. Here the input pump intensity from state 1 to state 3 is neglected.

$$\begin{cases} \dfrac{dN_1}{dt} = \dfrac{-\alpha_{12}(\omega_1)I_z^{\omega_1}}{\hbar\omega_1} + \dfrac{N_2}{\tau_{12}} + \dfrac{N_3}{\tau_{13}} \\ \dfrac{dN_2}{dt} = \dfrac{\alpha_{12}(\omega_1)I_z^{\omega_1}}{\hbar\omega_1} - \dfrac{\alpha_{23}(\omega_2)I_z^{\omega_2}}{\hbar\omega_2} - \dfrac{N_2}{\tau_{12}} + \dfrac{N_3}{\tau_{23}} \\ \dfrac{dN_3}{dt} = \dfrac{\alpha_{23}(\omega_2)I_z^{\omega_2}}{\hbar\omega_2} - \dfrac{N_3}{\tau_{13}} - \dfrac{N_3}{\tau_{23}} \end{cases} \tag{5.2}$$

The populations can be approximate with steady-state solutions. Since $\alpha_{ij}(\omega_p) = \frac{N_i - N_j}{N}\alpha_{ij}^{(0)}(\omega_p)$, we can get

$$\begin{cases} -\dfrac{(N_1 - N_2)\alpha_{12}^{(0)}I_z^{\omega_1}}{N\hbar\omega_1} + \dfrac{N_2}{\tau_{12}} + \dfrac{N_3}{\tau_{13}} = 0 \\ \dfrac{(N_1 - N_2)\alpha_{12}^{(0)}I_z^{\omega_1}}{N\hbar\omega_1} - \dfrac{(N_2 - N_3)\alpha_{23}^{(0)}I_z^{\omega_2}}{N\hbar\omega_2} - \dfrac{N_2}{\tau_{12}} + \dfrac{N_3}{\tau_{23}} = 0 \\ \dfrac{(N_2 - N_3)\alpha_{23}^{(0)}I_z^{\omega_2}}{N\hbar\omega_2} - \dfrac{N_3}{\tau_{13}} - \dfrac{N_3}{\tau_{23}} = 0 \end{cases} \tag{5.3}$$

Set

$$\begin{cases} I_{12}^{sat} = \dfrac{N\hbar\omega_1}{2\tau_{12}\alpha_{12}^{(0)}} \\ I_{23}^{sat} = \dfrac{N\hbar\omega_2}{2\tau_{23}\alpha_{23}^{(0)}} \end{cases} \tag{5.4}$$

Then the relationships between populations of different levels are

$$\begin{cases} N_1 = N_3\left(1+\dfrac{2I_{12}^{sat}}{I_z^{\omega_1}}\left(1+\dfrac{\tau_{12}}{\tau_{13}}\right)+\dfrac{2I_{23}^{sat}}{I_z^{\omega_2}}\left(1+\dfrac{\tau_{23}}{\tau_{13}}\right)+\dfrac{4I_{12}^{sat}I_{23}^{sat}}{I_z^{\omega_2}I_z^{\omega_1}}\left(1+\dfrac{\tau_{23}}{\tau_{13}}\right)\right) \\ N_2 = N_3\left(1+\dfrac{2I_{23}^{sat}}{I_z^{\omega_2}}\left(1+\dfrac{\tau_{23}}{\tau_{13}}\right)\right) \\ N_1+N_2+N_3 = N \end{cases} \quad (5.5)$$

The pump intensity of every position is calculated from CST simulation in order to calculate the population N_1, N_2 and N_3 of every position and the local susceptibility. Similar to the derivation of equation (2.19), the effective overall SFG susceptibility can be calculated by integrated SFG susceptibility of all positions, as shown below.

$$\chi_{eff}^{(2)}(\omega_1+\omega_2,\omega_1,\omega_2) = \frac{\int_V \chi_{MQW,zzz}^{(2)}(r)\dfrac{E_z^{\omega_1}(r)}{E_{inc}^{\omega_1}}\dfrac{E_z^{\omega_2}(r)}{E_{inc}^{\omega_2}}\dfrac{E_z^{\omega_{SFG}}(r)}{E_{inc}^{\omega_{SFG}}}dV}{V} \quad (5.6)$$

where the $E_z^{\omega_i}(r)$ is the z component of the electric field inside the MQW at frequency ω_i. The output SFG power is

$$I_{SFG} = \frac{(\omega_{SFG}\chi_{eff}^{(2)}d)^2 I_{inc}^{\omega_1} I_{inc}^{\omega_2}}{2\varepsilon_0 c^3} \quad (5.7)$$

where d is the thickness of MQW, $I_{inc}^{\omega_i}$ is the pump intensity in air at frequency ω_i, I_{SFG} is the output SFG beam intensity.

In order to produce the maximum conversion efficiency with this metasurface, various pump intensities are explored in the simulation. In Fig. 5.3(a), the conversion efficiency (I_{SFG}/I_{QCL}) has a saturation effect when the CO_2 laser (pump 1) intensity increases above 50 kW/cm^2. Before the saturation, for the same CO_2 laser intensity, the conversion efficiency increases as QCL (pump 2) intensity increases. In our experiment, since the maximum QCL peak power is around 50-100 mW (3.5 kW/cm^2-7.1 kW/cm^2),

the maximum conversion efficiency is below 0.1% for CO_2 laser intensity below 500 kW/cm^2. In Fig. 5.3(b), the conversion efficiency (I_{SFG}/I_{CO}) and the QCL intensity demonstrate a linear dependence for CO_2 laser intensity below 5.1×10^2 kW/cm^2 without showing a saturation limit. For the same QCL intensity, the upconversion process is more efficient when CO_2 laser intensity is small, such as 5.1×10^{-2} kW/cm^2 and 5.1 kW/cm^2. For the CO_2 laser intensity of 5.1×10^{-2} kW/cm^2 and 5.1 kW/cm^2, the conversion efficiency is very similar, and 5.1 kW/cm^{2}could generate a more considerable output power. Thus, in the experiment, the CO_2 laser intensity is fixed around 5.1 kW/cm^2 when tuning the QCL intensity.

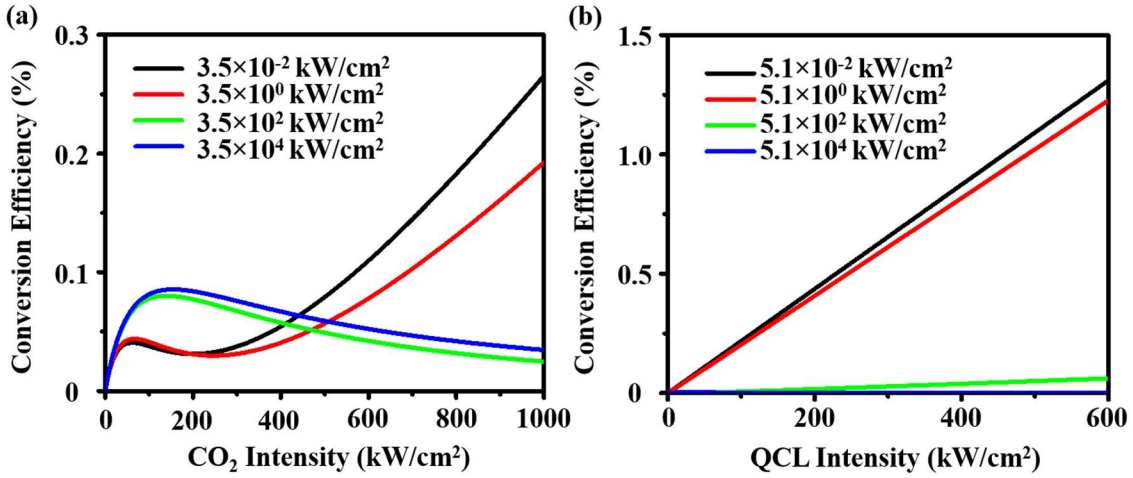

Figure 5.3: (a) Simulations of the SFG conversion efficiency versus CO_2 laser (pump 1) intensity with CO_2 laser polarized in the x-direction at $\lambda_1 \approx 9.3$ μm. QCL (Pump 2, $\lambda_2 \approx 13.4$ μm) is polarized in the x-direction and its intensity is shown in the figure. (b) Simulations of the SFG conversion efficiency versus QCL intensity with QCL polarized in the x-direction at $\lambda_2 \approx 13.4$ μm. CO_2 laser ($\lambda_1 \approx 9.3$ μm) is polarized in the x-direction and its intensity is shown in the figure.

The corresponding effective susceptibilities are shown in Fig. 5.4. In Fig. 5.4 (a), for QCL intensities above 3.5×10^{-2} kW/cm^2, the $\chi_{eff}^{(2)}$ decreases when CO_2 laser

intensity increases. This diminution of $\chi_{eff}^{(2)}$ contributes to the saturation of conversion efficiency. For QCL intensities below 3.5 kW/cm^2, the $\chi_{eff}^{(2)}$ decreases and then increases when CO_2 laser intensity increases. This increase of $\chi_{eff}^{(2)}$ contributes to the reascension of the conversion efficiency curve in Fig. 5.3 (a).

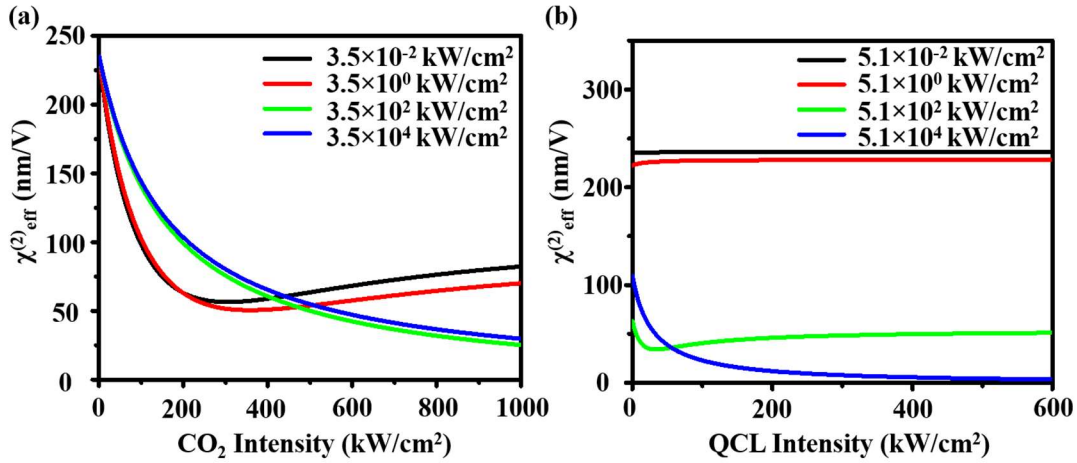

Figure 5.4: (a) Simulations of the effective susceptibility versus CO_2 laser intensity with CO_2 laser polarized in the x-direction at $\lambda_1 \approx 9.3$ μm. QCL ($\lambda_2 \approx 13.4$ μm) is polarized in the x-direction and its intensity is shown in the figure. (b) Simulations of the effective susceptibility versus QCL intensity with QCL polarized in the x-direction at $\lambda_2 \approx 13.4$ μm. CO_2 laser ($\lambda_1 \approx 9.3$ μm) is polarized in the x-direction and its intensity is shown in the figure.

In Fig. 5.4 (b), for CO_2 laser intensity below 5.1 kW/cm^2, $\chi_{eff}^{(2)}$ increases by a tiny amount when QCL intensity increases and it gradually approaches a steady value. This leads to an almost linear trend in the conversion efficiency as shown in Fig. 5.3(b). For CO_2 laser intensity at 5.1×10^2 kW/cm^2, the $\chi_{eff}^{(2)}$ drops at the beginning and then increases. For CO_2 laser intensity at 5.1×10^4 kW/cm^2, the $\chi_{eff}^{(2)}$ decreases in the entire simulation range. For future research, a strong pump intensity for transitions from state 2 to 3 and a relatively low intensity for transitions from state 2 to 3 are preferred to achieve a significant increase in conversion efficiency.

5.3 EXPERIMENTAL CHARACTERIZATION

Linear Absorption Spectra

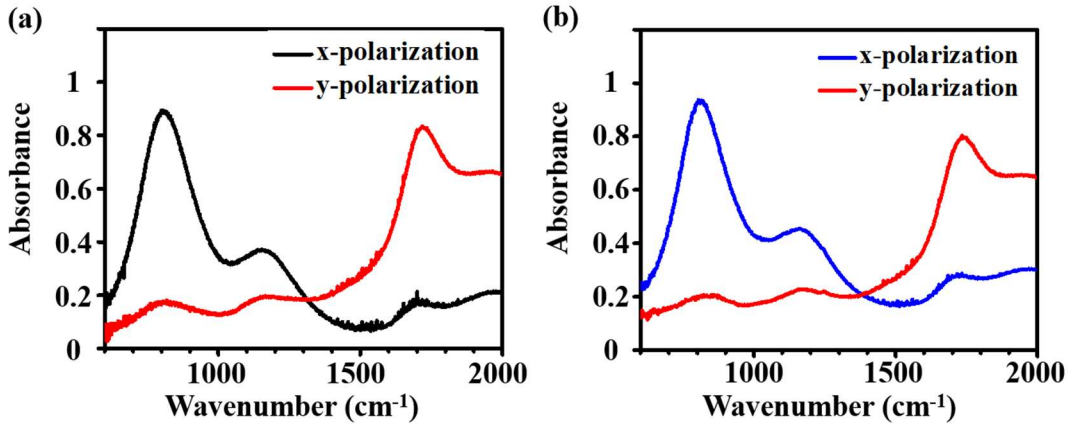

Figure 5.5: (a) Reflection-absorption spectrum of the fabricated metasurface at normal incidence for light polarized along x-axis and y-axis after the damage test. (b) Reflection-absorption spectrum of the fabricated metasurface at normal incidence for light polarized along x-axis and y-axis before the damage test.

The absorption spectra of this metasurface for x- and y-polarized input light were measured with Bruker FTIR spectrometer. The spectra are the same before and after the damage test. This step is to confirm that the metasurface is not damaged by the continuous-wave CO2 laser with a beam intensity of 50 kW/cm^2.

Homemade QCL Laser Properties

A homemade QCL was used as one of the pump sources. The wavelength of this non-tunable single-frequency QCL is measured to be 13.4 μm. An aspheric AR coated lens with a focal length of 1.87 mm and a numerical aperture of 0.85 (LightPath Technologies) is used as the collimating lens in front of the laser. A pulse generator (Agilent 8114A, 100V/2A) and a high power supply (KEPCO high voltage power supply, 0-1000 V) are used to generate a high voltage pulse to trigger the laser.

The output powers after the collimating lens were measured. For this measurement, the laser was operating with a frequency of 50 kHz and a pulse width of 50 ns, and the total bias voltage is tuned from 400 to 500 V with a step of 10 V. The measured current reading on KEPCO and the average output power are shown in Fig. 5.6. (The laser chip is in series connecting with a 50 Ω resister.) In the measurement range, the laser is not saturated.

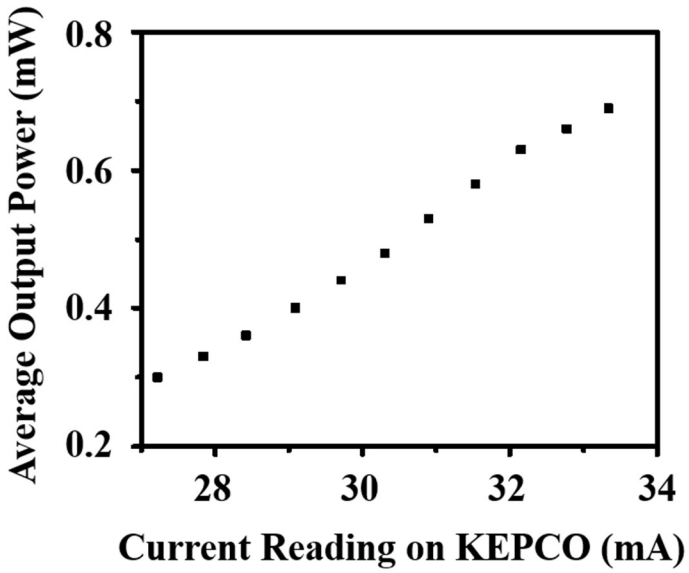

Figure 5.6: The laser average output power versus current reading on KEPCO with 0.25% duty cycle (frequency 50 kHz, pulse width 50 ns).

QCL Cooling Stage Design and Characterization

Since the homemade QCL requires a stable temperature around 20 °C during the nonlinear characterization to prevent laser degradation and power shifting, a new cooling stage was made for this homemade QCL. A 50 mm×50 mm×3.75 mm thermoelectric cooler (TEC) (Peltier Module CP15535) was sandwiched between two copper plates (4 in.×4 in.×0.5 in.), and the heat was extracted from the top plate to bottom plate. A

thermal sensor (thermistor *#B57550G0103F000*, 10k Ω at 25 °C) was embedded into the top copper plate with a distance of 0.06" below the top surface. A computer fan was added to the bottom copper plate to accelerate the heat dissipation. Silicon cooler paste was used as an adhesion layer between different parts to improve the heat dissipation.

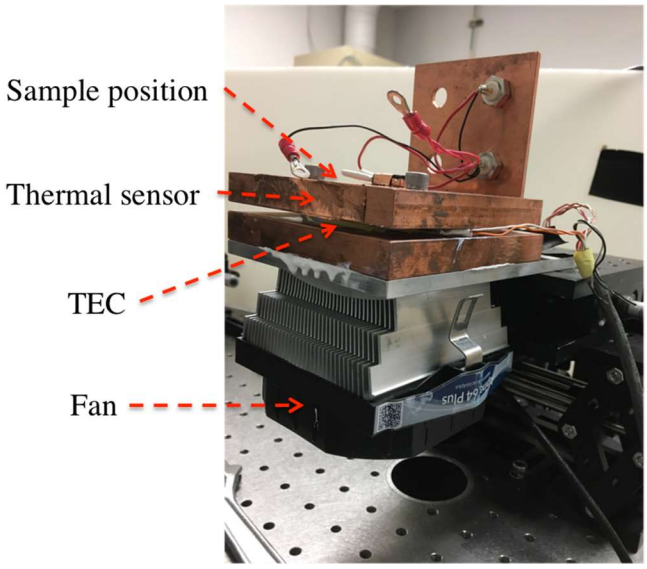

Figure 5.7: The structure of the initial designed cooling stage.

The thermal sensor and the TEC are connected to the temperature controller (ILX Lightwave LDT 5500B) by a interconnect cable (CC501 S). The Steinhart-Hart equation is the most popular model for describing the thermistor R-T relationship:

$$\frac{1}{T} = C_1 + C_2 lnR + C_2 (lnR)^3 \tag{5.8}$$

where T is the absolute temperature in Kelvin and R is the thermistor resistance in ohms. The C_1, C_2, and C_3 are called Steinhart-Hart constants. The thermistor calibration was performed to extract the C_1, C_2, and C_3 by measuring the resistances at three different temperatures. Please note, the temperature T shown on the screen of our controller and the thermal sensor resistance R has a relationship of

$$\frac{1}{T} = C_1^* \times 10^{-3} + C_2^* \times 10^{-4} lnR + C_3^* \times 10^{-7} (lnR)^3 \quad (5.9)$$

where C_1^*, $C_2^*$and C_3^* are the coefficients we set in the controller. Here we get C_1^*= 0.756, C_2^*= 2.615, C_3^*= 2.415.

With the original air cooling design, I noticed that the temperature of resister ramped up fast and started to melt during the experiment. I also noticed that the dissipated heat from the 50 Ω resister induced a vast thermal noise when testing the laser output power. Thus the resister was moved away from the laser chip and a water cooling block was added to cool down the resister. The modified stage with water cooling block is shown below.

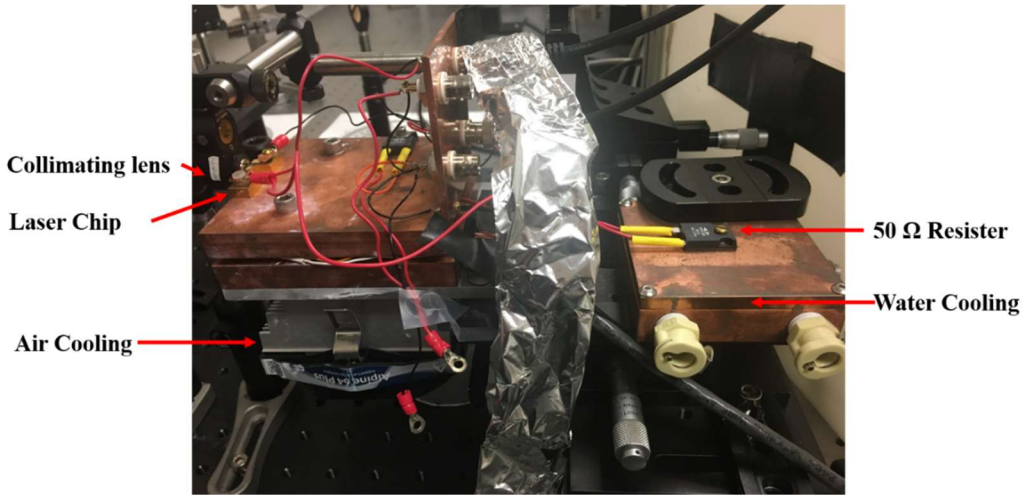

Figure 5.8: The structure of the modified cooling stage for homemade QCL.

Experimental Setup

The experimental setup for SFG metasurface characterization was designed as Fig. 5.9(a). A linear polarized homemade QCL (13.4 μm) and a non-tunable CO2 laser (9.3 μm) were placed with the same polarization. A SP filter (SP1) was used as a beam splitter to combine the two beams. The beams were reflected by another SP filter (SP2) and passed through a numerical aperture 0.5 collimating lens to the sample. The SFG

output was collected by the same lens, and then passed through a SP filter and a ZnSe lens to the detector.

The actual experimental setup is shown in Fig. 5.9(b). A BaF_2 wedge (with 0.5-degree difference of the two surfaces) was used to attenuate the power of the CO_2 laser to 1~1.2W. The BaF_2 (n=1.47 at 9.3 μm, reflection ~8%) wedge was placed at 45° to the incoming CO_2 beam. After 1 m distance, the separation of reflected two reflected beams was around 9 mm. One of the beams was blocked and the other one was used as the pump source. Here a wedge was used instead of a window because we observed dramatically fluctuations of the CO_2 power with a window. (It might be caused by the interference of the two beams and the slight shifting of the wavelength.) The metasurface sample was mounted on a copper heat sink to improve the heat dissipation. A LP filter was placed in front of QCL protect the QCL from strong CO_2 beams, and a SP filter was placed in front of the detector to reduce background noise and increase the signal-to-noise ratio. The two LP filters are long-pass dichroic filters that transmit $\lambda_2 \approx 13.4$ μm and reflects $\lambda_1 \approx 9.3$ μm. The two SP filters are short-pass dichroic filters that reflect λ_1 and λ_2 and transmits $\lambda_{SFG} \approx 5.5$ μm.

In this setup, the radii of pump 1 (CO2 laser) and pump 2 (homemade QCL) at the focal point are measured to be 25 μm and 30 μm respectively. The radius of the SFG signal is calculated to be 19.2 μm with Gaussian beams assumption.

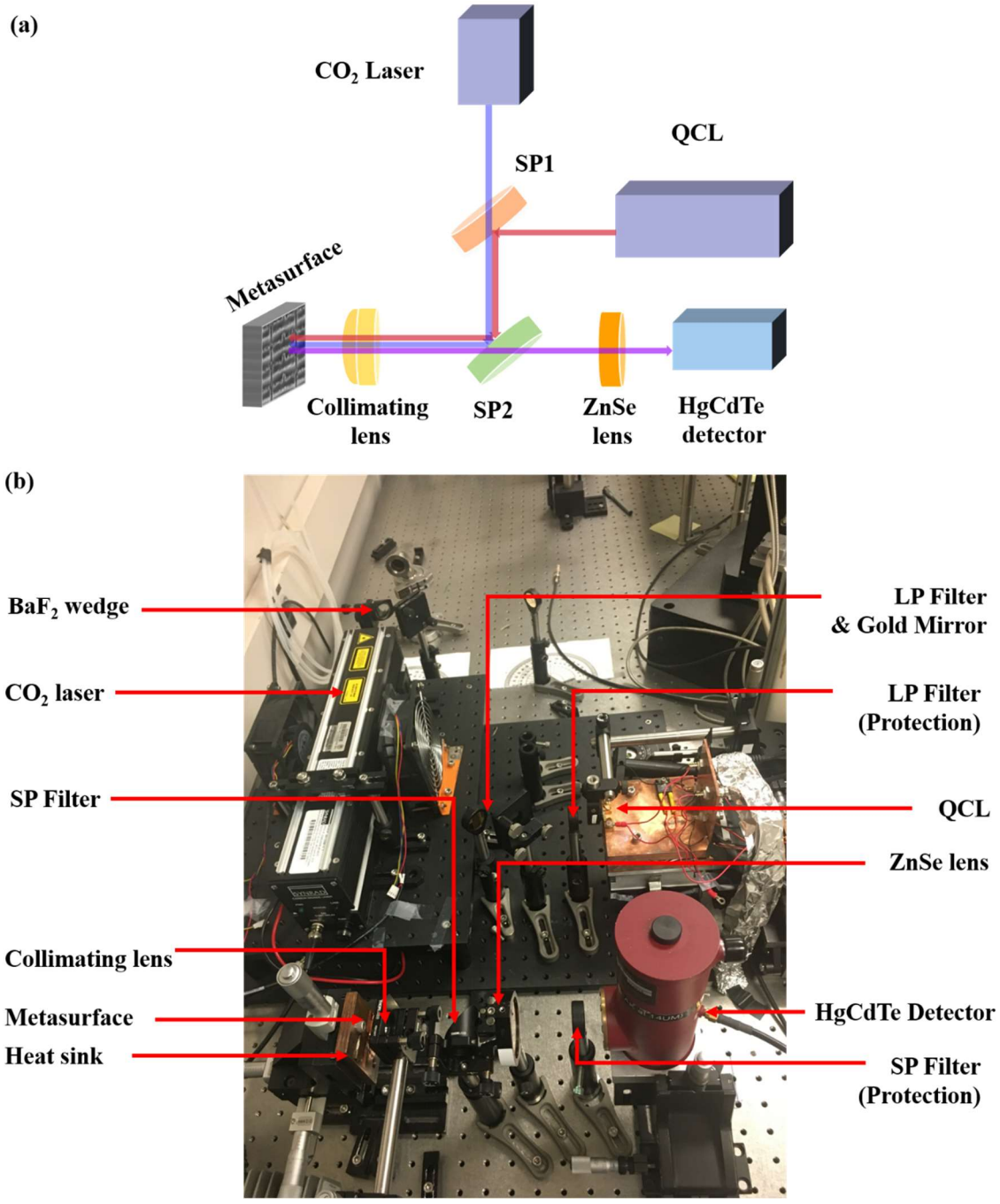

Figure 5.9: Optical setup for metasurface SFG characterization. (a) Schematic of the designed optical setup. (b) Photo image of the actual optical setup.

Detector Calibration

The lock-in amplifier reading with the HgCdTe detector at 5.5 μm was calibrated with different duty cycles. The laser (MIRcat-QT Mid-IR Laser) beam was focused by a ZnSe lens and the power of the beam was measured by a power meter. Then the power meter was replaced with a HgCdTe detector, and an ND filter was added in front of the detector to avoid the saturation. The calibration coefficients are shown in Fig. 5.10. The calibration coefficient of the HgCdTe detector at 5.5 μm with 0.25% duty cycle (frequency 50 kHz, pulse width 50 ns) is 1400 V/W.

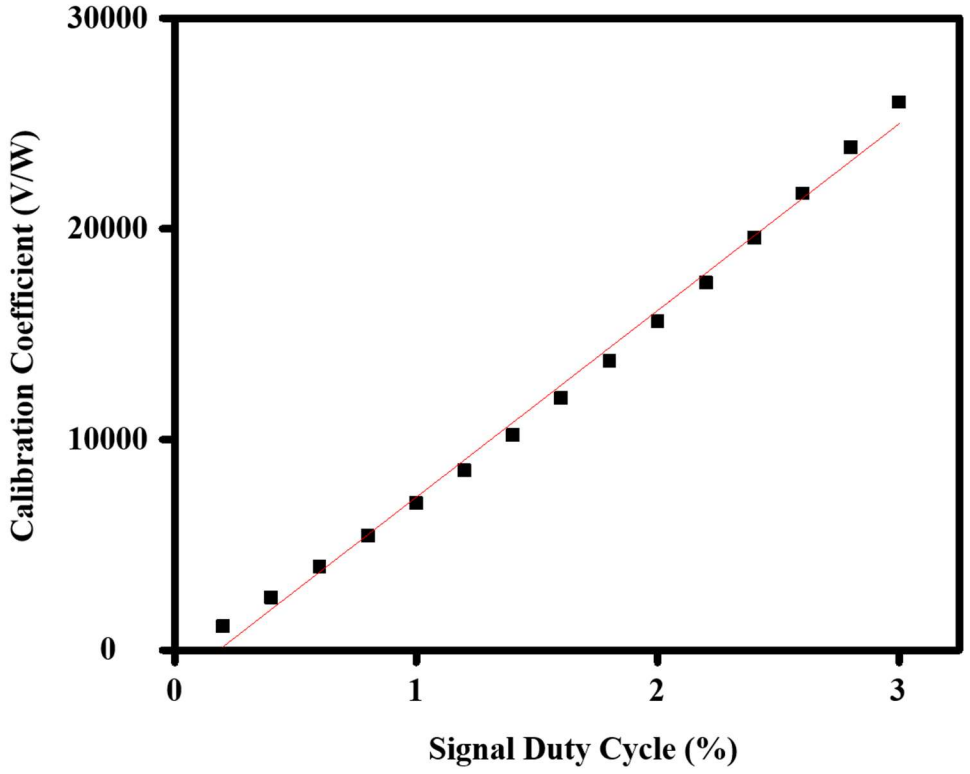

Figure 5.10: The calibration coefficients of the HgCdTe detector at 5.5 μm with different signal duty cycles.

Nonlinear Measurement Results

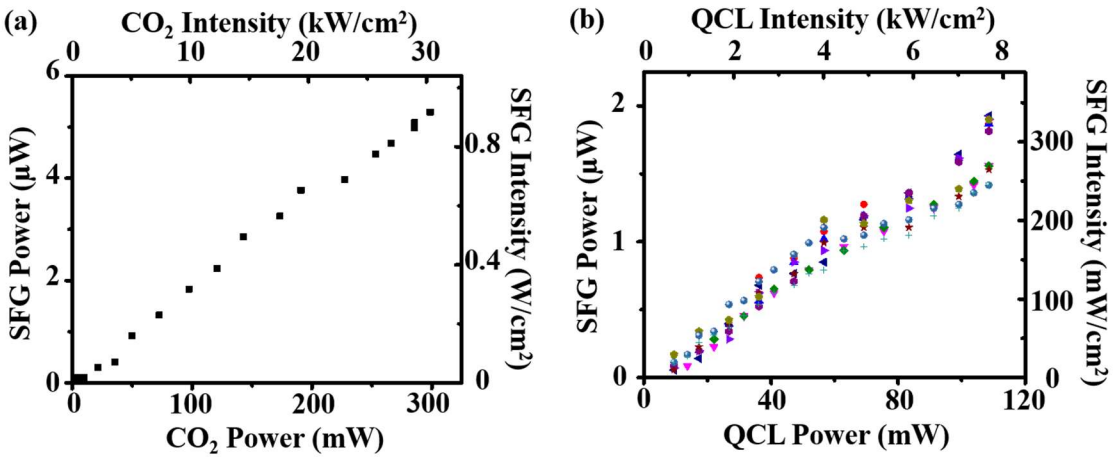

Figure 5.11: a) Experimentally measured SFG peak power/intensity as a function of the CO_2 laser peak power/intensity. The QCL power is fixed at 47 mW (3.3 kW/cm^2) at the sample position. b) Experimentally measured SFG peak power/intensity as a function of the QCL peak power/intensity. The CO_2 laser power is fixed at 50 mW (5.1 kW/cm^2) at the sample position. The data are corrected for the collection efficiency of the setup.

The homemade QCL laser is operating at 50 kHz, 50 ns (0.25% duty cycle) with a homemade water-cooling system. The wavelength is 13.4 μm. The CO_2 laser is operating under a continuous-wave mode with a wavelength of 9.3 μm. Experimental results have been shown in Fig. 5.11. Fig. 5.11(a) shows the SFG power/peak intensity as a function of the CO2 laser power/peak intensity. Here, QCL power was fixed at 47 mW and CO2 laser power was varied between zero and 0.3 W using a half-wave plate and a polarizer. It shows a clear linear dependence with a maximum conversion efficiency (I_{SFG}/I_{QCL}) of 0.03%. The maximum SFG power was 5.3 μW when the CO_2 laser was 300 mW. The relationship between SFG power/peak intensity and homemade QCL power/peak intensity is shown in Fig. 5.11(b), where CO_2 power was fixed at 50 mW and QCL power

was tuned from 0 to 110 mW. The measurement has been repeated several times and shown with different colors in the figure. The SFG power and QCL power has a nearly linear dependence. The intensity data in Fig. 5.11(a) also allow us to compute the effective nonlinear susceptibility of the metasurface using Equation (5.6). We obtain $\chi^{(2)}_{eff} \approx 158$ nm/V. Our experiment conversion efficiency is a little smaller than the theory prediction (0.04%) for this pump intensity. The polarization dependence of the SFG output is shown in Fig. 5.12. The y-polarized SFG signal dominated in the output signal.

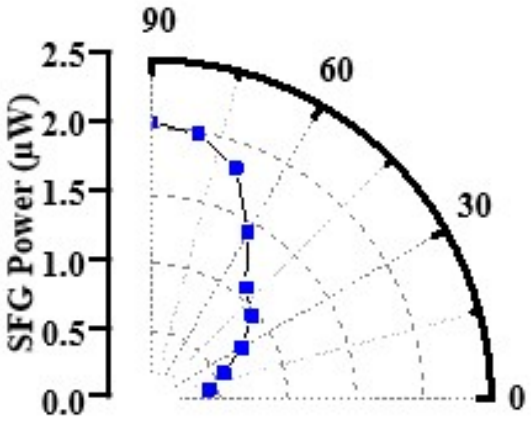

Figure 5.12: DFG peak power as a function of the angle of polarization analyzer in front of the photodetector with 0° corresponding to x-direction in Fig. 5.2.

5.4 SUMMARY

An upconversion efficiency of 0.03% has been demonstrated in the metasurface with input intensity of 30.4 kW/cm^2 and 3.3 kW/cm^2. Stronger pump lasers are required to achieve higher conversion efficiency. However, due to the saturation effect, by increasing the pump intensity for transitions from state 1 to state 2 will not lead to a conversion efficiency more than 0.1% for intensity below 500 kW/cm^2 (with the other

pump intensity below 3.5×10^4 kW/cm^2). The theory analysis has predicted a remarkable conversion efficiency more than 1% with input intensity of 500 kW/cm^2 for the transitions from state 2 to state 3 (with the other pump intensity at 5.1 kW/cm^2). This study might light up the path for further research to achieve high conversion efficiency for upconversion metasurfaces and has excellent potential for 2D upconversion imaging. For pump intensity around or above 10^4 kW/cm^2, the strong intensity could cause other effects such as Rabi splitting, which may lead to even higher conversion efficiency by carefully design specific MQW structures.

Chapter 6: Prospect of Upconversion in Polaritonic Intersubband Nonlinear Metasurfaces

6.1 Introduction

The upconversion in polaritonic intersubband nonlinear metasurfaces has been demonstrated in Chapter 5 with pump intensity up to 30 kW/cm^2. From the previous theoretical analysis in Chapter 5, we notice that a strong pump intensity for state 2 to 3 transition will contribute to a high-efficiency upconversion. Here I provide a preliminary theoretical analysis of the metasurface behaviors under extremely high pump intensities.

6.2 Preliminary Theoretical Analysis

Here we consider a special case: the pump 2 (I_2, for state 2 to 3 transition) is extremely strong and pump 1 (I_1, for state 1 to 2 transition) is weak. In this situation, whenever an electron is pumped from state 1 to state 2, it is almost immediately pumped to state 3. Even though the I_2 is extremely large, it is hard to reach saturation intensity $I_{23}^{sat}(\omega_{32})$ (see equation (5.4)) because of the limited electrons on state 2 pumped by I_1. While we do need to pay attention to the saturation $I_{12}^{sat}(\omega_{32})$, which is the saturation intensity for state 1 to 2 transition pumped by I_2. Usually, the photon energy of pump 2 is close to the transition energy $E_{23} = \hbar\omega_{23}$, but away from the transition energy $E_{21} = \hbar\omega_{21}$, and the $I_{12}^{sat}(\omega_{23})$ is a large value. For sufficiently large field strength, $I_{12}^{sat}(\omega_{23})$ becomes a limiting factor for conversion efficiency.

$$I_{12}^{sat}(\omega_{23}) = \frac{cn\varepsilon_0((E_2 - E_{21})^2 + \hbar^2\gamma_{12}^2)}{2\mu_{12}^2\tau_{12}\gamma_{12}} \tag{6.1}$$

where E_2 is the electric field of pump 2, τ_{12} is the relaxation time between state 1 and 2, $\hbar\gamma_{12}$ is the measured transition linewidth between states 1 and 2.

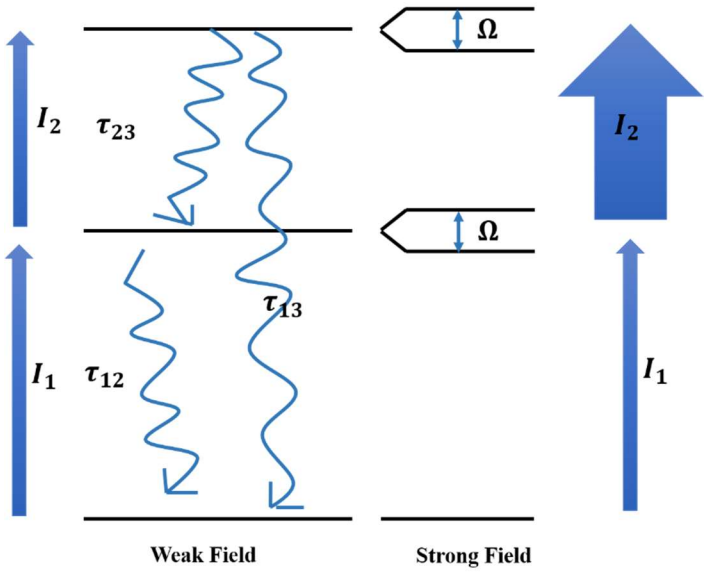

Figure 6.1: Schematic of a three-level system with weak pump intensity (I_2) on the left-hand side and strong pump intensity (I_2) on the right-hand side. Ω is the Rabi frequency. τ_{ij} is the relaxation time between state *i* and *j*.

On the other hand, a sufficiently intense optical field can profoundly modify the energy-level structure and cause Rabi splitting. The Rabi frequency is [*11*]:

$$\Omega = \frac{2|\mu_{32}||E|}{\hbar} \tag{6.2}$$

For the relaxation process of a two-level system, we have:[14]

$$\frac{1}{T_2} = \frac{1}{2T_1} + \gamma_c \tag{6.3}$$

where γ_c is the collisional dephasing rate, T_2 is the dipole dephasing time, T_1 is the population relaxation time. In our MQW system, the second and third energy levels can be treated as a two-level system with a strong pump field. $\frac{1}{T_1} = \frac{1}{\tau_{23}} + \frac{1}{\tau_{13}}$, τ_{13} and τ_{23} are calculated by the self-consistent Poisson–Schrödinger solver, based on the Frohlich model of electron phonon coupling. T_1 is on the order of picosecond. $\frac{1}{\gamma_c}$ is usually around 30-50 fs. Thus T_2 is dominated by γ_c. $\frac{1}{T_2} \approx \gamma_{23}$, corresponds to the measured linewidth.

We want to design a structure that can survive under high-intensity beams without obvious distortion of the original energy levels, which requires Rabi frequency $\Omega \leq \gamma_{23}$.

$$\frac{2|\mu_{32}||E|}{\hbar} \leq \gamma_{23} \tag{6.4}$$

$$|E| \leq \frac{\hbar\gamma_{23}}{2|\mu_{32}|} \tag{6.5}$$

Since $I = 2\varepsilon_0 nc|E|^2$ (n is the MQW refractive index),

$$I \leq \frac{\varepsilon_0 nc\hbar^2\gamma_{23}^2}{2|\mu_{32}|^2} \tag{6.6}$$

The threshold intensity is named as I_{Ra} in the following discussion, and the value is $I_{Rabi} = \frac{\varepsilon_0 nc\hbar^2\gamma_{23}^2}{2|\mu_{32}|^2}$.

The highest pump intensity is limited by the smaller value of I_{Rabi} and $I_{12}^{sat}(\omega_{32})$. Ideally, we want to have structures with $I_{Rabi} < I_{12}^{sat}(\omega_{32})$, so that the limiting factor is I_{Rabi}. These structures require a larger difference of the transition energies $|E_{21} - E_{32}|$ compared with our previous design. However, limited by the laser sources we have, I provide a compromised design with I_{Rabi} close to $I_{12}^{sat}(\omega_{32})$.

6.3 MQW DESIGN

The structure was designed to be resonant for the upconversion process with pump photon energies of 92 meV and 133 meV, respectively. The CO_2 laser (9.3 μm, 133 meV) will provide a strong pump for state 2 to 3 transition. The QCL (13.4 μm, 92.5 meV) will provide the weak pump for state 1 to 2 transition. The layer sequence (in nanometer) is **3**/6.9/**0.9**/3.6/**3** where AlInAs barriers are shown in bold, and the first 2 nm of the first 3-nm-barrier and the last 2 nm of the last 3-nm-barrier are n-doped to 3×10^{18} cm^{-3}. The conduction band diagram of one MQW period is shown in Figure 6.2. ez_{ij} is

the transition dipole moment between state i and j. E_{ij} is the transition energy between state i and j.

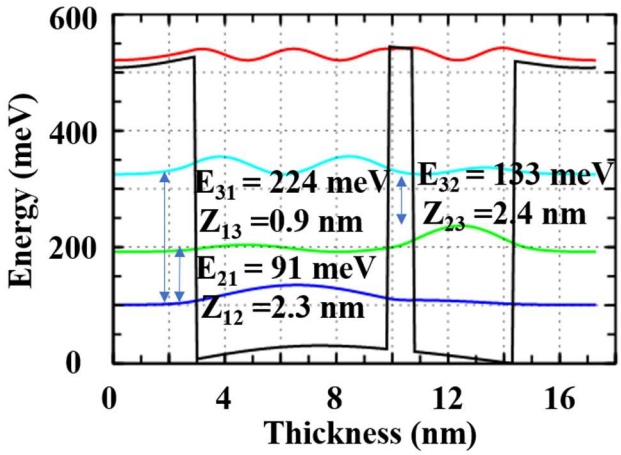

Figure 6.2：Conduction band diagram of one period of an $In_{0.53}Ga_{0.47}As/Al_{0.48}In_{0.52}As$ MQW structure designed for high-efficiency upconversion. The layer sequence (in nanometer) is **3**/6.9/**0.9**/3.6/**3** where AlInAs barriers are shown in bold, and the first 2 nm of the first 3-nm-barrier and the last 2 nm of the last 3-nm-barrier are n-doped to 3×10^{18} cm^{-3}

For this structure, τ_{23}=1.99 ps, τ_{13}= 1.77 ps, τ_{13}= 0.99 ps, calculated by the self-consistent Poisson‐Schrödinger solver, based on the Frohlich model of electron phonon coupling. The calculated I_{Rabi} is 1.7×10^{11} W/m^2, the calculated $I_{12}^{sat}(\omega_{32})$ is 7.4×10^{10} W/m^2. The calculated maximum conversion efficiency (before saturation) is 2.08%. Please note, the calculated intensity I_{Rabi} and $I_{12}^{sat}(\omega_{32})$ are the intensity inside the MQW. If the intensity in air is the interested value, then it can be converted as below:

$$I_{Rabi,air} = \frac{I_{Rabi}}{n|\eta|^2} \tag{6.7}$$

η is the field enhancement factor, n is the refractive index of MQW. It is the same with $I_{12}^{sat}(\omega_{32})$.

The sample was grown with MBE by our collaborators in TUM. The growth sheet is shown below.

Matrix Layers				
Layer	**Material**	**[nm]**	**Ratio**	**Doping (cm-3)**
1	InGaAs	300	In53Ga47As	
2	InP	100		
3	InGaAs	5	In53Ga47As	
4	AlInAs	1	Al48In52As	
5	AlInAs	2	Al48In52As	3.00E+18
	Start of 26 repeat periods			
6S1	AlInAs	2	Al48In52As	3.00E+18
7S1	AlInAs	1	Al48In52As	
8S1	InGaAs	6.9	In53Ga47As	
9S1	AlInAs	0.9	Al48In52As	
10S1	InGaAs	3.6	In53Ga47As	
11S1	AlInAs	1	Al48In52As	
12S1	AlInAs	2	Al48In52As	3.00E+18
	End of repeat periods			
13	AlInAs	2	Al48In52As	3.00E+18
14	AlInAs	1	Al48In52As	
15	InGaAs	2	In53Ga47As	

Table 6.1: $In_{0.53}Ga_{0.47}As/Al_{0.48}In_{0.52}As$ MQW growth parameters. The semiconductor layers were grown on semi-insulating InP substrate.

The sample absorption spectrum was measured with the multipass geometry method as shown in Fig. 6.3 (a). The sample was cut into 4 mm wide and ~8 mm long. Its substrate was polished to be a shiny surface. 200 nm gold was deposited on both sides of the sample. Then the sample was polished to have facets at 45° to the surface normal. The broadband Mid-IR source from the Fourier-transform infrared spectrometer was chopped at 500 Hz. Then the beam passed through a wire grid polarizer and was focused by a ZnSe lens on the sample surface. The polarizer controlled the beam to TE or TM mode. TE (polarized horizontally) is the background signal and TM (polarized vertically) is the signal can be absorbed by the material. The sample was placed at 45° with facets normal

to the input beam. The output beam was collected and sent to the detector by a pair of ZnSe lens. The measurement result is shown in Fig. 6.3 (b).

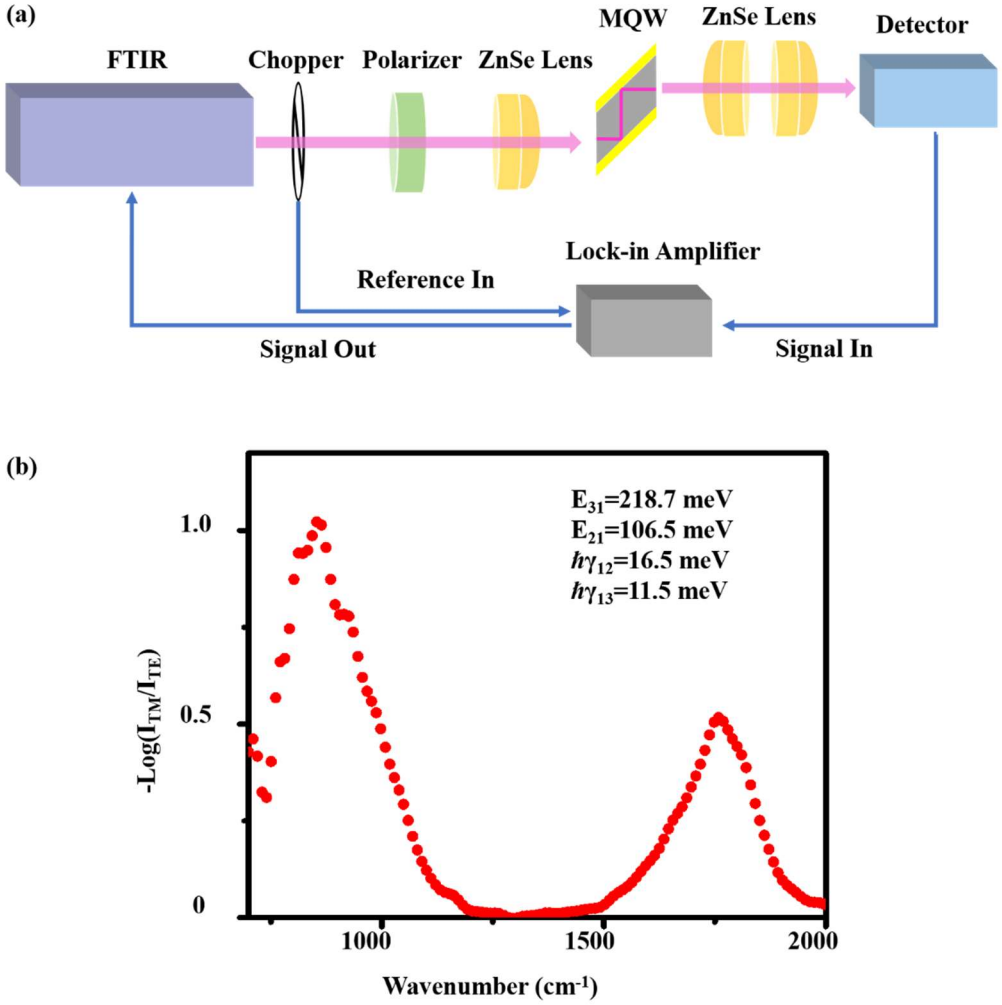

Figure 6.3: (a) Schematic of the intersubband absorption measurement setup. The Mid-IR beam from FTIR was chopped at 500 Hz. Then the beam passed through a wire grid polarizer and was focused by a ZnSe lens on the sample surface. The sample was placed at 45° with facets normal to the input beam. The output beam was collected and sent to the detector by a pair of ZnSe lens. (b) Absorption spectra of the MQW heterostructure acquired by multipass geometry method.

The transition linewidths ($2\hbar\gamma_{ij}$) can be extracted from the full width at half maximum (FWHM) of the absorption peaks. The absorption coefficient can be calculated with[*17*]:

$$\alpha = -\frac{1}{L_{int}}\mathrm{Ln}(10)\, Log_{10}\left(\frac{I_{TM}}{I_{TE}}\right) \tag{6.8}$$

where I_{TM} and I_{TE} are the transmitted intensities of TM-polarized and TE polarized light. L_{int} is the interaction length, which is given by:

$$L_{int} = \frac{L_w N n_p}{cos\theta} \tag{6.9}$$

where L_w is the thickness of one period MQW, *N* is the number of periods in MQW, n_p is the number of passes, θ is the angle of incidence with respect to the MQW growth direction. Here, θ = 45°, L_w = 17.4 nm, *N* = 26, n_p = 20. (The sample length after fabrication length was 7 mm and the sample thickness was 0.33 mm.) The absorption coefficients are α_{12}=3.5×10^3 cm^{-1}, α_{12}=1.8×10^3 cm^{-1}.

I notice that the transition energies are shifted away from designed values and provides a smaller value of $|E_{21} - E_{32}|$. The calculated $I_{12}^{sat}(\omega_{32})$ is 3.31× 10^{10} W/m^2, which leads to a decrease of maximum conversion efficiency (before saturation) from 2.08% to 0.46%. Further research can be focused on the optimization of design and growth condition to reduce the shift or other designs with a large value of $|E_{21} - E_{32}|$.

6.4 SUMMARY

Here, the metasurface behaviors under sufficiently large pump intensity are discussed. The preliminary theoretical analysis predicts a great potential for achieving high-conversion-efficiency metasurfaces with large pump intensity. In future research, except for the analysis above, the damage threshold is another factor that can limit the device performance. The damage threshold is related to the designs of nanoresonators based on our experience.

Chapter 7: Prospect of Difference Frequency Generation in Polaritonic Intersubband Nonlinear Metasurfaces

7.1 Introduction

The THz sources have been widely used in astrophysics, security screening, communication technology, and ultrafast spectroscopy [*56, 57*]. Our group has demonstrated room temperature THz QCL based on intersubband nonlinearities [*58, 59*]. Another method that can potentially provide a room-temperature continuous-wave THz source is using ultra-thin metasurfaces. Metasurfaces optimized for THz DFG using λ=5-15 μm pumps can be used to build high-power THz sources using mid-infrared QCL or CO_2 lasers as pumps. Here, I will explore the possibility of extending the application of nonlinear polaritonic metasurfaces to THz range through the DFG process. I have designed a metasurface for DFG process with the two pumps at $\lambda_1 \approx 8.0$ μm and $\lambda_2 \approx 9.3$ μm, and the difference-frequency at $\lambda_{DFG} \approx 56.4$ μm.

7.2 Metasurface Design and Simulations

The $In_{0.53}Ga_{0.47}As/Al_{0.48}In_{0.52}As$ quantum well structure for Mid-IR to THz DFG was designed using a self-consistent Poisson–Schrödinger solver. The structure was designed to be resonant for the DFG process with the two pumps at $\lambda_1 \approx 8.0$ μm (155 meV) and $\lambda_2 \approx 9.3$ μm (133 meV) and the difference-frequency at $\lambda_{DFG} \approx 56.4$ μm (23 meV). The layer sequence (in nanometer) is **4**/3.3/**2.7**/9.2/**4** where AlInAs barriers are marked in bold, and the 9.2 nm well are n-doped to 0.5×10^{17} cm^{-3}. The conduction band diagram of one MQW period is shown in Fig. 7.1.

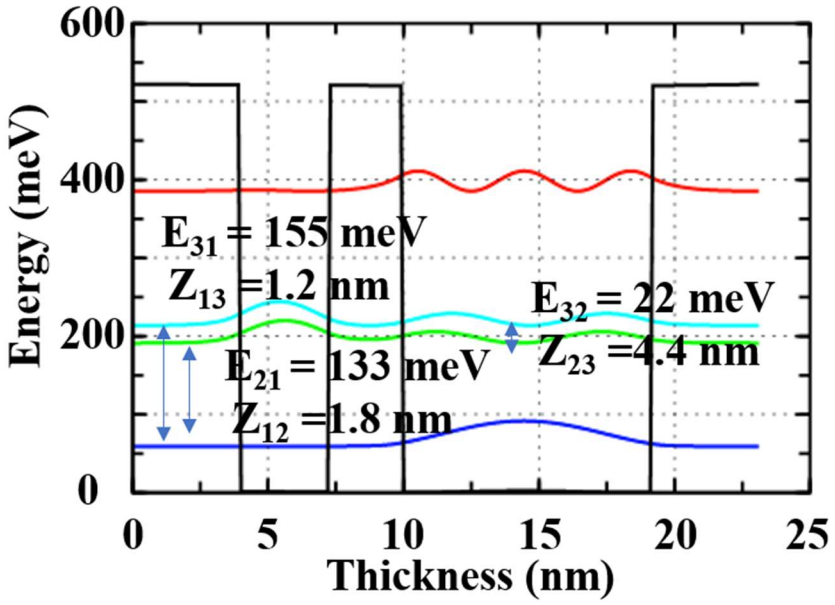

Figure 7.1：Conduction band diagram of one period of an $In_{0.53}Ga_{0.47}As/Al_{0.48}In_{0.52}As$ MQW structure designed for Mid-infrared-to-THz DFG. The layer sequence (in nanometer) is **4**/3.3/**2.7**/9.2/**4** where AlInAs barriers are marked in bold, and the 9.2 nm well are n-doped to 5×10^{17} cm^{-3}.

For this structure, $\hbar\omega_{31}$ = 155 meV, $\hbar\omega_{21}$ = 133 meV. z_{13} = 1.2 nm, z_{12} = 1.8 nm, z_{13} = 4.4 nm. The dipole matrix element z_{11}, z_{22}, z_{33} were calculated with a matlab file using equations:

$$z_{ij} = \frac{\int \varphi_i \, z \, \varphi_j^* \, dz}{\sqrt{\int \varphi_i \;\; \varphi_i^* \, dx \cdot \int \varphi_j \;\; \varphi_j^* \, dx}} \tag{7.1}$$

where φ_i and φ_j are the wave function of state i and j. z_{11} = 14.4 nm, z_{22} = 9.9 nm, z_{33} = 10.0 nm.

An 800-nm-thick MQW layer composed of 34 repetitions of the structure in Fig. 7.1 was grown by the molecular beam epitaxy on a semi-insulating InP substrate by our collaborators in TUM. The growth sheet is shown in Table 7.1.

Matrix Layers				
Layer	**Material**	**[nm]**	**Ratio**	**Doping (cm-3)**
1	InGaAs	300	In53Ga47As	
2	InP	100		
3	InGaAs	5	In53Ga47As	
4	AlInAs	4	Al48In52As	
	Start of 34 repeat periods			
5S1	AlInAs	4	Al48In52As	
6S1	InGaAs	3.3	In53Ga47As	
7S1	AlInAs	2.7	Al48In52As	
8S1	InGaAs	9.2	In53Ga47As	5.00E+17
9S1	AlInAs	4	Al48In52As	
	End of repeat periods			
10	AlInAs	4	Al48In52As	
11	InGaAs	5	In53Ga47As	

Table 7.1: $In_{0.53}Ga_{0.47}As/Al_{0.48}In_{0.52}As$ MQW growth parameters. The semiconductor layers were grown on semi-insulating InP substrate.

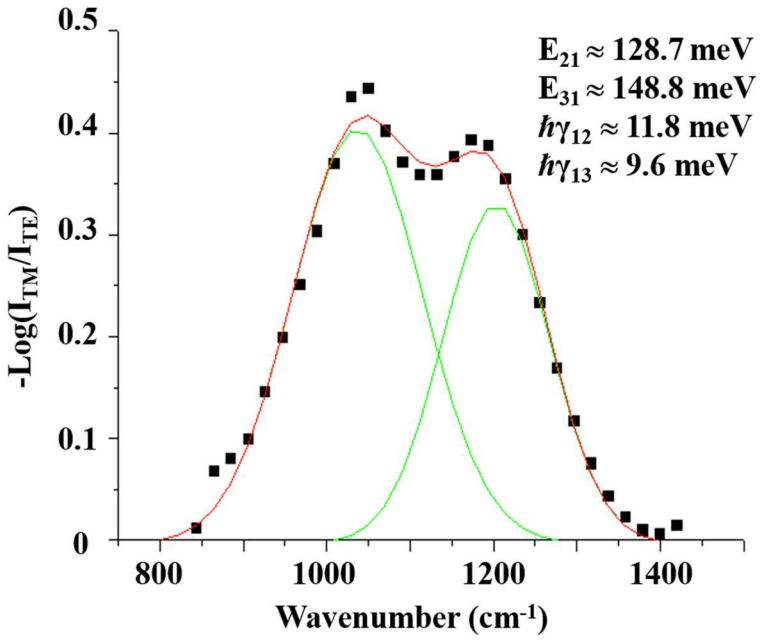

Figure 7.2：Absorption spectrum of the Mid-infrared-to-THz MQW heterostructure acquired by multipass geometry method.

The absorption spectrum of the grown material is measured with a multipass geometry. The experimental absorption results are shown in Figure 7.2. The absorption spectrum of the grown structure indicates that the intersubband transition energies between the ground state and states 3 and 2 are 148.8 meV and 128.7 meV, slightly different from the design targets. $\hbar\gamma_{12}$=11.8 meV, and $\hbar\gamma_{13}$=9.6 meV. I further assumed $\hbar\gamma_{32}$ =5.0 meV and $\hbar\gamma$ =5.0 meV for calculation of $\chi^{(2)}_{MQW,zzz}$. The expression of $\chi^{(2)}_{MQW,zzz}$ for Mid-infrared-to-THz DFG is [*11*]:

$$\chi^{(2)}_{MQW,zzz}(\omega_1-\omega_2,\omega_1,\omega_2)=\frac{e^3}{2\varepsilon_0\hbar}\left\{\frac{(N_1-N_2)z_{12}z_{23}z_{31}}{(\omega_{32}-\omega_1+\omega_2-i\gamma_{32})(\omega_{21}-\omega_2+i\gamma_{21})}\right. \quad (7.2)$$
$$-\frac{(N_1-N_3)z_{12}z_{23}z_{31}}{(\omega_{32}-\omega_1+\omega_2-i\gamma_{23})(\omega_{31}-\omega_1-i\gamma_{31})}$$
$$+\frac{(N_1-N_3){z_{13}}^2(z_{11}-z_{33})(\omega_1-\omega_2+2i\gamma_{31})}{(\omega_1-\omega_2+i\gamma)(\omega_1-\omega_{31}+i\gamma_{31})(\omega_{31}-\omega_2+i\gamma_{31})}$$
$$\left.+\frac{(N_1-N_2){z_{12}}^2(z_{11}-z_{22})(\omega_1-\omega_2+2i\gamma_{21})}{(\omega_1-\omega_2+i\gamma)(\omega_1-\omega_{21}+i\gamma_{21})(\omega_{21}-\omega_2+i\gamma_{21})}\right\}$$

Since one of the pump lasers is tunable and the other is fixed at 133 meV, the output THz signal is also tunable. The calculated $\chi^{(2)}_{MQW,zzz}$ is shown in Table 7.2. (Please note the definition of $\chi^{(2)}_{MQW,zzz}$ here is different from the one in Ref. [*15*].)

Frequency (THz)	4	4.5	5	5.5	5.6	5.7	5.8
$\chi^{(2)}_{MQW,zzz}$ (nm/V)	516.5	508	436.5	325	297.5	276	256

Table 7.2: Calculated $\chi^{(2)}_{MQW,zzz}$ for different DFG output frequencies.

A long-tail T structure has been optimized for the electromagnetic resonances at two mid-IR pump frequencies and THz DFG frequency, similar as in Ref. [*15*].

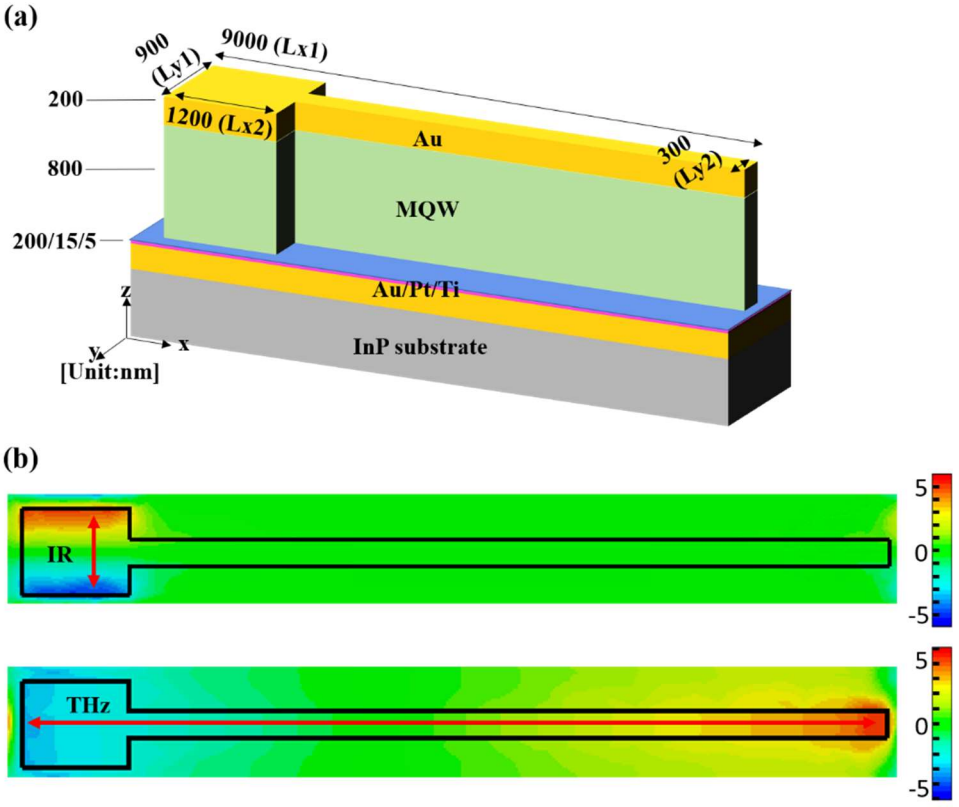

Figure 7.3: (a) A metasurface unit-cell (9.2 μm × 1.1 μm) of the Mid-infrared-to-THz DFG metasurface. (b) The simulated E_z field enhancement at the IR pump frequencies and the output THz monitored in the MQW layer 400 nm below the top metal surface of the nanoresonator. The color code shows the field enhancements in the MQW heterostructure relative to the electric-field amplitudes in the incoming waves.

However, it is still uncertain about which model (isotropic/anisotropic) is proper to describe the behavior of electrons in this material. Here, we use an anisotropic model to describe the behavior of electrons in the IR range. The material parallel permittivities can be calculated with equations (2.2) and the vertical permittivities can be calculated with:

$$\varepsilon_{\perp}(\omega) \approx \varepsilon_{core}(\omega) + \frac{Ne^2 z_{21}^2}{\epsilon_0 \hbar(\omega_{21} - \omega - i\gamma_{21})} + \frac{Ne^2 z_{31}^2}{\epsilon_0 \hbar(\omega_{31} - \omega - i\gamma_{31})} \tag{7.3}$$

An isotropic model is used to describe the behavior of electrons in the THz range, which means the material permittivities are calculated with equations (2.2) for all directions. The optimized structure with this model is shown in Fig. 7.3. The overlap of this structure is around 1.97 for 5.5 THz output.

Generally, the purpose of our nonlinear metasurface optimization is to achieve either maximum output intensity or maximum conversion efficiency. For maximum DFG intensity, from equation (4.18), we can get the optimization factor including MQW thickness is :

$$M = d\frac{\int_V \frac{E_z^{\omega_1}}{E_{inc}^{\omega_1}} \frac{E_z^{\omega_2}}{E_{inc}^{\omega_2}} \frac{E_z^{\omega_{DFG}}}{E_{inc}^{\omega_{DFG}}} dV}{V} \tag{7.4}$$

For maximum DFG conversion efficiency, if the conversion efficiency is defined as:

$$\eta = \frac{I_{air}^{DFG}}{\frac{1}{2}(I_{air}^{\omega_1} + I_{air}^{\omega_2})} \tag{7.5}$$

then we have:

$$\eta = \frac{(\omega_{DFG}\chi_{MQW,zzz}^{(2)} d)^2 \frac{I_{MQW}^{\omega_1}}{\ell_1}\frac{I_{MQW}^{\omega_2}}{\ell_2}}{\varepsilon_0 c^3 (\frac{I_{MQW}^{\omega_1}}{\ell_1} + \frac{I_{MQW}^{\omega_2}}{\ell_2})} \left| \frac{\int_V \frac{E_z^{\omega_1}}{E_{inc}^{\omega_1}} \frac{E_z^{\omega_2}}{E_{inc}^{\omega_2}} \frac{E_z^{\omega_{DFG}}}{E_{inc}^{\omega_{DFG}}} dV}{V} \right|^2 \tag{7.6}$$

where $\ell_1 = \frac{\int_V \left|\frac{E_z^{\omega_1}}{E_{inc}^{\omega_1}}\right|^2 dV}{V}$, $\ell_2 = \frac{\int_V \left|\frac{E_z^{\omega_2}}{E_{inc}^{\omega_2}}\right|^2 dV}{V}$. The optimization factor for maximum DFG conversion efficiency is:

$$F = d^2 \frac{1}{(\beta\ell_2 + \ell_1)} \left| \frac{\int_V \frac{E_z^{\omega_1}}{E_{inc}^{\omega_1}} \frac{E_z^{\omega_2}}{E_{inc}^{\omega_2}} \frac{E_z^{\omega_{DFG}}}{E_{inc}^{\omega_{DFG}}} dV}{V} \right|^2 \tag{7.7}$$

where $\beta = \frac{I_{MQW}^{\omega_1}}{I_{MQW}^{\omega_2}}$. Here, I have designed the structures with the purpose of maximum conversion efficiency. I have simulated the same MQW with different thicknesses (400 nm, 600 nm, 800nm). The simulation results reveal that 800 nm is preferred for Mid-IR to THz DFG metasurface with F factor ~4.4 times larger than 400 nm MQW, ~1.6 times larger than 600 nm MQW. (For different MQW layer sequence, doping levels and nanoresonator dimensions, F factor follows a similar trend as thickness increases.) Thus the best designed MQW here was grown with a thickness of 800 nm.

7.3 EXPERIMENTAL CHARACTERIZATION

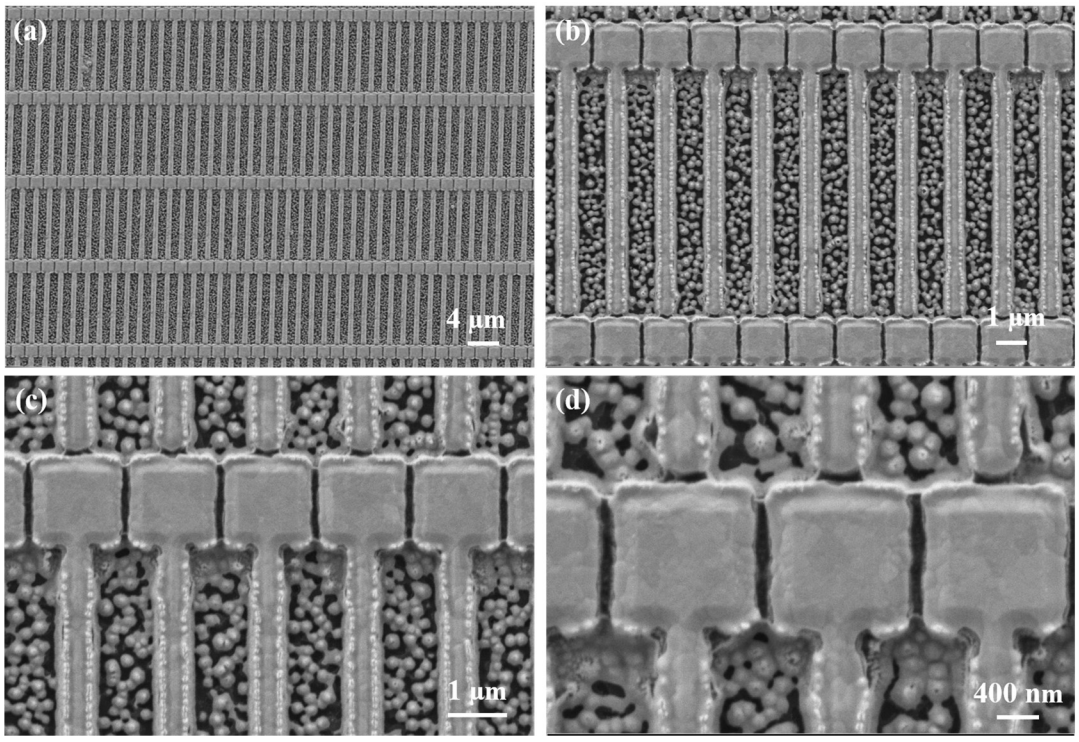

Figure 7.4: The SEM images of the fabricated Mid-IR to THz metasurface.

The sample was fabricated in a similar method as described in Chapter 4. Because of the difference between experiments and simulations, 25 different patterns with varies dimensions are fabricated. The SEM images of the fabricated metasurface structure have

been shown in Figure 7.4. As you may notice, the etched area on the sample surface has many residues and may need further improvements.

The setup for IR reflection-absorption measurement is shown in Fig. 7.5 (a). The IR light from FTIR was chopped at 500 Hz. The chopped light passed through a wire grid polarizer and a 50/50 beam splitter, then focused on the metasurface by an objective lens (numerical aperture 0.5). The sample surface was normal to the input beam propagating direction. The reflected light was collected by the same lens, reflected by the beam splitter, focused by a ZnSe lens and then sent to the HgCdTe detector.

Because of the lack of beamsplitters and polarizers that can work for 4-6 THz range, the reflection-absorption spectrum of the fabricated metasurface was measured at 45° incidence without a polarizer. The setup is shown in Fig. 7.5 (b). The THz light from FTIR was chopped at 500 Hz, then focused on the metasurface by an off-axis parabolic mirror (1-inch diameter, 1-inch focal length). The sample was placed at 45° with respect to the input beam. The reflected light was collected by another off-axis parabolic mirror (1-inch diameter, 1-inch focal length), and then sent to the detector by a large off-axis parabolic mirror (2-inch diameter, 4-inch focal length). A helium-cooled bolometer was used for THz reflection-absorption measurement. Due to the absorption of THz signal in the air, the whole setup was covered and purged with N_2 during the THz reflection-absorption measurement.

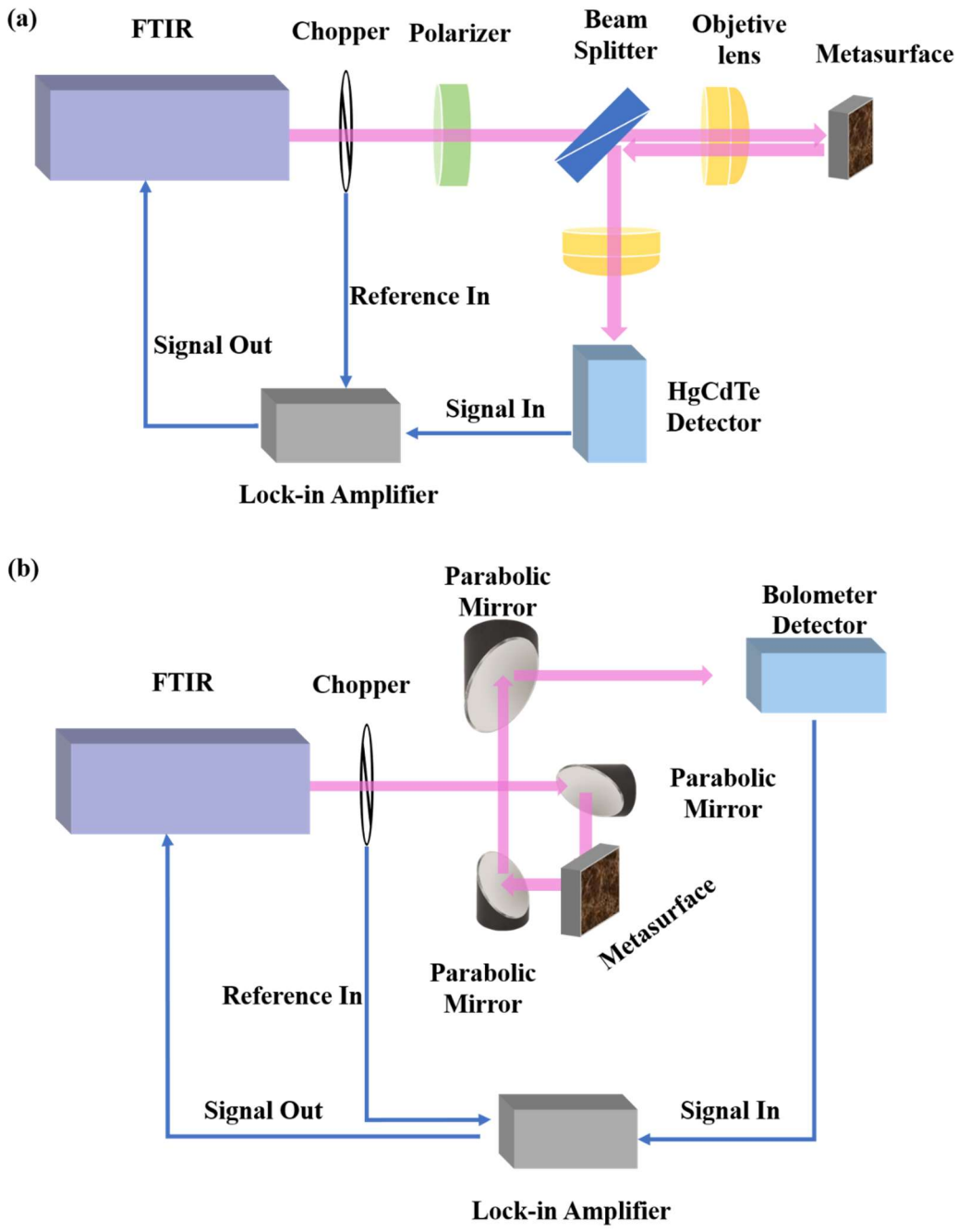

Figure 7.5: (a) Schematic of setup for the IR reflection-absorption measurement at normal incidence. (b) Schematic of the setup for the THz reflection-absorption measurement at 45° incidence.

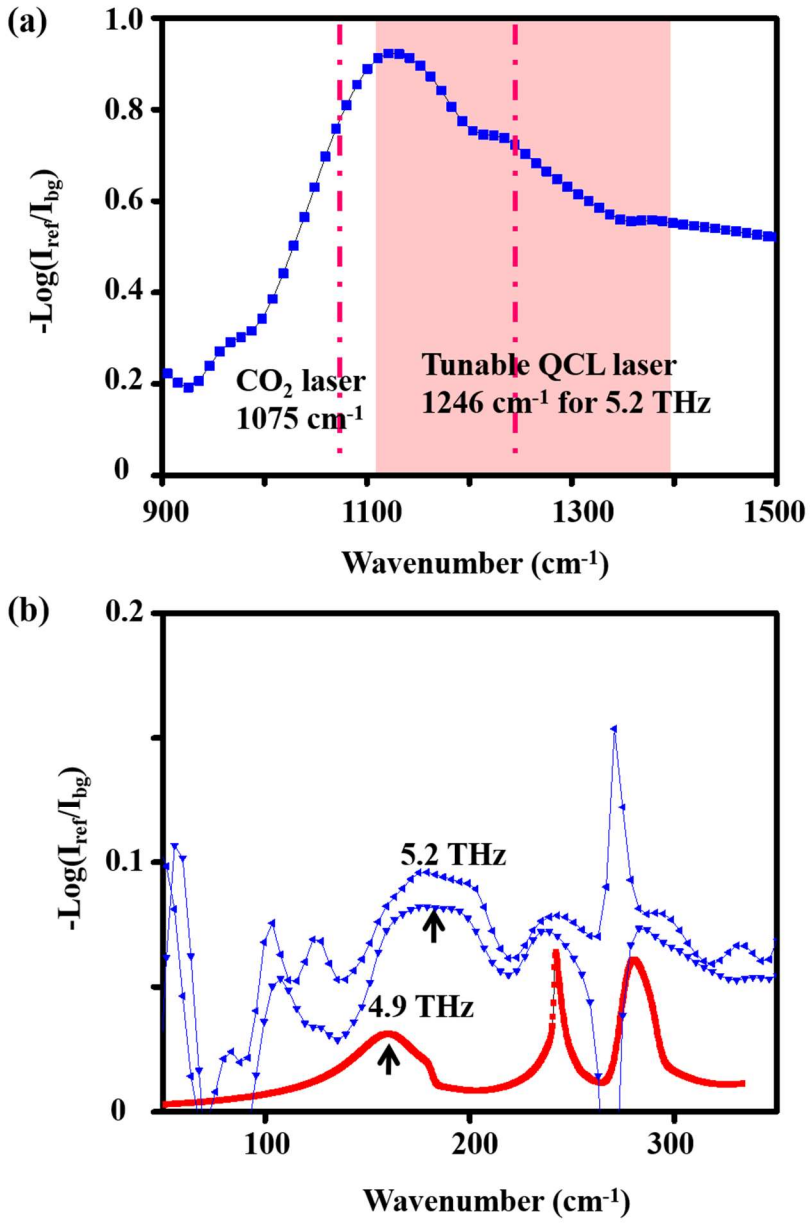

Figure 7.6: (a) IR reflection-absorption spectrum at normal incidence. The metasurface has strong absorptions near the two pump wavenumbers. The CO_2 laser wavenumber is 1705 cm^{-1}. The red area represents the tuning range of the QCL laser. For DFG output at 5.2 THz, the QCL wavenumber is 1246 cm^{-1} (b) THz reflection-absorption spectrum at 45° incidence. The blue curves are the experimental results of the same patterns. The red curve is the simulation results at 45° incidence.

The best reflection-absorption spectrum is from a pattern with dimensions of ly1=1400 nm, ly2=300 nm, lx2=1400 nm, lx1=8000 nm. The reflection-absorption spectrum of this pattern was shown in Fig. 7.6. I_{ref} is the reflected beam intensity on pattern area, I_{bg} is the reflected beam intensity on gold with no patterns. In Fig. 7.6 (a), the metasurface has strong absorptions near the two pump wavenumbers. The CO_2 laser wavenumber is 1705 cm^{-1}. The red area represents the tuning range of the QCL laser. For DFG output at 5.2 THz, the QCL wavenumber is 1246 cm^{-1}. In Fig. 7.6 (b), the reflection-absorption spectrum is measured with 45° incidence. The blue curves are the experimental results (measured twice) and the red curve is the simulation results. The simulation results are acquired by $-log(0.5 + 0.5 \cdot S_{11}^2)$ for the case with no polarizer. This reflection-absorption spectrum indicates a weak absorption in the THz range. The strongest absorption is around 5.2 THz, which is close to the simulation absorption peak - 4.9 THz. In addition, the absorption from measurement is stronger than the absorption from simulation, which may be related to the isotropic model used for permittivity calculation.

The optical set-up for mid-infrared-to-THz DFG metasurface nonlinear characterization is shown in Fig. 7.7 with normal incidence. A linear polarized tunable QCL and a non-tunable CO_2 laser were placed with the same polarization. A long-pass filter was used as a beam splitter to combine the two beams. The beams passed through a parabolic mirror by the hole (D=3.2 mm), and then were focused on the sample by a small parabolic mirror. The output DFG signal was collected by the small parabolic mirror, and then was reflected and focused by the parabolic mirror with a hole to the bolometer detector. Because the THz beam has a larger beam size than the hole, we expected the parabolic mirror with a hole can still collect most part of the THz signal.

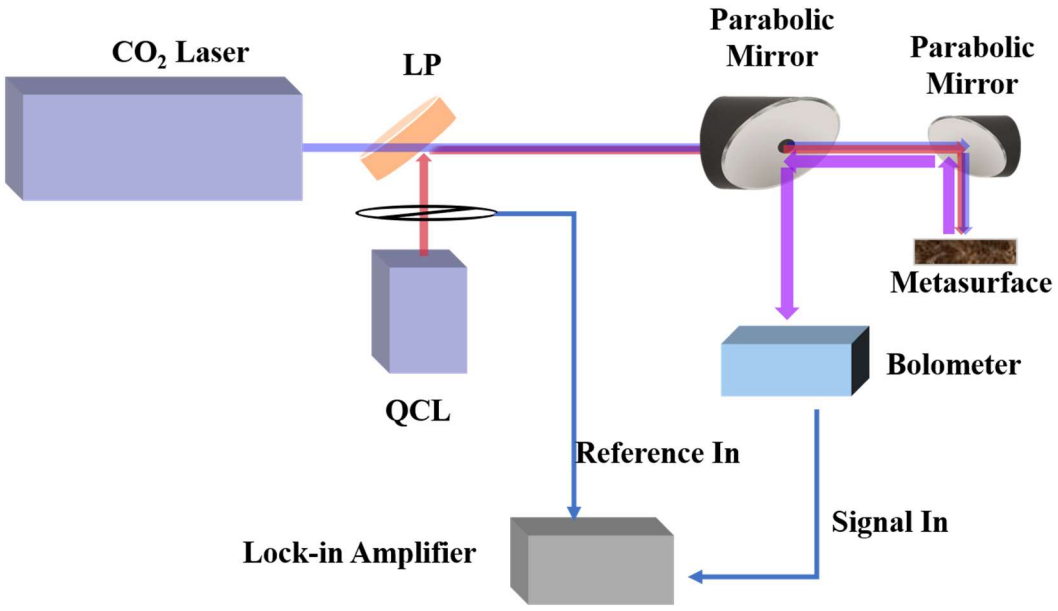

Figure 7.7: Optical set-up for metasurface nonlinear characterization. A linear polarized tunable QCL and a non-tunable CO_2 laser were placed with the same polarization. A long-pass filter was used as a beam splitter to combine the two beams. The beams passed through a parabolic mirror by the hole, and then were focused on the sample by a small parabolic mirror. The output DFG signal was collected by the small parabolic mirror, and then was reflected and focused by the parabolic mirror with a hole to the bolometer detector.

In the actual experiment, the power of the CO_2 laser is reduced in order to protect optical components and sample. The CO_2 laser (D=3.5 mm) was working under continuous mode with the power of 3.3 W at the sample position. (A long focal length ZnSe lens was used to shrink the beam to pass through the hole.) The QCL (D<2.5 mm) (Daylight) was working at 10% duty cycle (250 kHz) with the peak power of 270 mW at the sample position. The radius of the focused QCL beam was around 90 μm, and the radius of the focused CO_2 beam was around 127 μm. The calculated peak intensity of CO2 laser is 13.0 kW/cm^2 and the calculated peak intensity of QCL is 2.1 kW/cm^2. Effective susceptibility is 640 nm/V. Sample thickness is 800 nm. In this system, the

calculated DFG beam size is 73 μm and the output peak power at the sample position is ~13.7 μW. The average power is 0.69 μW. The following measurement will be performed by other group members.

Another option is designing devices in transmission mode rather than the reflection mode, which can avoid the wide frequency range requirements of optical components. Based on our previous research experience, a metasurface without metal backplane will cause a reduction of nonlinearity around 4 times[*60*]. A preferred design is a metasurface in transmission mode with both metallic resonators on top and bottom (as shown below). This requires further fabrication development of plasma etching of bottom layer Au after high-temperature wafer bonding, or the wafer bonding with photoresist (SU8) between metal and InP substrate at a lower temperature.

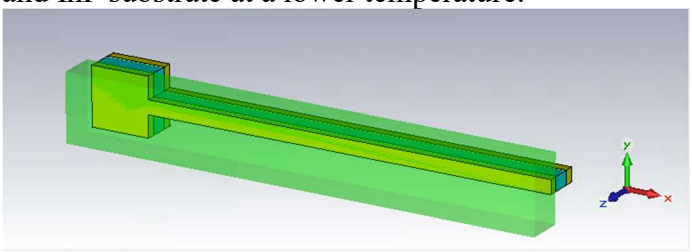

Figure 7.8: A Mid-infrared-to-THz DFG metasurface unit-cell in transmission mode.

7.4 SUMMARY

I have designed a metasurface for DFG process with the two pumps at $\lambda_1 \approx 8.0$ μm and $\lambda_2 \approx 9.3$ μm, and the difference-frequency at $\lambda_{DFG} \approx 56.4$ μm. The preliminary experimental results indicate the long-tail nanoresonators can provide resonances for both IR and THz signals. Although there are still uncertainties about the permittivity models and other experimental issues, this work lights up the path for future study of mid-infrared-to-THz metasurfaces.

Chapter 8: Conclusion

8.1 SUMMARY

In this dissertation, I have extended the functionality of polaritonic nonlinear metasurfaces to difference-frequency and sum-frequency generation in the mid-infrared range with two distinct input pumps. I have provided the theoretical analysis for both DFG and SFG metasurfaces and also performed the experiments with theoretical guidance. In Chapter 4, I have demonstrated the DFG in polaritonic nonlinear metasurface for the first time. The conversion efficiency with respect to pump 1 intensity ($\frac{I_{0DFG}}{I_{01}}$) is approximately 0.13%, which corresponds to 0.3% conversion of pump 1 photons to DFG photons. This research also indicates that the DFG metasurface can survive under the beam intensity of ~ 50 kW/cm^2. In Chapter 5, the first SFG polaritonic nonlinear metasurface has been demonstrated with a conversion efficiency of 0.03% with input intensity of 30.4 kW/cm^2 and 3.3 kW/cm^2. The behavior of upconversion metasurface under high-intensity beams is discussed in Chapter 6. Except for the study of DFG and SFG metasurfaces in the mid-infrared range, I have also explored the possibility of mid-infrared-to-THz DFG metasurfaces in Chapter 7. The preliminary experimental results indicate the long-tail nanoresonators could provide resonance for THz signal. In addition, in Chapter 2, the design of SHG MQW with new materials with a predicted conversion efficiency of 1.2% has also be discussed as complementary to our previous SHG research.

For future study about the second-order polaritonic metasurfaces, except exploring new MQW materials and optimizing the design of metasurfaces, one interesting topic is to study the behaviors of metasurface under high-intensity beams (>50 kW/cm^2). This can potentially lead to a remarkable improvement in conversion efficiency

based on the theoretical analysis. For the mid-infrared-to-THz DFG metasurface which can possibly provide continuous room-temperature THz source, except further optimization of the optical setup, the devices in transmission mode rather than the reflection mode can be explored to avoid the wide frequency range requirements of optical components.

References

1. N. Yu, F. Capasso, Flat optics with designer metasurfaces. *Nature materials* **13**, 139 (2014).

2. L. Novotny, N. Van Hulst, Antennas for light. *Nature photonics* **5**, 83 (2011).

3. J. A. Schuller *et al.*, Plasmonics for extreme light concentration and manipulation. *Nature materials* **9**, 193 (2010).

4. Y. Svirko, N. Zheludev, M. Osipov, Layered chiral metallic microstructures with inductive coupling. *Applied physics letters* **78**, 498-500 (2001).

5. S. A. Maier, Plasmonic field enhancement and SERS in the effective mode volume picture. *Optics Express* **14**, 1957-1964 (2006).

6. F. Ding, A. Pors, S. I. Bozhevolnyi, Gradient metasurfaces: a review of fundamentals and applications. *Reports on Progress in Physics* **81**, 026401 (2017).

7. A. Krasnok, M. Tymchenko, A. Alu, Nonlinear metasurfaces: a paradigm shift in nonlinear optics. *Materials Today* **21**, 8-21 (2018).

8. N. Nookala *et al.*, Ultrathin gradient nonlinear metasurface with a giant nonlinear response. *Optica* **3**, 283-288 (2016).

9. J. Lee *et al.*, Ultrathin second‐harmonic metasurfaces with record‐high nonlinear optical response. *Advanced Optical Materials* **4**, 664-670 (2016).

10. J. Lee *et al.*, Giant nonlinear response from plasmonic metasurfaces coupled to intersubband transitions. *Nature* **511**, 65 (2014).

11. R. W. Boyd, *Nonlinear Optics*. (Academic Press, ed. 3rd, 2008).

12. Y. R. Shen, *The principles of nonlinear optics*. (Wiley-Interscience, 2003).

13. G. Li *et al.*, Continuous control of the nonlinearity phase for harmonic generations. *Nature materials* **14**, 607 (2015).

14. N. Segal, S. Keren-Zur, N. Hendler, T. Ellenbogen, Controlling light with metamaterial-based nonlinear photonic crystals. *Nature Photonics* **9**, 180 (2015).

15. M. Tymchenko, J. Gomez-Diaz, J. Lee, M. Belkin, A. Alù, Highly-efficient THz generation using nonlinear plasmonic metasurfaces. *Journal of Optics* **19**, 104001 (2017).

16. E. R. Weber, R. K. Willardson, H. Liu, F. Capasso, *Intersubband transitions in quantum wells: physics and device applications*. (Academic press, 1999), vol. 62.

17. F. Capasso, C. Sirtori, A. Y. Cho, Coupled quantum well semiconductors with giant electric field tunable nonlinear optical properties in the infrared. *IEEE Journal of Quantum Electronics* **30**, 1313-1326 (1994).

18. J. Gomez-Diaz, M. Tymchenko, J. Lee, M. A. Belkin, A. Alù, Nonlinear processes in multi-quantum-well plasmonic metasurfaces: electromagnetic response, saturation effects, limits, and potentials. *Physical Review B* **92**, 125429 (2015).

19. I. Vurgaftman, J. R. Meyer, L. R. Ram-Mohan, Optimized second-harmonic generation in asymmetric double quantum wells. *IEEE journal of quantum electronics* **32**, 1334-1346 (1996).

20. F. Ding, Y. Yang, R. A. Deshpande, S. I. Bozhevolnyi, A review of gap-surface plasmon metasurfaces: fundamentals and applications. *Nanophotonics* **7**, 1129-1156 (2018).

21. D. Palaferri *et al.*, Room-temperature nine-μm-wavelength photodetectors and GHz-frequency heterodyne receivers. *Nature* **556**, 85 (2018).

22. D. Palaferri *et al.*, Patch antenna terahertz photodetectors. *Applied Physics Letters* **106**, 161102 (2015).

23. J. Madéo *et al.*, Patch antenna microcavity terahertz sources with enhanced emission. *Applied Physics Letters* **109**, 141103 (2016).

24. S. A. Bashar, Study of indium tin oxide (ITO) for novel optoelectronic devices. *UMIST, Manchester*, 106-109 (1998).

25. L. Zang, *Energy efficiency and renewable energy through nanotechnology*. (Springer, 2011).

26. A. R. Adams, Strained-layer quantum-well lasers. *IEEE Journal of Selected Topics in Quantum Electronics* **17**, 1364-1373 (2011).

27. D. Arent, K. Deneffe, C. Van Hoof, J. De Boeck, G. Borghs, Strain effects and band offsets in GaAs/InGaAs strained layered quantum structures. *Journal of applied physics* **66**, 1739-1747 (1989).

28. T. B. Bahder, Eight-band k· p model of strained zinc-blende crystals. *Physical Review B* **41**, 11992 (1990).

29. S. Campione, A. Benz, M. B. Sinclair, F. Capolino, I. Brener, Second harmonic generation from metamaterials strongly coupled to intersubband transitions in quantum wells. *Applied Physics Letters* **104**, 131104 (2014).

30. W. Fan *et al.*, Second harmonic generation from patterned GaAs inside a subwavelength metallic hole array. *Optics express* **14**, 9570-9575 (2006).

31. S. Kruk *et al.*, Enhanced magnetic second-harmonic generation from resonant metasurfaces. *ACS Photonics* **2**, 1007-1012 (2015).

32. F. Niesler *et al.*, Second-harmonic generation from split-ring resonators on a GaAs substrate. *Optics letters* **34**, 1997-1999 (2009).

33. D. A. Smirnova, A. E. Miroshnichenko, Y. S. Kivshar, A. B. Khanikaev, Tunable nonlinear graphene metasurfaces. *Physical Review B* **92**, 161406 (2015).

34. G. Li, S. Zhang, T. Zentgraf, Nonlinear photonic metasurfaces. *Nature Reviews Materials* **2**, 17010 (2017).

35. O. Wolf *et al.*, Phased-array sources based on nonlinear metamaterial nanocavities. *Nature communications* **6**, 7667 (2015).

36. F. Capasso, C. Liu, E. Weber, R. Willardson, Intersubband transitions in quantum wells: Physics and device applications. *Semiconductors and Semimetals, edited by HC Liu Academic, San Diego, CA* **62**, 18 (2000).

37. J. Lee, (2014).

38. L. Fu, Z. Wang, E. C. Yan, Chiral vibrational structures of proteins at interfaces probed by sum frequency generation spectroscopy. *International journal of molecular sciences* **12**, 9404-9425 (2011).

39. K. Kuhnke, D. Hoffmann, X. Wu, A. Bittner, K. Kern, Chemical imaging of interfaces by sum-frequency generation microscopy: Application to patterned self-assembled monolayers. *Applied physics letters* **83**, 3830-3832 (2003).

40. S. Yamaguchi, Development of single-channel heterodyne-detected sum frequency generation spectroscopy and its application to the water/vapor interface. *The Journal of chemical physics* **143**, 034202 (2015).

41. Y. Shen, Surface properties probed by second-harmonic and sum-frequency generation. *Nature* **337**, 519 (1989).

42. J. Shah, Ultrafast luminescence spectroscopy using sum frequency generation. *IEEE Journal of Quantum Electronics* **24**, 276-288 (1988).

43. R. H. Hadfield, Single-photon detectors for optical quantum information applications. *Nature photonics* **3**, 696 (2009).

44. A. Eckstein, B. Brecht, C. Silberhorn, A quantum pulse gate based on spectrally engineered sum frequency generation. *Optics express* **19**, 13770-13778 (2011).

45. S. Tanzilli *et al.*, A photonic quantum information interface. *Nature* **437**, 116 (2005).

46. D. V. Strekalov, A. S. Kowligy, Y.-P. Huang, P. Kumar, Optical sum-frequency generation in a whispering-gallery-mode resonator. *New Journal of Physics* **16**, 053025 (2014).

47. J. C. Baumert, F. Schellenberg, W. Lenth, W. Risk, G. Bjorklund, Generation of blue cw coherent radiation by sum frequency mixing in KTiOPO4. *Applied physics letters* **51**, 2192-2194 (1987).

48. Z.-Y. Zhou *et al.*, Generation of light with controllable spatial patterns via the sum frequency in quasi-phase matching crystals. *Scientific reports* **4**, 5650 (2014).

49. W. Risk, W. Lenth, Diode laser pumped blue‐light source based on intracavity sum frequency generation. *Applied physics letters* **54**, 789-791 (1989).

50. E. Mimoun, L. De Sarlo, J.-J. Zondy, J. Dalibard, F. Gerbier, Sum-frequency generation of 589 nm light with near-unit efficiency. *Optics express* **16**, 18684-18691 (2008).

51. R. Demur *et al.*, Near-infrared to visible upconversion imaging using a broadband pump laser. *Optics express* **26**, 13252-13263 (2018).

52. H. Maestre, A. Torregrosa, C. Fernández-Pousa, J. Capmany, IR-to-visible image upconverter under nonlinear crystal thermal gradient operation. *Optics express* **26**, 1133-1144 (2018).

53. L. Huot, P. M. Moselund, P. Tidemand-Lichtenberg, L. Leick, C. Pedersen, Upconversion imaging using an all-fiber supercontinuum source. *Optics letters* **41**, 2466-2469 (2016).

54. H. Maestre, A. Torregrosa, J. Capmany, IR Image upconversion using band-limited ASE illumination fiber sources. *Optics express* **24**, 8581-8593 (2016).

55. Y. Liu *et al.*, Difference‐Frequency Generation in Polaritonic Intersubband Nonlinear Metasurfaces. *Advanced Optical Materials* **6**, 1800681 (2018).

56. M. Tonouchi, Cutting-edge terahertz technology. *Nature photonics* **1**, 97 (2007).

57. S. Dhillon *et al.*, The 2017 terahertz science and technology roadmap. *Journal of Physics D: Applied Physics* **50**, 043001 (2017).

58. K. Vijayraghavan *et al.*, Broadly tunable terahertz generation in mid-infrared quantum cascade lasers. *Nature communications* **4**, 2021 (2013).

59. S. Jung *et al.*, Broadly tunable monolithic room-temperature terahertz quantum cascade laser sources. *Nature communications* **5**, 4267 (2014).

60. N. Nookala *et al.*, Mid-infrared second-harmonic generation in ultra-thin plasmonic metasurfaces without a full-metal backplane. *Applied Physics B* **124**, 132 (2018).